UNIVERSITY OF CALIFORNIA, MERCED

Transport Phenomena in Fuel Cells

by

Mrittunjoy Sarker

Ph.D. thesis
in
Mechanical Engineering

Committee in charge:

Professor James Palko, Chair
Professor Po-Ya Abel Chuang, Thesis Advisor
Professor Venkattraman Ayyaswamy
Professor Min Hwan Lee

2024

This Ph.D. thesis of Mrittunjoy Sarker is approved, and it is acceptable in quality and form for any future publication on microfilm and electronically:

Professor James Palko, Chair	Date
Professor Po-Ya Abel Chuang, Thesis Advisor	Date
Venkattraman Ayyaswamy	Date
Min Hwan Lee	Date

University of California, Merced
2024

To my family - Shusmita and my parents; my friends - Dr. Nitul, Dr. Ayon, Felipe, Azimur, Rubel, Jobaer, Rojoni; my esteemed colleagues at Honda - Yiman, Shutang; and my respected advisor, Professor Chuang - all of whom believed in me and supported my journey in their unique ways.

ACKNOWLEDGMENT

First and foremost, I extend my deepest gratitude to my advisor, Professor Dr. Po-Ya Abel Chuang, for welcoming me into the Thermal and Electrochemical Energy Laboratory (TEEL) at UC Merced. His invaluable training, insightful suggestions, critical comments, and generous funding support have been pivotal throughout my graduate studies.

I am equally thankful to my peers in TEEL, who have been instrumental in my research endeavors, with special thanks to Felipe Mojica, now at Bosch, USA, for meticulously guiding me through fuel cell testing and diagnostics. My appreciation extends to Dr. Md. Azimur Rahman, a former colleague at TEEL and now at General Motors, for his critical contributions to my Ph.D. thesis and our collaborative manuscripts. I am also grateful to Shirin Mehrazi and Marc Francis Labata for their assistance with SEM imaging. Special gratitude goes to Dr. Nitul, now at OCOchem, for his willingness to review my writings upon request, and to Dr. Ayon Karmakar for his support in my research. Additionally, my journey was supported by Joy Marie Mora, Zabih Najafianashrafi, Pulkit Sagar, and Robel Mehari Tesfaye, whose motivation and well wishes were a constant source of encouragement.

The AEMFC project would not have been feasible without the significant support from Dr. Ami Neyerlin and Dr. Bryan Pivovar of the National Renewable Energy Laboratory (NREL) in Golden, Colorado. Their supply of materials and expert guidance were invaluable to the project's success.

The PEMFC study project on the sensitivity analysis of limiting current was supported by the GREENPower Program (IIID 2015-09) from the Commission on Higher Education- Philippine California Advanced Research Institutes (CHED-PCARI) of the Republic of the Philippines, with additional thanks to TORAY Industries Inc. and Freudenberg Group for supplying Toray 060 and Freudenberg H23C8 gas diffusion media, respectively.

Thanks to Chemours^{TM} for providing us with their pre-commercial, highly oxygen-permeable ionomer (HOPI), which helped us characterize and investigate both the durability and fuel cell performance using this ionomer. Special thanks to Austin Plymill and Andrew Park for their valuable discussions on the experimental results.

Finally, I reserve my profoundest gratitude for my beloved wife, Shusmita Saha, whose unwavering support and companionship have been my greatest strength from the onset of my graduate research journey. I wish you all the success, today and always, as you pursue your Ph.D. at UC Merced.

May we all continue to strive towards a bright future.

ABSTRACT

Currently, anion exchange membrane fuel cells (AEMFC) are gaining strong interests from researchers because it provides great potential for applying non-precious metal in comparison to the proton exchange membrane fuel cells (PEMFC). Compared to PEMFC, AEMFC has faster reaction kinetics for the cathodic oxygen reduction reaction (ORR), which enables the utilization of non-noble catalyst. In addition, the less corrosive alkaline environment allows for low-cost stainless-steel bipolar plate. However, there are still many technical barriers related to material and transport in an AEMFC. In an AEMFC, water is generated during anodic hydrogen oxidation reaction (HOR) and is consumed during the cathodic ORR. Hydroxide ions (OH^-) are formed during ORR and carry water molecules from the cathode to the anode via electro-osmotic drag. During high current density operation, anode flooding can hinder hydrogen transport. Similarly, it may cause cathode drying leading to high ohmic loss due to reduction in membrane and ionomer conductivity. Therefore, optimizing water management in an AEMFC is essential for achieving good cell performance. Based on the HOR and ORR, the transport limitation may occur due to insufficient supply of one or a combination of hydrogen, oxygen, hydroxide ion, and water. This project, as discussed in Chapter 3, aims to examine and identify sources of transport limitations and quantify their effect under various operating conditions. Two types of flow fields are used to study the cell performance and water behavior in the cell. The membrane electrode assembly is made of alkaline membrane with high hydroxide ion conductivity and gas diffusion electrodes are fabricated with alkaline ionomer. Two gas diffusion electrodes (GDE) are prepared with solid (powder) and liquid (dispersion) ionomer binder, GDE-1 and GDE-2 respectively. The dispersion ionomer binder makes a very hydrophobic electrode that makes ion exchange difficult and results in poor performance although the membrane is sufficiently hydrated. Adding ethanol to ion exchange solution helps to improve exchange and consequently performance. It is found that higher RH is helpful to achieve better ohmic performance, but lower RH is preferred to achieve better concentration or high current density performance. So, it is obvious that the AEMFC performance is very sensitive to RH, especially on the anode side. Hydrogen and oxygen mass transport limitations are both observed from the performance measurement. However, the effect of reducing hydrogen concentration on AEMFC performance is greater than that caused by reducing oxygen concentration. Neutron experiments show that cathode gets more water at the beginning of the cell

operation, out of which most water is then transported to the anode through electroosmotic drag, the balance shifts towards anode and anode becomes flooded at some point which causes the cell performance to reduce. All these results provide valuable insights on the AEMFC water management strategies for improving cell performance and making a significant impact towards the development of AEMFC technology.

Hydrogen-powered proton exchange membrane fuel cells (PEMFC) have great potential to replace the traditional internal combustion engines due to its inherent advantages of zero greenhouse gas emissions, better fuel efficiency, quick startup, silent operation, less required maintenance, etc. In a PEMFC, oxygen transport is a critical performance limiting factor because of the sluggish oxygen reduction reaction kinetics. Limiting current method is a well-established in-situ diagnostic tool to measure the oxygen transport resistance in a PEMFC. To obtain accurate oxygen transport resistances, a few key assumptions need to be made including: (1) the effect of temperature gradient in the diffusion media is negligible, (2) no convective flow in the porous media, (3) oxygen is diluted in a gas mixture of nitrogen and water vapor, (4) the total oxygen transport resistance combines gas diffusion layer, microporous layer, and catalyst layer, (5) the effect of membrane thickness has negligible effect, and (6) the anode side does not affect the measurement results due to fast hydrogen oxidation reaction. In this project, as discussed in Chapter 4, we perform a systematic study of the effect of membrane thickness and operating conditions on obtaining robust and reliable limiting current measurements. Standard Nafion membranes of two different thicknesses (25 and 85 µm) are tested with Toray 060 and Freudenberg H23C8 diffusion media. In addition, we further study the interaction between membrane thickness and cell temperature, asymmetric pressure and relative humidity and their effects on limiting current results. Our results show that membrane thickness and relative humidity are critical factors in obtaining reliable oxygen transport resistance due to their effect on the overall water balance in the cell.

Fuel cell durability is a key limitation for its commercialization in heavy-duty applications. Cathode catalyst layers need to be designed to demonstrate not only high oxygen reduction reaction (ORR) mass activity and cell performance but also significanlt durability during long-term operation. Ion-conducting polymers, or ionomers, play a crucial role in determining both performance and durability in a PEMFC. A highly oxygen permeable ionomer (HOPI), developed by Chemours^{TM}, is explored in the project explained in Chapter 5. HOPI is known for higher ORR mass activity and lower oxygen transport resistance through its film covering the active catalyst sites. A fuel cell utilizing the HOPI ionomer in the cathode catalyst layer is compared with one using the conventional Nafion D2020^{TM} ionomer. Durability experiments demonstrate the superior durability of the HOPI ionomer.

Measurements of cathode proton resistance, oxygen transport resistance, and cell performance before and after accelerated stress tests reveal the superiority of the HOPI cell in all aspects compared to the D2020 ionomer. According to the literature, the improved cell durability and performance attributed to the HOPI ionomer are due to its higher ORR mass activity, enhanced oxygen transport through the ionomer film, and higher oxygen solubility.

TABLE OF CONTENTS

LIST OF FIGURES

LIST OF TABLES

LIST OF SYMBOLS

Chapter 1

INTRODUCTION

1.1 Background and Motivation

The concept of the greenhouse effect was first identified by the French mathematician Joseph Fourier in 1824, who noted that Earth would be significantly colder without its atmosphere [1]. This phenomenon involves the absorption and entrapment of solar heat by various atmospheric gases, including CO_2, CH_4, and N_2O, collectively known as greenhouse gases (GHGs) [2]. The negative impacts of GHG emissions on Earth's climate and human health are widely recognized. These emissions lead to global warming by trapping solar heat in the atmosphere [2]. NASA has reported that, as a consequence of global warming, the average global temperature has increased by 1.1°C since 1880, resulting in shifts in wildlife habitats, rising sea levels due to melting ice, and other environmental changes [1, 3]. The primary sources of GHG emissions are the combustion of fossil fuels such as coal, petroleum oil, and natural gas for power generation [4].

Among all GHGs, CO_2 contributes the most to the GHGs emissions. The amount of the CO_2 gas levels in the earth atmosphere is rising with an alarming rate that meticulous solution is needed to address this issue in no time soon. According to the United States Environmental Protection Agency (EPA), in 2019, CO_2 alone accounted for 80% of the total GHG emissions (from human activities) [5]. EPA also mentions that transportation sector is the major contributor to the GHG emissions in the US because it deploys fossils fuels like gasoline and diesel for powering up the vehicles; 35% of the total CO_2 emissions and 28% of the total GHG emissions are coming from the transportation sector alone [5]. The notorious effect of CO_2 is much easily understandable from the information EPA provided as: one typical passenger vehicle creates about 8.9 kg of CO_2 per every gallon of gasoline burnt [6]. Because of all these problems associated with burning fossil fuels in vehicles and other power generating devices, new technologies need to be investigated, developed, and implemented to replace fossil fuels. Fuel cells and batteries are two such promising technologies.

Fuel cells are electrochemical energy conversion devices that converts the chemical energy of fuel into electric power. Fuel cell is a clean technology since the only byproducts from the fuel cell reaction are heat and pure water; meaning no

or zero GHG emission at all. Fuel cells can be considered as open thermodynamic systems that can generate power as long as the fuel is provided to the fuel cell system. Whereas, batteries are considered to be as closed systems since they can only perform as long as they have charge inside of them. Once the charge is completely depleted, batteries need to be recharged again and charging requires significant amount of time as compared to refueling a fuel cell with hydrogen. That's why, a long-way drive is much more feasible using a fuel cell powered car as compared to a battery driven car.

Fuel cells can be categorized into five different types based on their choice of electrolytes or charge carriers and operating temperatures: i) Proton Exchange Membrane Fuel Cell (PEMFC), ii) Anion Exchange Membrane Fuel Cell (AEMFC), iii) Phosphoric Acid Fuel Cell (PAFC), iv) Solid Oxide Fuel Cell (SAFC), v) Molten Carbonate Fuel Cell (MCFC). Low temperature fuel cells like PEMFC, AEMFC offer high efficiency, high energy density, quick start-up, quick refueling time, quiet operation due to no moving parts, less or no maintenance, and high durability [7–11].

1.2 Overview of Fuel Cell Components

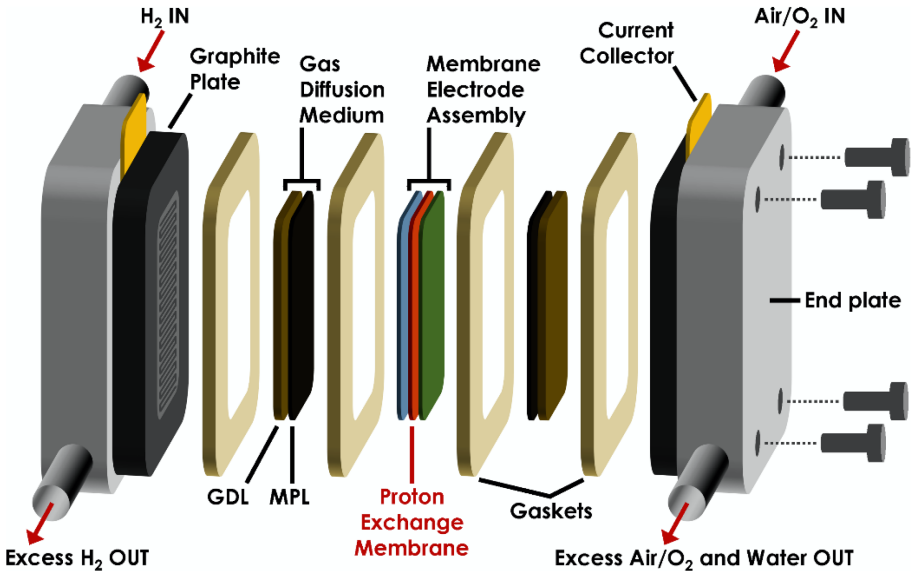

Figure 1.1: Different components of a fuel cell [12].

A fuel cell is comprised of various components: bipolar plates of flow fields (FF), gas diffusion media or layers (GDL or GDM), electrode or CL (anode and

cathode), and solid electrolyte or ion conducting membrane. The membrane and the electrodes combined are often referred to as the membrane-electrode assembly (MEA). A schematic of different fuel cell components is shown in Figure 1.1.

Flow Field (FF)

The FF performs five vital functions: i) supply of fuel and oxidant to the reaction sites, ii) removal of product water from the cell, iii) transport heat which is generated from the ORR at cathode side, iv) conduct electron from the GDM to current collector, v) provide mechanical support to the GDL [13]. The capability of the flow field to perform these five different tasks can highly affect the ohmic and concentration performance of a fuel cell [14, 15].

Uniform distribution of the reactants are essential to achieve homogeneous current density from a fuel cell, and the uniform distribution can be ensured by a well-designed flow field. A non-homogeneous current distribution in a cell can cause poor cell performance, wastage of reactant supply, degradation of cell materials, and mechanical stress in the cell [16]. 'Flooding' in a fuel cell is one of the major reasons for non-uniform current distribution. Flooding phenomena is defined as the condensation and accumulation of liquid water inside fuel cell components. This trapped liquid water blocks the pathway of the reactants traveling from the channel to the catalyst layer. Although complete flooding should be avoided but some water is necessary since too little water in the cell can reduce cell performance because proton conductivity in the membrane is solely hydration-dependent. That is why a proper water management is needed in fuel cell, and researchers are consistently investigating by modifying and altering different design parameters related to the flow field. The most popular and vastly investigated flow field designs are shown in Figure 1.2.

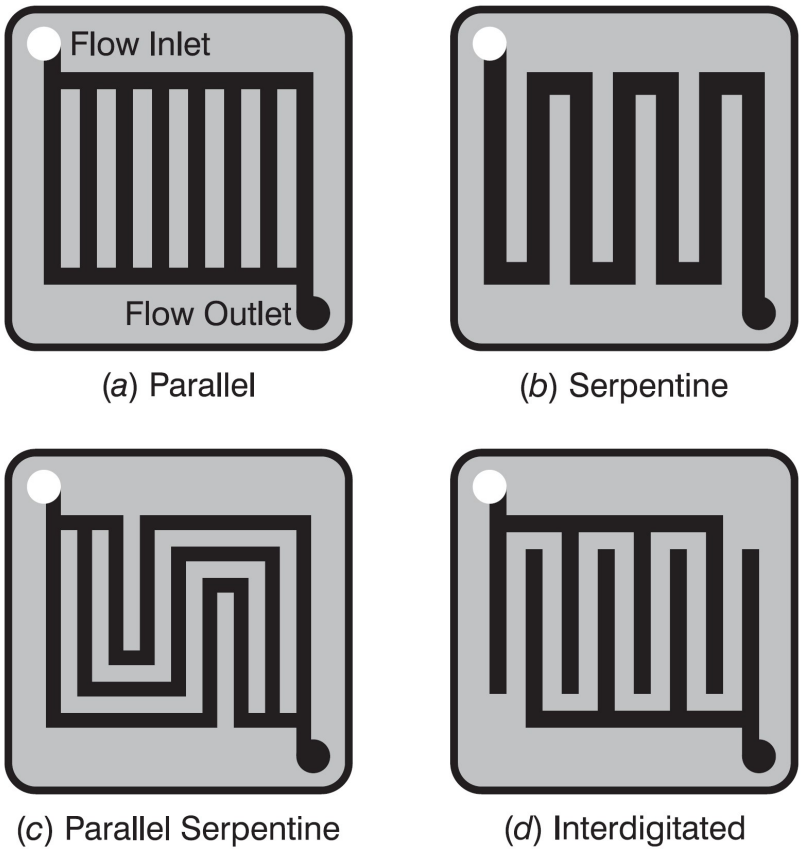

Figure 1.2: Most popular flow channel designs: (a) straight parallel, (b) single serpentine, (c) parallel-serpentine combination, (d) interdigitated [17].

The simplest design features multiple square, straight channels that flow gas in one direction across the electrode and is commonly referred to as straight parallel. My friends in Thermal and Electrochemical Energy Laboratory (TEEL, UC Merced, CA, USA) investigated this design with fuel cell experiments and three dimensional finite element simulation and thereafter published their work [18]. It was observed under conditions of high humidity the straight parallel would exhibit unstable performance likely due to slugs of water that would condense and fill the channels blocking gas transport. These results have also observed by Spernjak et al. that studied this straight parallel and two other designs in-situ [19]. The low pressure drop associated with this design makes it difficult to remove water [20]. Despite this, the straight parallel channel design remains popular because this provides more uniform conditions at the inlet and outlet.

Another common design also studied by the researchers and also TEEL is the single-channel serpentine design [18]. This design features one square channel that snakes back and forth across the electrode area, it was observed under the many

different operating conditions the single channel serpentine could effectively remove water and provide stable performance but at the cost of much greater gas pressure drop. Liu et al. compared serpentine and parallel, as well as other channel designs, at 100% RH inlet conditions and found that the serpentine flow field design had the best performance, citing pressure drop as the key reason behind this increased performance [21]. Basically, the liquid water is forced to exit from the cell since there exists only one flow path in this design. A high pressure gradient between adjacent two channels can induce cross flow under the rib, which aids in liquid water removal from the gas diffusion media [22]. However pressure drop can be beneficial for improving fuel cell performance, but it would be impractical for a fuel cell stack and system as the required pumps and compressors would drastically reduce efficiency [23]. Gas transport modes in parallel and serpentine designs are shown in Figure 1.3.

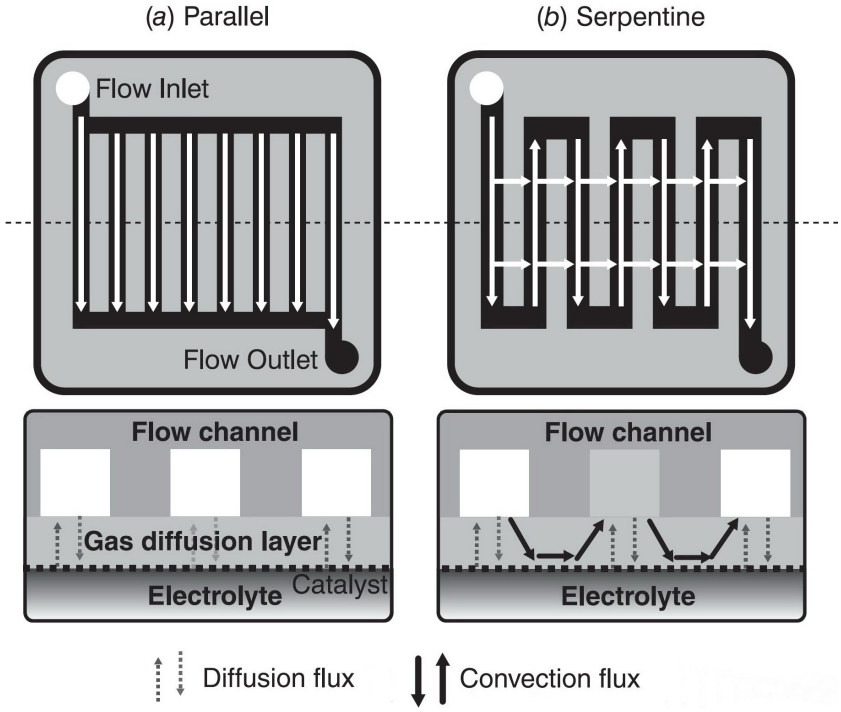

Figure 1.3: Gas transport modes in (a) parallel and (b) serpentine, flow design [17].

There exist many more flow channel designs in the research fields aside from the two as mentioned above. A hybrid of parallel channel and serpentine is the multiple channel serpentine or parallel-serpentine that yields a wider operating range [17, 18]. There is another interdigitated flow channel design that offers forced convection

of the reactant gases throough the GDM and it can provide better water management [17]. Even though interdigitated design offers better water management, it is not as popular due to demonstrating significant reactant pressure drop. We published a work investigating novel 3D-nozzle flow channel design that demonstrates lower oxygen transport resistance and thereby helps to improve the performance under wet condition [24]. Presently at the industrial level Honda Motor Co. uses a wavy design in their V-Flow stack where channels meander slightly across the electrode area [25]. Toyota uses in the Toyota Mirai a complex 3D fine mesh flow field on cathode and a simple straight parallel type design on the anode [8].

Both parallel and serpentine designs were used in the AEMFC work mentioned in this proposal, and only parallel design was used for the preliminary work related to PEMFC.

Gas Diffusion Media (GDM)

The gas diffusion layer (GDL) is usually made of carbon fiber paper, the fibers conduct electrons and heat between FF and catalyst layer (CL), whereas the porous structure allows mass transport of reactants and product water. GDL needs to be thin enough to reduce transport resistance of the reactant flow from the channel to the reaction sites, and reduce the ohmic resistance for the transfer of electrons from the reaction site to the flow field. But a too thin GDL is never recommended since GDL can loose its mechanical properties under compression. In addition, GDL should posses good thermal conductivity to transport the heat. Another function of GDL is to provide mechanical support to the MEA. To achieve a balance between good conductivity and mass transport, GDL properties such as tortuosity, porosity, permeability, and especially hydrophobicity should be meticulously chosen.

There are different types of GDL that have been tested in fuel cell research; carbon cloth [26], carbon fiber paper (CFP) [27, 28], gas diffusion electrode (GDE) or catalyst coated carbon paper [29] etc. The use of the CFP is the most common in the literature. Toray 060 and Freudenberg H23C8 are the two most common GDLs used in PEMFC research. SEM images of these two GDLs are shown in Figure 1.4. Different properties of these two diffusion medias are tabulate in Table A.1 and A.2.

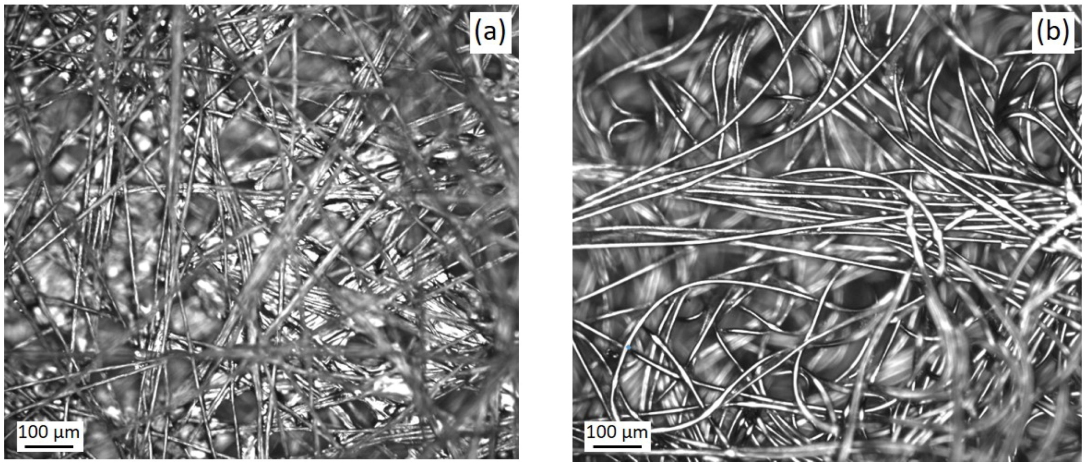

Figure 1.4: SEM images of the carbon fiber layer in (a) Toray TGP-H-060 and (b) Freudenberg H23C8. [30]

GDL plays very crucial role in fuel cell water management. Water management and flooding phenomena has been one of the most crucial performance limiting issues in fuel cell (e.g., cathode flooding in PEMFC, and anode flooding in AEMFC). The polymer membrane and catalyst layer ionomer require water to be adequately hydrated to maintain ionic conductivity. Simultaneously, water that has condensed in the CL or GDL can flood the pores and block pathways for reactant gas transport [31–33]. The flooding phenomena can occur under highly humidified or high current density condition when the amount of water exceeds the maximum capacity of vapor transport. In a PEMFC, imbalanced water in the catalyst layer can reduce the rate of cathodic oxygen reduction reaction (ORR), which already has a sluggish reaction kinetics compared to anodic hydrogen oxidation reaction (HOR), and more than two thirds of the total voltage loss happens due to this slower cathode kinetics under most operating conditions [34]. Therefore, good water management by optimizing water removal is necessary for achieving good performance from a fuel cell.

To aid with water removal and thereby to improve gas transport, the GDL is often 'wetproofed' or treated with hydrophobic agent to give it hydrophobic properties [28]. Different types of hydrophobic agents have been used in the literatures e.g. polytetrafluoroethylene (PTFE) [35, 36], fluorinated ethylene propylene (FEP) [37, 38], polyvinylidene fluoride (PVDF) [39, 40], perfuoroalkoxy(PFA) [41], perfluoropolyether (PFPE) [41]. The most common hydrophobic agent is PTFE and the most common method for wetproofing is dipping the bare GDL into the suspension of hydrophobic polymers. However, a higher PTFE loading can completely clog the GDL pores and thereby hinder oxygen transport to catalyst leading to high mass transfer limitations [26, 42, 43].

Another strategy for improving water management is the addition of a thin microporous layer (MPL) between GDL and CL [44, 45]. MPL is usually made of porous carbon black powder and hydrophobic agent. A MPL works as a capillary barrier which induces high hydraulic pressure to push the liquid water from the cathode side to the anode side ensuring better hydration or proton ion conduction through membrane. In addition, oxygen transport is enhanced due to less water saturation in the GDL or near the CL [46, 47]. The use of MPL also reduces the thermal and electronic contact resistance between GDL and CL [48, 49]. The water-managing function of MPL becomes more active under high current density condition when the cell is prone to flooding [49]. A MPL can also act as a mechanical support for CL by impeding the intrusion of the catalyst particles into the GDL pores [50].

Figure 1.5: Carbon fiber paper (dark side represents MPL, gray side represents the bare side with no MPL [30].

After adding a MPL to the carbon fiber paper, a GDL is often referred to as gas diffusion media (GDM). A commercial GDM is shown in Figure 1.5 to demonstrate the MPL and no-MPL sides. I investigated the effect of both wetproofing and MPL incorporation during my Masters in UC Merced and it was found that only increasing the PTFE loading in the GDL is not sufficient to prevent electrode flooding, rather addition of hydrophobic MPL on the cathode is crucial for performance, especially under wet conditions [51]. However, it is to be noted that wetproofing and MPL are vastly investigated in PEMFC research. Not too many studies are reported so far to crucially investigate the effect of these two methods in AEMFC.

Electrolyte

The ion conducting membrane (for example: proton exchange membrane or polymer electrolyte membrane or PEM in PEMFC, or anion exchange membrane or

alkaline electrolyte membrane or AEM in AEMFC) is a solid, organic polymer, usually perfluorosulfonic acid [52]. So, membranes provide ionic pathways for proton or hydroxide transport in PEMFC or AEMFC, respectively. An ideal membrane should possess a couple of characteristics as: (a) high ionic (e.g., proton or hydroxide) conductivity, (b) better electronic insulating capability or low electronic conductivity, (c) better mechanical and chemical integrity, (d) low fuel and oxidant crossover, (e) good stability and mechanical properties under both dry and wet condition, (f) less swelling when hydrated, and (g) low cost to manufacture.

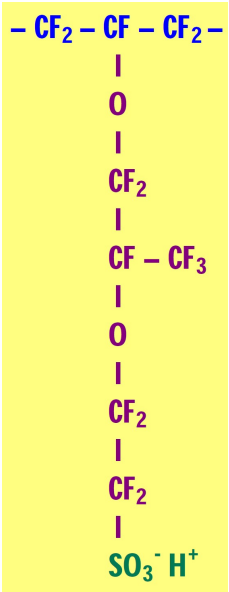

Figure 1.6: Chemical structure of Nafion™, manufactured by the Chemours™ Co. [52].

Currently, Nafion™, manufactured by the Chemours™ Co., is the most popular PEM being used in PEMFC [52]. The chemical structure of Nafion™ is shown in Figure 1.6. The negative sulfonic acid ions attached to the side chains can't move. Under hydrated condition, movement of hydrogen ions or protons occur by hopping from one sulfonic acid site to another within the membrane. The solid hydrated electrolyte is a very good conductor of protons because of this mechanism.

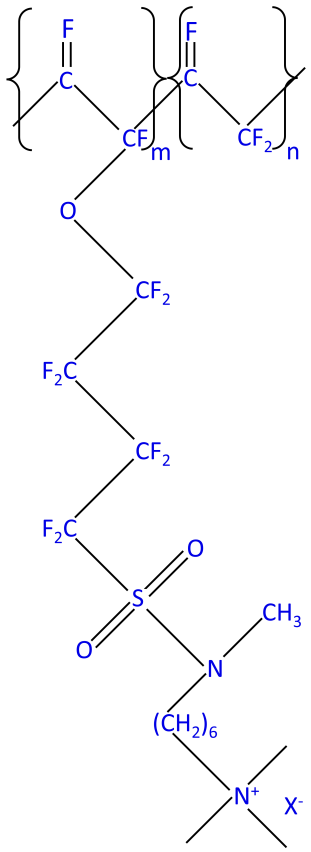

Figure 1.7: Chemical structure of Gen 2 PFAEM [53].

In our AEMFC project, as discussed in Chapter 3, perfluorinated anion exchange membrane (PFAEM), or Gen 2 PFAEM membrane was used [54]. As shown from the structure of Gen 2 in Figure 1.7, it has methylated sulfonamide linkages to the 3M backbone with six methylene groups tethered to a trimethyl ammonium cation.

Electrodes

Two of the electrodes or catalyst layers are the heart of a fuel cell where all reactions take place. Electrodes are usually made of carbon, ionomer, and catalyst. Carbon serves as an electron conductor and catalyst support, the ionomer provides pathways for conducting the ions, and the catalyst surface reduces the activation energy for the reactions. The boundary on the catalyst surface where ions are able to meet with electrons and reactant gas (for example hydrogen and oxygen) are referred to as the triple-phase boundary. It means, triple-phase boundary is where the reaction actually takes place.

Other components

Current collectors are placed with the flow field plates so that they can conduct the electron from the flow field and pass it through the external circuit. Finally, compression plates are used on the both ends to compress and ensure better contact among different cell components. Also, PTFE gaskets are used to reach to the target strain of the GDM and to ensure insulation wherever needed.

1.3 Working Principle of PEMFC

As already mentioned, a polymer electrolyte membrane fuel cell or PEMFC has a low operating temperature (<100°C) and utilizes a solid polymer electrolyte for proton exchange. Hydrogen-powered PEMFCs can play a major role as an alternative for combustion engines, or as a power source for any portable and stationary devices in the near future because of a lot of their promising features like high power density, better fuel efficiency, zero greenhouse gas (GHG) emissions, quick start-up, quiet operation, faster refueling time, and simplicity of design.

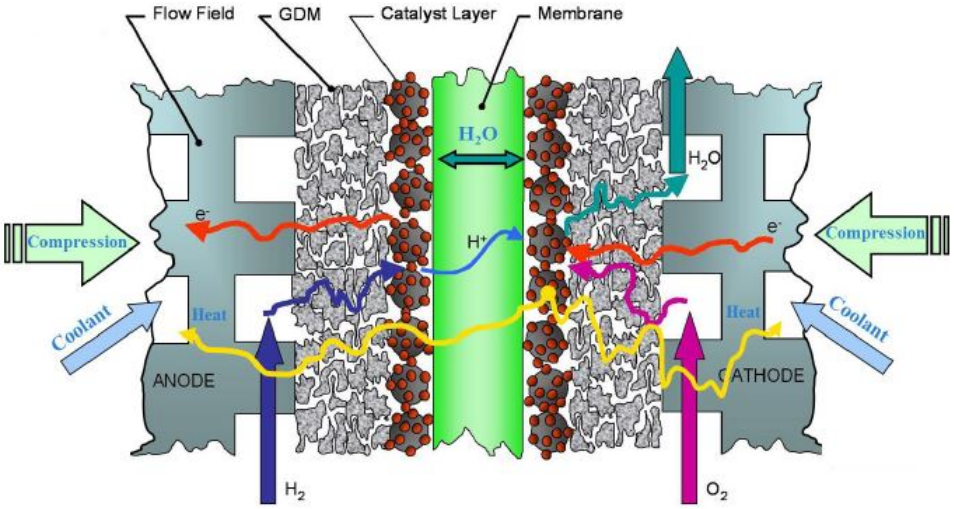

Figure 1.8: Schematic of a PEMFC cross-section (not to scale) [55].

A schematic of PEMFC cross section is shown in Figure 1.8. Two types of reactant streams (hydrogen, and oxygen or air) are supplied to either side of a PEMFC. Supplied hydrogen fuel is combined with oxygen through electrochemical reaction to produce electricity, water, and heat. In principle, at the anode electrode, hydrogen gas is reduced to hydrogen ions (H^+ or protons) and electrons. The protons are transferred to the cathode electrode through the electrolyte or ion-conducting proton-exchange membrane, and then combine with electrons and oxygen to generate product water and heat, while the electrons are flowed through an external circuit for providing power to any device connected.

In a PEMFC, the hydrogen-oxygen chemical reaction is divided into two electrochemical half-cell reactions as following:

$$\mathrm{H_2} \rightarrow 2\mathrm{H^+} + 2e^- \ (E_{ox} = 0\ V) \tag{1.1}$$

$$\frac{1}{2}\mathrm{O_2} + 2\mathrm{H^+} + 2e^- \rightarrow \mathrm{H_2O}\ (E_{red} = 1.23\ V) \tag{1.2}$$

And, the net exothermic reaction is presented as:

$$\mathrm{H_2} + \frac{1}{2}\mathrm{O_2} \rightarrow \mathrm{H_2O}\ (E_{cell} = 1.23\ V) \tag{1.3}$$

1.4 Working Principle of AEMFC

In an anion exchange membrane fuel cell (AEMFC), a solid anion-exchange membrane is used for conducting hydroxide ions instead of protons in a PEM. A schematic of the operating principle for AEMFC is shown in Figure 1.9. Like the PEMFC, hydrogen and oxygen gases are supplied on either side of the AEMFC. Hydrogen gets oxidized at the anode through HOR to produce water and electrons, whereas oxygen reacts with water at the cathode through ORR to produce hydroxide ions. The hydroxide ions are transported from the cathode side to the anode side through a hydroxide conducting anion exchange membrane. The generated electrons from the anode side travels through an external circuit to the cathode side to generate electricity.

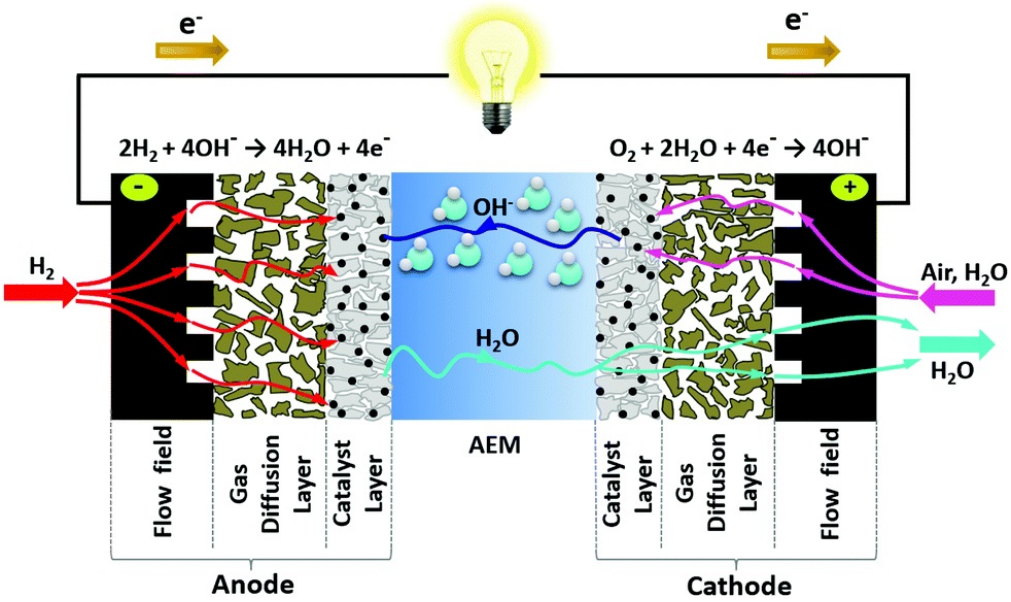

Figure 1.9: Schematic of AEMFC cross-section (not to scale) [56].

In an AEMFC, the hydrogen oxidation reaction (HOR) at anode, and oxygen reduction reaction (ORR) at cathode are shown as below:

$$2H_2 + 4OH^- \rightarrow 4H_2O + 4e^- \ (E_{red} = 0.83\ V) \tag{1.4}$$

$$O_2 + 2H_2O + 4e^- \rightarrow 4OH^- \ (E_{ox} = 0.40\ V) \tag{1.5}$$

And, the full cell reaction is written as:

$$2H_2 + O_2 \rightarrow 2H_2O \ (E_{cell} = 1.23\ V) \tag{1.6}$$

1.5 Research objectives

1.5.1 Objectives for the 'AEMFC' project (Chapter 3)

The primary objective of this research is to conduct a systematic experimental investigation to enhance the fundamental understanding of Anion Exchange Membrane Fuel Cells (AEMFC) through exploring cell performance under a broad spectrum of operating conditions and materials design. This study focuses on analyzing Toray TGP-H-060 gas diffusion electrodes fabricated from two different ionomer precursors, powder and dispersion. We utilized scanning electron microscopy (SEM) for both in-plane and cross-sectional images to examine the electrode layer structure. Through a carefully designed experiment series, we evaluated the impact of reactant concentration and operating parameters on AEMFC performance. Our findings revealed that AEMFC performance is highly sensitive to variations in relative humidity and hydrogen concentration, whereas oxygen concentration appeared less critical under the tested conditions. Furthermore, neutron radiography experiments were employed to explore liquid water transport and accumulation dynamics within the AEMFC, uncovering that water management shifts critically from the cathode to the anode during operation, leading to performance degradation when the anode becomes flooded. These insights are instrumental in developing effective water management strategies, significantly advancing AEMFC technology.

1.5.2 Objectives for the 'PEMFC limiting current' project (Chapter 4)

The objective of this research work is to perform a systematic investigation to examine the influence of membrane thickness and operational conditions on limiting current analysis. Through experimental approach, we evaluated the oxygen transport resistance across standard Nafion membranes of two distinct thicknesses (25 and 85 µm) under varying cell temperatures, pressures, and humidity levels, employing Toray 060 and Freudenberg H23C8 as gas diffusion media. Our work fills a significant gap in the current research, as there hasn't been a detailed exploration of how these factors together impact the measurement of limiting current, despite

the extensive literature on fuel cell performance. Previous studies have often focused on single factors of fuel cell operation or on the theoretical aspects of limiting current, without directly linking membrane properties and operating conditions to oxygen transport resistance. Our findings reveal that both membrane thickness and relative humidity play pivotal roles in determining accurate oxygen transport resistance, mainly due to their substantial impact on the cell's water management. Additionally, this work delves into the discrepancies observed in limiting current theories under standard conditions, shedding light on the complex dynamics of water transport and its implications for PEMFC performance. This study, by correlating experimental data with simulation outcomes, not only enriches our fundamental understanding of PEMFC operational dynamics but also sets the stage for future advancements in design and optimization strategies, ensuring accurate measurement of oxygen transport properties through limiting current experiments.

1.5.3 Objectives for the 'HOPI Ionomer' project (Chapter 5)

The objective of this exploratory project is to investigate a highly oxygen-permeable ionomer (HOPI), which is currently under research and development by Chemours^{TM}. This investigation involves using HOPI to fabricate the cathode catalyst layer of a PEM fuel cell. Cells prepared with HOPI are compared with those using the standard or conventional ionomer, Nafion D2020^{TM} (hereafter referred to as D2020). We aim to examine the impact of this newly developed ionomer on cell durability, oxygen transport in the ionomer thin film, cathode proton transport, and overall cell performance, utilizing in situ fuel cell electrochemical diagnostics. First, the durability of the HOPI cell is compared with that of the D2020 by conducting DOE 5000 MEA accelerated stress test (AST) cycles. Then, the cathode proton resistance, both before and after the AST cycles, is examined and compared. Subsequently, the oxygen transport resistance - specifically the electrode resistance - for both ionomers is compared before and after AST. Finally, the cell performance and the H_2/Air mass activities for both ionomer cells are compared. The insights gleaned from these comprehensive analyses aim to guide the optimization of ink formulation and ionomer selection, thereby enhancing the formation of catalyst layers and improving the performance and durability of proton exchange membrane fuel cells.

Chapter 2

LITERATURE REVIEW

The literature review is structured into three main sections. Initially, it examines the prevailing conditions of AEMFC technology, focusing on its strengths, challenges, strategies for water management, and the materials currently in use. Subsequently, the review addresses the issues with the existing method used to measure oxygen transport resistance in the fuel cell. The third section introduces a novel material, High Oxygen Permeable Ionomer (HOPI), and discusses its role as a catalyst material in PEMFC for assessing performance and durability. The first section aligns with the AEMFC project elaborated upon in Chapter 3. The second section pertains to the project conducted on the impact of membrane thickness and various operational conditions on the limiting current in PEMFC, detailed in Chapter 4. The third section covers the durability and performance evaluation of the HOPI ionomer, discussed in Chapter 5.

2.1 AEMFC: advantages, challenges, and water management

Fuel cells are one of the most promising technologies that has the potential to replace internal-combustion (IC) engines due to its high efficiency, high energy density, and quiet and clean operation [8, 24, 57]. Proton exchange membrane fuel cells (PEMFC) are the most studied type so far due to their maturity of the components. However, there are still many limiting issues, such as sluggish oxygen reduction reaction (ORR), mass transport issues, carbon monoxide (CO) poisoning of platinum group metal (PGM) based catalysts [58–60]. In the past few years, anion exchange membrane fuel cells (AEMFC) are gaining strong interests for its potential to reduce cost [61–63]. In an AEMFC, water is consumed and generated on the cathode and anode, respectively, and the hydroxide (OH^-) is transported from cathode to anode. A schematic of the AEMFC and the reactions associated with them are shown in Figure 2.1.

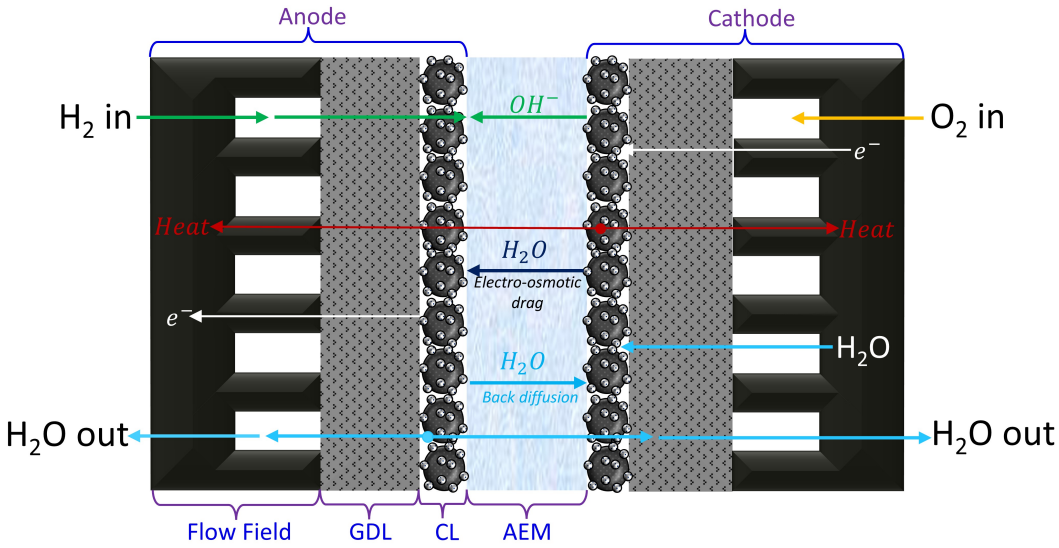

Figure 2.1: Schematic of an AEMFC.

An AEMFC provides great potential for applying non-precious metal in comparison to PEMFC [61, 64]. ORR in alkaline conditions is more facile due to its lower cathodic activation overpotential [65]. In addition, low-cost stainless steel can be used as flow field material instead of expensive materials like high-purity graphite or polymer/metal composties since corrosion of the bipolar plate is less of an issue in the high-pH alkaline environment [56, 61, 66]. The cost reduction of AMEFCs compared to PEMFCs can be substantial, since nearly 20∼30% and 25∼40% cost come from the bipolar plate and catalyst layer, respectively, in a PEMFC [67]. In addition, AEMFC offers low-cost electrolyte [68, 69], reduced CO poisoning [70], low fuel crossover [71], and broader choice of fuels [61]. However, there are many technical challenges existed related to AEMFC for achieving high power density and durable operation. These challenges mainly involve the transport of reactants, products, and hydroxide under a wide range of operating conditions. Efficient water transport and balance in an AEMFC is much more challenging than a PEMFC since water is actively participating in both anodic and cathodic reactions. In addition, there's a lack of stable ionomer and membrane that can transport hydroxide efficiently under a wide range of relative humidity conditions [72, 73]. As a result, anode flooding and cathode drying are often observed under higher current density operations, which induce severe polarization losses due to hydrogen starvation or increased hydroxide transport resistance [74].

In the past decade, the majority of AEMFC studies are related to anion exchange membrane and ionomer materials aiming to enhance hydroxide conductivity and stability [61, 75]. One major challenge is to fabricate AEMs possessing not only

high OH^- conductivity but also sufficient mechanical stability without chemical deterioration at high level of pH and temperatures [76]. In 2018, Dekel reported that significant advancements have been made in AEMs that the hydroxide conductivity in an AEM is close to that of the proton conductivity in the PEMs now [61]. Nevertheless, most experimental results published are using pure oxygen or carbon dioxide (CO_2)-free air to avoid carbonate and bicarbonate formation, which adversely affect the membrane conductivity by reducing the hydroxide diffusion coefficient [77, 78]. In addition, the operating current densities, temperature and relative humidity are often selected in ideal conditions to avoid polymer degradation [79, 80].

Some studies investigating the water management in AEMFC have been published. Omasta et al. used radiation grafted AEM to study flooding and dryout issues by changing the reactant flow rate and dew point temperatures [81]. By using both hydrophilic and hydrophobic gas diffusion layers (GDL), they showed that active water management in the cell is achievable by optimizing cell operating conditions e.g., relative humidity (RH). Kaspar et al. studied the effect of wetproofing and microporous layer (MPL) in GDL and showed that higher wetproofing loading or MPL do not help with water management to performance increment, instead they can exacerbate the situation by inducing more mass transport due to water flooding [82]. A number of modeling studies have also been published to study the AEMFC water management in recent years [73, 74, 83–88]. Sometimes, models become helpful for providing insights on relation between results and model parameter. However, not all of the published models are fully capable to capture all of the multiphysics happening in AEMFC.

Several studies investigating water management in an AEMFC have also been published. Omasta et al. used radiation grafted AEM to study flooding and dryout issues by changing the reactant flow rate and relative humidity [81]. By using both hydrophilic and hydrophobic gas diffusion layers (GDL), they showed that active water management in the cell can be achieved by optimizing relative humidity. Kaspar et al. studied the effect of wetproofing and microporous layer (MPL) in a GDL and showed that higher wetproofing loading or MPL do not help with water management for performance improvement, instead they can exacerbate the situation by inducing more mass transport resistance due to water flooding [82]. Several modeling studies have also been published in recent years to investigate water transport in an AEMFC [73, 74, 83–89]. Models are helpful for providing insights on explaining overpotentials from the experimental results, but none of the models is capable to predict the highly interactive multiphysics under a wide range of operating conditions.

In an AEMFC, transport limitation may occur due to the insufficient supply of hydrogen, oxygen, hydroxide, and water. Therefore, a systematic experimental

investigation on cell performance in a wide range of operating conditions and materials design is essential in achieving better fundamental understanding of an AEMFC. In our AEMFC work explained in Chapter 3, we studied Toray TGP-H-060 gas diffusion electrodes made from two ionomer precursors, powder and dispersion. Both in-plane and cross-sectional images were taken using scanning electron microscope (SEM) to analyze the electrode layer. A systematic design of experiments were conducted to study the sensitivity and effect of reactant concentration and operating conditions on AEMFC performance. The results indicate that the AEMFC performance is the most sensitive to relative humidity followed by hydrogen concentration. Based on our analyses, oxygen concentration is not the most critical factor in AEMFC operation. Lastly, we performed neutron radiography experiments to investigate liquid water transport and accumulation in an AEMFC. In addition, an AEMFC model is employed in this study that introduced a new approach to model two of the ohmic regions in an AEMFC polarization curve by implementing a catalyst layer flooding model. The results identify critical advancements needed for an AEMFC for the next technology breakthrough.

2.2 Effect of membrane sensitivity and operating conditions on limiting current analysis

A Proton Exchange Membrane Fuel Cell (PEMFC) is an electrochemical device designed to convert chemical energy from fuel, typically hydrogen, into electricity, with water and heat as the only byproducts. This clean energy conversion process positions hydrogen-powered fuel cells as a compelling alternative to combustion engines and as a viable power source for portable and stationary applications in the foreseeable future. The appeal of PEMFC technology lies in its array of promising features, including high power density, superior fuel efficiency, zero greenhouse gas (GHG) emissions, quick startup times, quiet operation, and a simple design structure, making it a key element in the advancement towards sustainable energy solutions [89–92].

Central to the PEMFC's operation are its major components: the flow field (FF), the gas diffusion layer (GDL), and the membrane-electrode assembly (MEA). The GDL, or gas diffusion media (GDM), typically constructed from carbon fiber and often treated with polytetrafluoroethylene (PTFE) to induce hydrophobic properties, plays a pivotal role in the fuel cell's performance [51, 93]. GDM conducts electrons and heat between the flow field and catalyst layer, and also facilitates the diffusive or convective mass transport of reactant gases through its porous structure, while simultaneously managing the removal of product water [35]. The membrane-electrode assembly (MEA) is the heart of the PEMFC, where the electrochemical reactions occur. It consists of the proton exchange membrane (PEM) sandwiched

between two electrodes - the anode and the cathode. The PEM selectively allows protons to pass through from the anode to the cathode, while electrons travel through an external circuit to generate electricity. The electrodes, coated with a catalyst, typically platinum, facilitate the hydrogen oxidation reaction (HOR) at the anode and the oxygen reduction reaction (ORR) at the cathode.

In a PEMFC, the transport of oxygen plays a pivotal role in determining overall cell performance, primarily due to the inherently slow kinetics of the ORR [94–96]. Limiting current method is a tool to measure the total oxygen transport resistance, $R_{O_2}^{Total}$ (in s/cm), in different components of a PEMFC [97–106]. It is to be noted that the transport limiting current in fuel cells manifests when oxygen concentration at the electrode approaches zero due to transport limitations, identifiable by a vertical drop in the steady-state polarization curve. However, it's crucial to differentiate this from other causes of vertical polarization, such as slow electrode kinetics or significant ohmic losses from membrane or electrode dryout [99] Distinguishing transport limiting current involves recognizing its unique signatures, ensuring accurate identification and analysis. For the derivation of precise oxygen transport resistances, several assumptions are fundamental, including: (1) the temperature gradient within the diffusion media is negligible, (2) the absence of convective flow within the porous media, (3) oxygen is diluted in a gas mixture of nitrogen and water vapor, (4) anode side has negligible impact on polarization, (5) negligible fuel crossover through the membrane, (6) negligible short circuit in the cell, (7) minimal effect from cell operating conditions, (8) a negligible influence of membrane thickness on outcomes, (9) the total oxygen transport resistance combines gas channel, gas diffusion layer, microporous layer, and catalyst layer [26, 101, 104, 107]. A detailed analysis and derivation on the limiting current method is provided in Chapter 4 to establish a fundamental understanding.

In this work, we have performed a systematic investigation to examine the influence of membrane thickness and operational conditions on limiting current analysis. Through experimental and numerical approaches, we evaluated the oxygen transport resistance across standard Nafion membranes of two distinct thicknesses (25 and 85 µm) under varying cell temperatures, pressures, and humidity levels, employing Toray 060 and Freudenberg H23C8 as gas diffusion media. Our findings reveal that both membrane thickness and relative humidity play pivotal roles in determining accurate oxygen transport resistance, mainly due to their substantial impact on the cell's water management. Additionally, this work delves into the discrepancies observed in limiting current theories under standard conditions, shedding light on the complex dynamics of water transport and its implications for PEMFC performance. This study, by correlating experimental data with simulation outcomes, not only enriches our fundamental understanding of PEMFC operational dynamics but also sets the stage for future advancements in design and optimization

strategies, ensuring accurate measurement of oxygen transport properties through limiting current experiments.

2.3 Highly oxygen-permeable ionomer (HOPI)

As already mentioned, proton exchange membrane fuel cells have shown great potential as leading clean energy conversion devices, especially for automotive applications, due to their high efficiency, zero emissions, quick startup, etc. As we move forward towards a cleaner and more sustainable future, it is crucial to conduct more intensive research for heavy-duty vehicles (e.g., trucks) to transition from diesel engines to cleaner alternatives like hydrogen fuel cells, since the high energy density of hydrogen can provide greater advantages. Researchers need to meet the stringent industry targets set by the DOE and other agencies. For example, the power density target set by the US DRIVE Fuel Cell Tech Team is 1.8 W/cm^2 by 2025 [108]. The DOE has set a target to achieve a mass activity of 0.44 A/mg^{Pt} [109]. In addition, the Million Mile Fuel Cell Truck (M2FCT) consortium has set targets of 2.5 kW/g_{PGM} power and 1.07 A/cm^2 of current density at 0.70 V after 25,000 hour equivalent accelerated stress test (AST) cycles for heavy-duty vehicles [110].

The cell performance is significantly influenced by the cathode catalyst layers because the oxygen reduction reaction (ORR) occurring at the cathode is very sluggish compared to the facile anodic hydrogen oxidation reaction (HOR). The catalyst layer is a porous structure composed of Pt or Pt alloy nanoparticles (2∼5 nm), carbon supports (10∼30 nm), and perfluorinated ionomers (3∼10 nm) [111]. A schematic of the PEMFC and the cathode catalyst layer, as obtained from the reference, is shown in Figure 2.2. Ionomers should be conductive to proton transport and non-conductive to electron transport. Thus, ionomers play a critical role in determining cell performance by ensuring the transport of protons across them while facilitating gas transport. Ionomers act as thin films that cover the carbon-supported catalysts and, therefore, contribute to the overall oxygen transport resistance. The transport resistance caused by the ionomer thin film results in a voltage drop in the cell [111]. One solution to this problem is to decrease the size of Pt nanoparticles, which essentially increases the specific surface area of the Pt. However, this method has a negative impact on cell durability because smaller particles tend to degrade more rapidly [111, 112]. Another method involves employing mesoporous carbon supports where the ionomer film cannot cover the Pt nanoparticles located inside the mesopores [111]. This approach is also not very favorable due to the absence of sufficient proton conductive pathways. Another key solution could be introducing new types of ionomers.

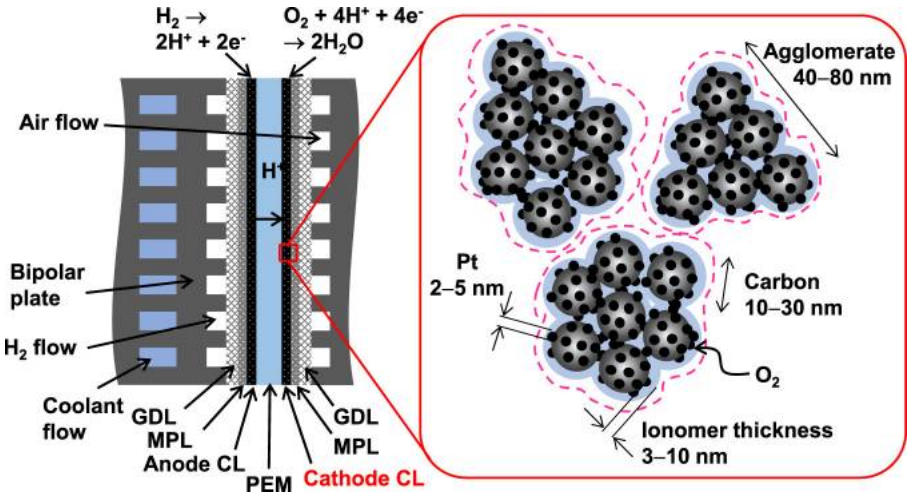

Figure 2.2: Schematic of a PEMFC along with cathode catalyst layer components [111].

Perfluorosulfonic acid (PFSA) ionomers, e.g., Nafion^{TM}, have been the most commonly used ionomer materials for both membranes and electrodes. However, using these ionomer binders in the electrode can create two issues: catalyst poisoning and high oxygen transport resistance [113]. The ORR mass activity is severely reduced due to the anion poisoning of the catalyst surface, which blocks the active Pt nanoparticle sites at all current densities, whereas the ionomer film creates severe mass transport resistance at high current densities, especially with low catalyst loading [97, 103, 113–115]. There remain two strategies to address these issues when designing ionomers for the catalyst layers. The first is to design an ionomer with a lower equivalent weight, which would reduce the oxygen transport resistance at the active catalyst sites. According to Braaten et al., the second strategy is to introduce shorter side chains that prevent adsorption to the Pt surface, thereby enhancing the ORR mass activity [113]. The highly oxygen-permeable ionomer (HOPI), developed by Chemours^{TM}, used in the project explained in Chapter 5, has a lower equivalent weight compared to the D2020 ionomer and can feature shorter side chains [111, 113, 116–118]. Therefore, HOPI exhibits high oxygen solubility and high ORR activity [113]. High oxygen solubility facilitates greater oxygen permeation through the ionomer thin film to the Pt nanoparticles, and the high ORR activity contributes to improved cell performance. As found in the literature, high ORR activity is associated with mitigated catalyst poisoning by sulfonate anion adsorption, originating from the layered folding of the ionomer backbones on the Pt surface [111].

Chapter 3

SENSITIVITY STUDY OF OPERATING CONDITIONS AND LIQUID WATER TRANSPORT BEHAVIOR IN AN AEMFC

Currently, anion exchange membrane fuel cells (AEMFC) are gaining strong interests from researchers because it provides great potential for applying non-precious metal in comparison to the proton exchange membrane fuel cells (PEMFC). Compared to PEMFC, AEMFC has faster reaction kinetics for the cathodic oxygen reduction reaction (ORR), which enables the utilization of non-noble catalyst. In addition, the less corrosive alkaline environment allows for low-cost stainless-steel bipolar plate. However, there are still many technical barriers related to material and transport in an AEMFC. In an AEMFC, water is generated during anodic hydrogen oxidation reaction (HOR) and is consumed during the cathodic ORR. Hydroxide ions (OH^-) are formed during ORR and carry water molecules from the cathode to the anode via electro-osmotic drag. During high current density operation, anode flooding can hinder hydrogen transport. Similarly, it may cause cathode drying leading to high ohmic loss due to reduction in membrane and ionomer conductivity. Therefore, optimizing water management in an AEMFC is essential for achieving good cell performance. Based on the HOR and ORR, the transport limitation may occur due to insufficient supply of one or a combination of hydrogen, oxygen, hydroxide ion, and water.

This project aims to examine and identify sources of transport limitations and quantify their effect under various operating conditions. Two types of flow fields are used to study the cell performance and water behavior in the cell. The membrane electrode assembly is made of alkaline membrane with high hydroxide ion conductivity and gas diffusion electrodes are fabricated with alkaline ionomer. Two gas diffusion electrodes (GDE) are prepared with solid (powder) and liquid (dispersion) ionomer binder, GDE-1 and GDE-2 respectively. The dispersion ionomer binder makes a very hydrophobic electrode that makes ion exchange difficult and results in poor performance although the membrane is sufficiently hydrated. Adding ethanol to ion exchange solution helps to improve exchange and consequently performance. It is found that higher RH is helpful to achieve better ohmic performance, but lower RH is preferred to achieve better concentration or high current density

performance. So, it is obvious that the AEMFC performance is very sensitive to RH, especially on the anode side. Hydrogen and oxygen mass transport limitations are both observed from the performance measurement. However, the effect of reducing hydrogen concentration on AEMFC performance is greater than that caused by reducing oxygen concentration. Neutron experiments show that cathode gets more water at the beginning of the cell operation, out of which most water is then transported to the anode through electroosmotic drag, the balance shifts towards anode and anode becomes flooded at some point which causes the cell performance to reduce. All these results provide valuable insights on the AEMFC water management strategies for improving cell performance and making a significant impact towards the development of AEMFC technology.

3.1 Experimental details

3.1.1 Membrane and ionomer preparation

Sulfonamide-linked alkyl ammonium perfluorinated Gen 2 polymer was used as both membrane and ionomer material to fabricate membrane electrode assemblies (MEAs) for fuel cell testing. The membranes were solvent cast by dissolving and stirring polymer in N,N-Dimenthylacetamide (DMAc) at 120°C for a minimum 2 hours to make 10 wt.% solutions, which were then drop casted on a Teflon sheet, followed by drying in an oven at 60°C to form membranes with a thickness between 50-55 µm and an approximate area of 50 cm^2. Membrane annealing was done by a heated platen press at 160°C and 800 psi for 10 minutes. The detailed synthesis and characterization of Gen 2 ionomer and membrane were reported previously [53, 54].

3.1.2 MEA fabrication

Catalyst ink mixing and coating process are known to have a significant impact on fuel cell performance and durability [119–121]. In this study, two different forms of ionomer were used, liquid (dispersion) and solid (powder) ionomer, both based on Gen 2 polymer. The ionomer solutions were prepared 10 wt.% from 1:1 deionized (DI) water (ultra-pure deionized water with a resistivity of 18.2 MΩcm) and n-propanol dispersion, analogue to Nafion dispersion. The catalyst ink was prepared by mixing platinum on Vulcan carbon catalyst (40 wt.% Pt, Alfa Aesar HiSPEC 4000), 10 wt.% ionomer solutions, DI water, and 2-propanol to yield a final ink weight composition of 5:12:8 for ionomer, carbon, platinum, respectively. For powder ionomer, the Gen 2 solid ionomer was grinded finely with agate mortar and pestle, followed by mixing with platinum on Vulcan carbon (Alfa Aesar HiSPEC 4000) and dispersed in DI water and 2-propanol. The dried ionomer catalyst mixture was further grinded for additional 10 minutes to avoid aggregated particles. The process of preparing catalyst ink using the solid ionomer was done similar to those processes reported by Mustain et. al. [81, 122]. The processes of making the GDE for both ionomers are similar. The catalyst mixture was tip sonicated for

20 seconds, followed by bath sonicating in ice for 20 minutes before hand spraying catalyst layer directly onto a gas diffusion layer (GDL, Toray TGP-H-060 with 5 wt.% PTFE). Platinum loading was measured by an energy dispersive X-ray fluorescence (EDXRF) spectrometer and is 0.64 and 0.54 mg cm^{-2} for GDE-1 (powder typer ionomer) and GDE-2 (dispersion type ionomer), respectively.

3.1.3 Fuel cell experiments

Before cell assembly, the Gen 2 membrane and GDE were submerged in fresh 1M KOH solution for 20 minutes for OH^- exchange. The exchange process was repeated for a minimum of two times to maximize the OH^- content. We explored the performance of two distinct flow field designs in fuel cells, both fabricated from POCO Graphite: a single-channel serpentine (SS) flow field, with a total channel area of 5 cm^2, and a straight parallel (SP) flow field, with a total channel area of 4 cm^2. In each case, the total channel area was masked down to an active area of 2 cm^2 by employing PTFE gaskets. Additionally, the use of PTFE gaskets in the cell plays a crucial role in preventing gas leakage. For neutron experiment, a special design straight parallel flow field was made by 6061 aluminum alloy with an active area of 1.33 cm^2. The hardware was gold plated to reduce electrical contact resistance and avoid corrosion.

All assembled fuel cells were tested using a Greenlight G20 fuel cell test station which was coupled with Gamry Reference 3000 and 30k Booster for performing eletrochemical impedance spectroscopy (EIS). The purpose of EIS is to measure the cell high frequency impedance (HFR). The cell was heated to 60°C with fully humidified H_2 and N_2 flow in the anode and cathode, respectively. Then, the flow was switched to O_2 at the cathode side and a constant cell voltage of 0.50 V was applied for the break-in process at a backpressure of 131 kPa. The break-in process is sensitive to the material set and operating conditions and the current density can take hours to reach plateau [18]. Pressure cycling tests between 131 kPa and ambient pressure was found to be helpful in removing channel liquid water if flooding is an issue during the break-in process. After the cell was successfully broken-in, a series of testing protocols were performed to evaluate the cell performance under different cell operating conditions as listed in Table 3.1. For dynamic conditions, the polarization curve was measured using linear sweep voltammetry (LSV) method by sweeping voltage from OCV to 0.10 V at a scan rate of 10 mV s^{-1}.

Test protocols for fuel cell experiments in the laboratory are tabulated in Table 3.1.

Test Name	Inlet RH (%)	Reactants (An/Ca)	Flowrate (NLPM)	H_2 Conc. (%)	O_2 Conc. (%)	Load Control (NLPM)
Break-in	92	H_2/O_2	0.10/0.10	100	100	0.50 V Hold
RH Sensitivity (Dynamic)	92, 80, 73	H_2/O_2	0.40/0.40	100	100	OCV → 0.20 V (10 mV/s)
RH Sensitivity (Steady-state)	92, 80	H_2/O_2	0.40/0.40	100	100	OCV → 0.20 V (5m hold at each vol.)
H_2 Sensitivity (Dynamic)	92	$(H_2+N_2)/O_2$	0.40/0.40	10, 50, 100	100	OCV → 0.20 V (10 mV/s)
O_2 Sensitivity (Dynamic)	92	$H_2/(N_2+O_2)$	0.40/0.40	100	10, 50, 100	OCV → 0.20 V (10 mV/s)
H_2 Sensitivity (Steady-state)	80	$(H_2+N_2)/O_2$	0.80/0.40	2,4,6,8,10,15,20,25,30	100	0.30 → 0.10 V (2m hold at each vol.)
O_2 Sensitivity (Steady-state)	80	$H_2/(N_2+O_2)$	0.40/0.60	100	2,4,6,8,10,15,20,25,30	0.30 → 0.10 V (2m hold at each vol.)

Table 3.1: Test protocols for the AEM fuel cell experiments (cell temperature= 70°C, cell backpressure= 131 kPa abs.).

3.1.4 Detailed Ion-exchange process

Before assembling a GDE-MEA for fuel cell testing, two GDEs (either a set of two GDE-1 or a set of two GDE-2) and a PF AEM Gen-2 membrane were exchanged in 1M KOH solution for a total of 60 minutes at the least, replacing with new base solution every 20 minutes to maximize the transfer of OH^- content. The membrane was sandwiched between two GDLs and pressed together, secured, in a Fuel Cell Technologies hardware between either two single pass serpentine or two straight-parallel flow graphite plates using 6-mil PTFE gaskets to obtain a 25% compression for the GDEs. The assembly was torqued in incremental steps to a total of 40 in-lb.

3.1.5 Cell break-in or activation

A break-process is always required to carry out after connecting the cell to the test station for activating the catalyst layer and get the cell ready to deliver performance. The break-in procedure is carried out under highly humidified conditions to keep the membrane hydrated, and for the formation of ion transporting domains in the Gen 2 membrane. It also helps in removing the carbonate or bicarbonate ions that were formed during the time of cell assembly due to the exposure of cell materials to the CO_2 in the open air.

For the break-in, H_2 and N_2 were flown through anode and cathode at 0.40 normalized liter per minute (NLPM) each side, and cell temperature was ramped up to 70°C in a way so that the relative humidity (RH) of the cell is never less than 100%. Thus, proper hydration at the beginning was ensured to avoid any membrane or ionomer degradation caused from dehydration. Then, the N_2 was switched to O_2 at the cathode side. An absolute back-pressured of 131 kPa was applied afterwards. After OCV was stabilized, a constant cell voltage of 0.50 V was applied to initiate break-in process for activating the catalyst layer. Break-in usually takes around

an hour to plateau the current density, when using the serpentine channel design. Most cells that are assembled with straight channel flow field experienced the issue of having very low current, which is assumed to have happened due to the higher water retention behavior of the straight channel design, causing from low pressure-drop characteristics [18]. A couple of pressure cycling tests (e.g., switching the pressure between 0 and 31 kPag) were found to be helpful to elevate the current density and reach to a plateau. After the cell was successfully broken-in, a series of testing protocols were performed to evaluate the cell performance under different cell operating conditions. For dynamic conditions, the polarization curve was measured using linear sweep voltammetry (LSV) method by sweeping voltage from OCV to 0.10 V at a scan rate of 10 mV/s. In order to have a consistent starting point, the cell was equilibrated at each RH or flow conditions for at least 10 minutes at 0.50 V before its polarization data was recorded.

3.1.6 Neutron radiography

Neutron radiography is an effective diagnostic tool for quantifying liquid water in an operating fuel cell [123]. In this work, neutron imaging experiments were done to investigate the through-plane liquid water distribution at the National Institute of Standard and Technology (NIST) [124]. Detailed layout with camera setup at the NIST facility can be found from literature [125, 126]. An Andor NEO scientific complementary metal-oxide-semiconductor (sCMOS) camera with a pixel pitch of 6.5 μm was used [127]. Specially designed fuel cell hardware was used for the neutron experiments. A straight-parallel channel design flow field was fabricated using 6061 aluminum alloy to ensure low neutron attenuation, and thereafter coated with gold for providing high electrical conductivity with corrosion-resistance. The flow field contained a total of 11 channels, and each channel had width of 0.635 mm and height of 0.890 mm. The fuel cell was operated using a custom-built fuel cell test station manufactured by Micro Instrument Corporation. To increase the spatial resolution and reduce noise, three neutron images with an exposure time of three minutes were filtered and averaged. To quantify the through-plane distribution, the water thickness is calculated at each pixel based on the Beer-Lambert law [128]. The water beneath cell lands and channels are distinguished by columnizing the image and taking average water thickness for columns coinciding with the center of a land. The final images are false-colored for better contrast and visualization. Detailed image processing steps can be found in the literature [125, 126, 129].

For neutron experiments, GDE-1 and GDE-2 were exchanged using KOH following the steps mentioned previously. In addition, another sample of GDE-2 was exchanged with ethanol added KOH to see if the addition of ethanol helps with cell performance improvement since GDE-2 demonstrated poor performance

as compared to the GDE-1. The cell configurations for neutron experiments are shown in Table 3.2.

Cell No.	GDE Type	Membrane	Flow field
3	GDE-1 (KOH)	Gen 2	SP-NIST 1.33 cm^2
4	GDE-2 (KOH)	Gen 2	SP-NIST 1.33 cm^2
7	GDE-2 (Ethanol+KOH)	Gen 2	SP-NIST 1.33 cm^2

Table 3.2: Cell configuration for neutron radiography experiments.

Neutron experiments were carried out for changing flow, RH, and reactant concentration. The test protocols for neutron experiments are listed in Table 3.3. The sequence here is for better understanding and to quickly explain the elimination of GDE-2 from further discussion. It is to be noted that RH-sweep was actually the last test to be carried out as low RH resulted in unrecoverable performance.

Test Name	Inlet RH (%)	Reactants (An/Ca)	Flowrate (NLPM)	H_2 Conc. (%)	O_2 Conc. (%)	Load Control (NLPM)
RH Sweep	100∼50	H_2/O_2	0.50/0.50	100	100	0.30 V Hold
H_2 Sensitivity	90	$(H_2+N_2)/O_2$	0.50/0.50	2,5,10,50,100	100	0.30 V Hold
O_2 Sensitivity	90	$H_2+(N_2+O_2)$	0.50/0.50	100	2,5,10,50,100	0.30 V Hold

Table 3.3: Test sequences for neutron radiography experiments (cell temperature= 70°C, cell backpressure= 135 kPa abs.).

3.2 Experimental results and discussion

3.2.1 Structure of Gas Diffusion Electrodes

To evaluate the structure of the gas diffusion electrode, surface and cross section SEM images were taken for both GDEs as shown in Figure 3.1 and 3.2, respectively. Since there is no microporous layer, the carbon fiber structure of Toray GDL can be clearly observed. Both GDEs show large pores in the catalyst layer demonstrating non-uniform coverage and distribution of the catalyst layer. With the ink spraying process, it can be assumed that a significant amount of Pt catalysts fall into the 100-µm sized pores of the carbon fiber paper. In addition, significant agglomeration of the catalyst and ionomer in the order of 50 µm diameter can be observed for both GDEs, especially for the dispersion type ionomer (GDE-2).

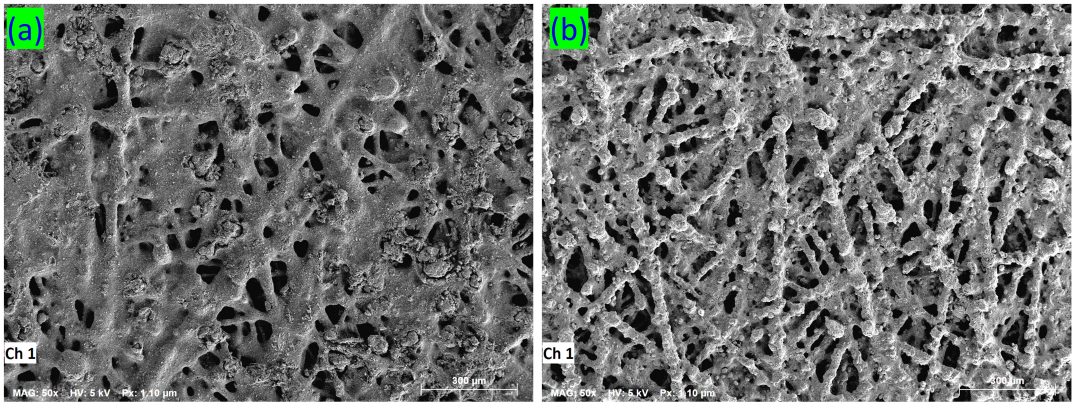

Figure 3.1: SEM surface images showing the structure of catalyst layer on Toray paper of (a) GDE-1 and (b) GDE-2.

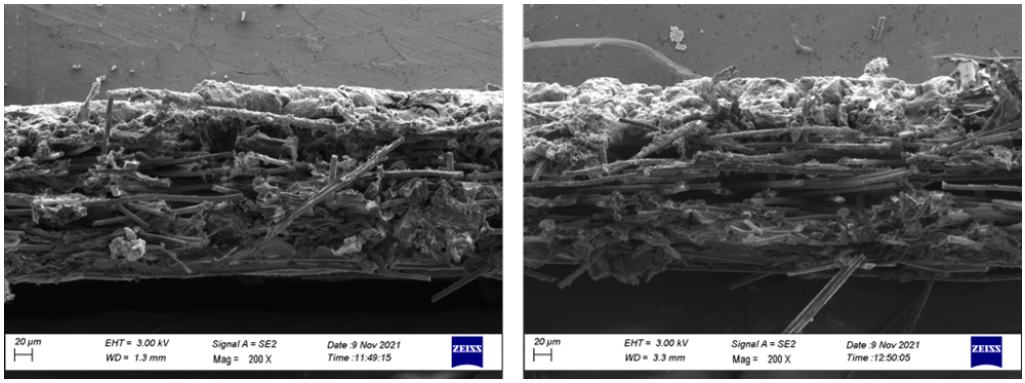

Figure 3.2: SEM cross-section images of (a) GDE-1 and (b) GDE-2.

To study elemental mapping and distribution, Energy Dispersive X-ray Spectroscopy (EDS) analysis were done based on the SEM top-down images as shown in Figure 3.3. The EDS data are tabulated in Table 3.4. A few major differences between GDE-1 and GDE-2 can be observed from the EDS results.

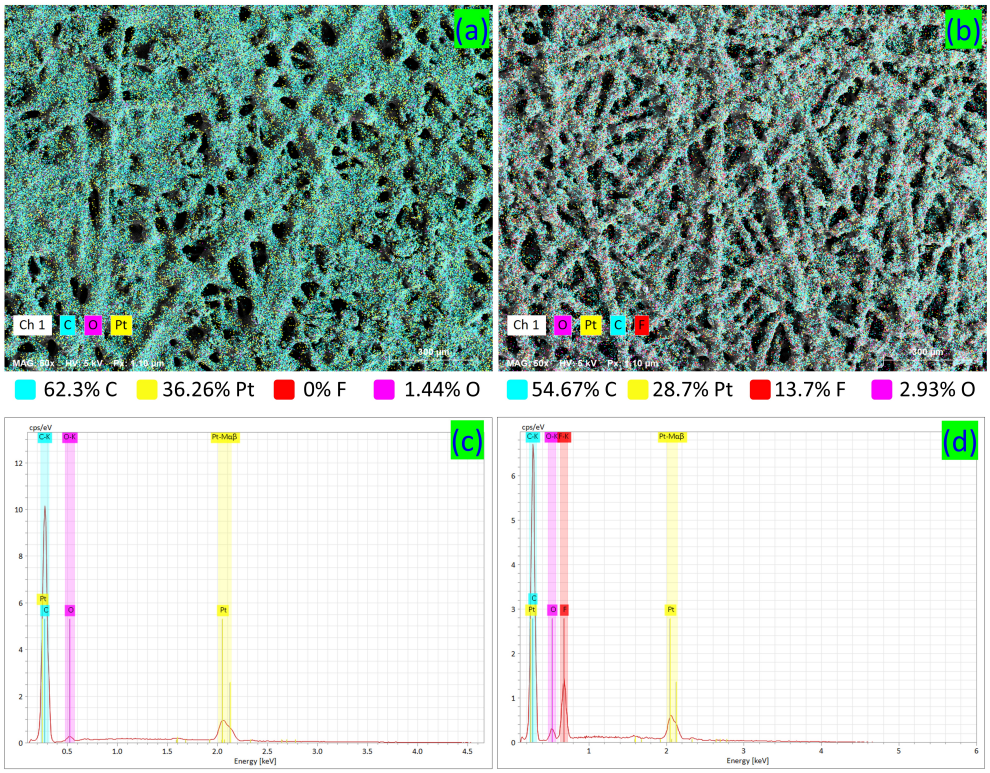

Figure 3.3: EDS mapping for (a) GDE-1, (b) GDE-2, EDS analysis showing the peaks for (c) C, Pt, and O in GDE-1, and (d) C, Pt, F, and O in GDE-2.

Sample name	C (%)	Pt (%)	F (%)
GDE-1 (powder)	62.3	36.3	0
GDE-2 (dispersion)	54.7	28.7	13.7

Table 3.4: EDS mapping data.

During the ion exchange process in KOH, GDE-2 electrode surface is seemed to be super hydrophobic because no trace of KOH solution is seen on the surface after an hour of ion-exchange process. Higher hydrophobicity for GDE-2 is also confirmed from the EDS mapping. For GDE-2, 13.7% of the detected signal comes from F (which is an indicator of PTFE or hydrophobic element), whereas no F signal is detected for GDE-1. A straightforward contact angle experiment using DI water, as shown in Figure 3.4, is also carried out and it is confirmed that GDE-2 surface is very hydrophobic as compared to GDE1 surface. Water contact angle is 149° for GDE2 as compared to 112° for the GDE-1.

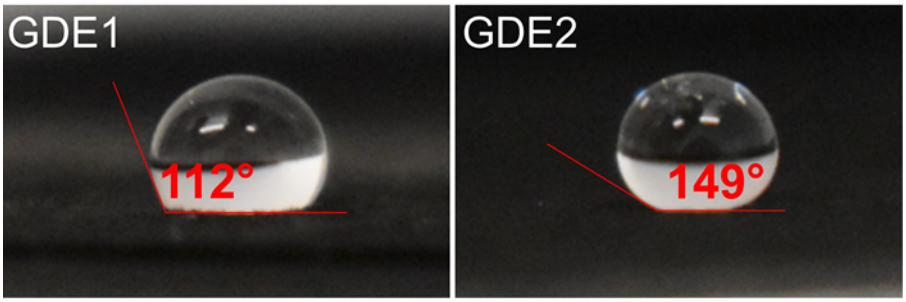

Figure 3.4: Illustration of the comparison of hydrophobicity between (a) GDE-1 and (b) GDE-2.

During the breakin process, as shown in Figure 3.5, breakin performance for cell assembled with GDE-2 is poor as compared to the cell assembled with GDE-1. Breakin current density of about 0.40 A cm^2 at 0.50 V for a healthy cell using GDE-2 is obtained, whereas the breakin current density is about 1.80 A cm^2 at 0.50 V for a healthy cell using GDE-1. The poor performance with GDE-2 is potentially because to the poor ion-exchange due to the surface being so hydrophobic.

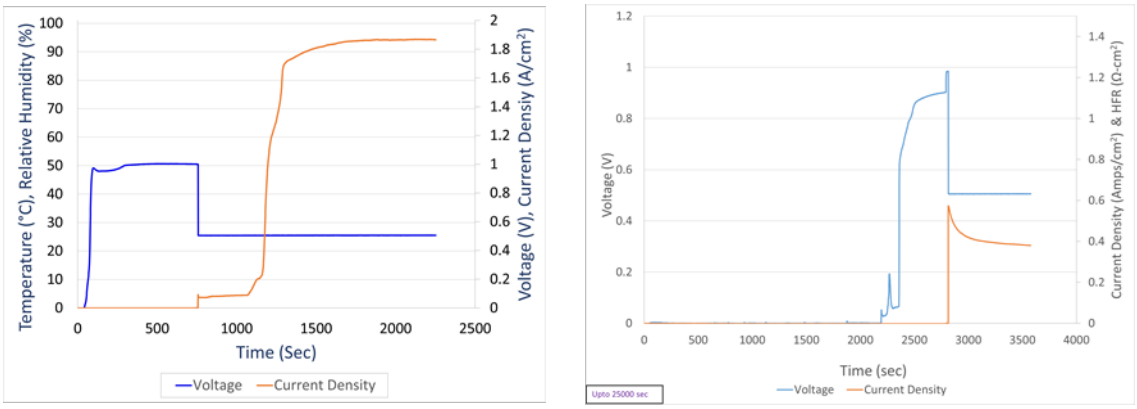

Figure 3.5: Fuel cell breakin performance curves for (a) GDE-1 and (b) GDE-2. Cell operating conditions: 70°C, 131 kPaa., 0.40/0.40 NLPM H_2/O_2, 0.50 V potentiostatic load control.

3.2.2 Sensitivity results from fuel cell experiments

3.2.2.1 Study of different ionomer materials

The AEMFC performances are evaluated and compared between GDE-1 (powder type ionomer) and GDE-2 (dispersion type ionomer). As shown in Figure 3.6, GDE-1 has superior performance under all RH conditions as compared to that of GDE-2. The key contributor to the poor performance of GDE-2 is due to its much higher ohmic resistance (HFR), especially under dry condition. The

increased HFR can be attributed to higher electrical and hydroxide transportation resistances. Based on the EDS analysis, GDE-2 shows much higher Fluorine content on the surface, which results in high electrical contact resistance. In addition, the increased hydrophobicity of GDE-2 surface may hinder OH^- exchange during the sample preparation process, which reduces the utilization of hydroxide transport sites [53]. The combined effects explain why the HFR is higher under 92% RH due to increased electrical contact resistance and the drastic increase of HFR under 73% RH due to the loss of OH^- conductivity in the electrode. Since the cells with GDE-2 do not perform well, our study is mainly focusing on the results obtained from powder type ionomer. Even though the dispersion type ionomer didn't perform well in our study, it is possible that its performance may be improved through catalyst ink or process optimization.

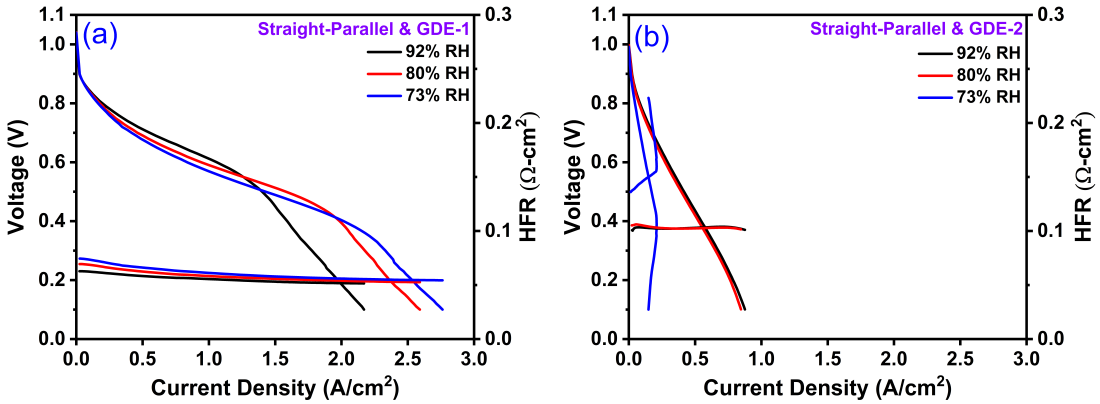

Figure 3.6: Dynamic performance curves for cells using straight parallel flow-field using (a) GDE-1 and (b) GDE-2 under three different RH (92, 80, and 73%). Cell operating conditions: 70°C, 131 kPaa., 0.40/0.40 NLPM H_2/O_2.

Overall, the cell with GDE-1 perform relatively well when the RH ranges from 73% to 92%. Even though the HFR increases with reducing RH due to dehydration, the mass transport loss improves significantly at high current density as shown in Figure 3.6(a). The results demonstrate that the AEMFC performance is very sensitive to RH as liquid water can easily flood the catalyst layer and dry out can significantly increase OH^- transport resistance in the catalyst layer.

3.2.2.2 Study of relative humidity under dynamic conditions

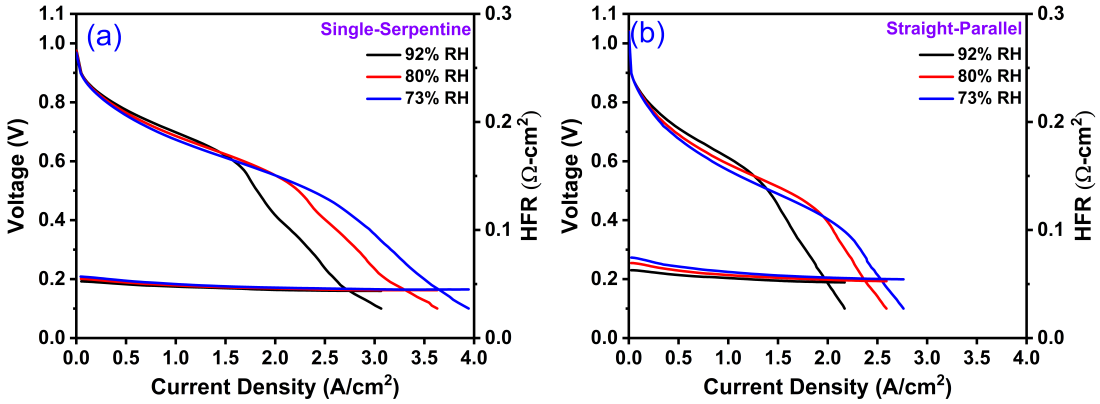

Figure 3.7: Dynamic performance curves under three different RH (92, 80, and 73%) conditions using (a) single serpentine and (b) straight parallel flow field design. Cell operating conditions: 70°C, 131 kPaa., 0.40/0.40 NLPM H_2/O_2.

The impact of relative humidity is examined again in Figure 3.7, but this time for two different flow field designs: single-serpentine (SS), as shown in Figure 3.7(a), and straight-parallel (SP), as shown in Figure 3.7(b). It is observed that performance is very sensitive to the RH for both channel designs. Out of the two FFs, SS design clearly outperforms the SP design. The higher pressure drop between inlet and outlet, associated with SS design as compared to the SP design [18], might have helped SS design to improve performance by alleviating electrode flooding through active water removal.

With this material under the operating conditions, for both FFs, ohmic performance improves with increasing the RH. This is because higher hydration or RH is helpful for increasing membrane and ionomer conductivity. Although increasing RH improves ohmic performance, but this significantly reduces the peak current density (from 4.30 A/cm^2 to 3 A/cm^2 for SS, and from 2.8 A/cm^2 to 2.2 A/cm^2 for SP), meaning that operating the cell under lower RH is helpful for concentration or high current density performance. Even though less water is available in the membrane-electrode interface due to low RH, sufficient water is provided from the cell reaction under high current density. This makes an active water balance in the cell that becomes helpful to improve the cell performance under high current density operation at low RH.

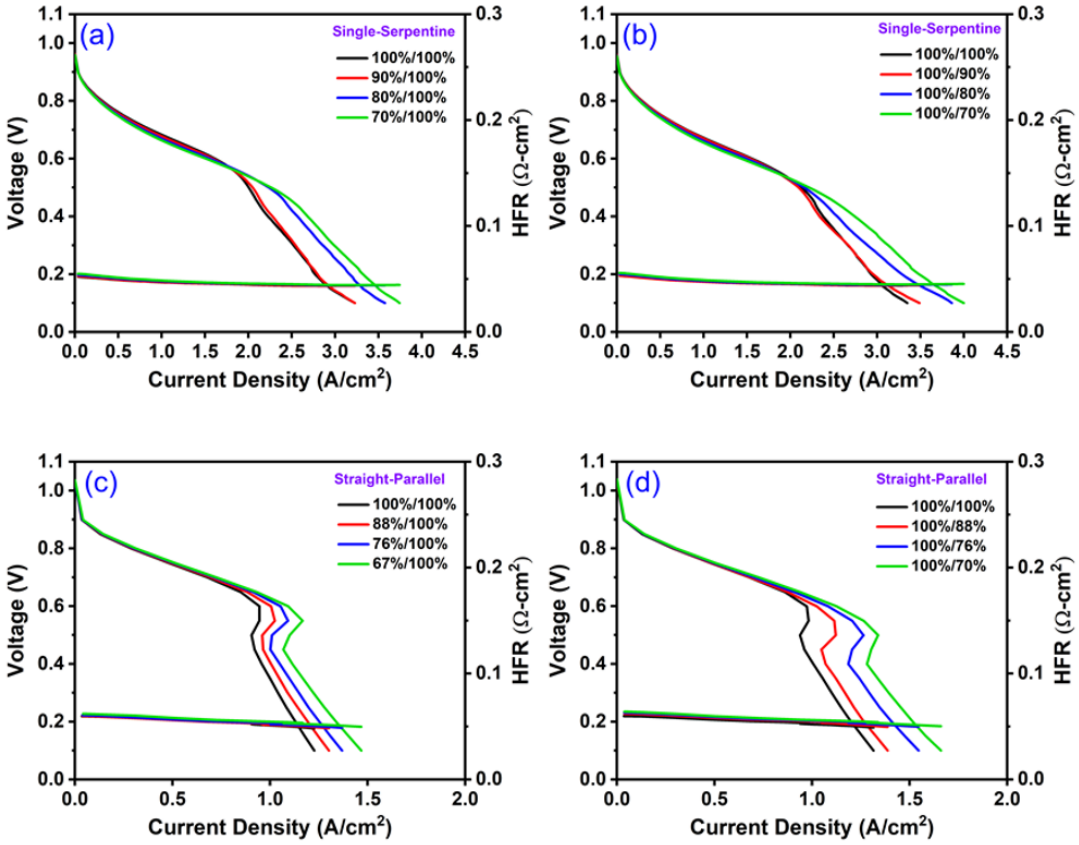

Figure 3.8: Fuel cell performance curves under (left) asymmetric anode and (right) asymmetric cathode RH conditions using (a,b) single serpentine and (c,d) straight parallel flow field. Cell operating conditions: 70°C, 131 kPaa., 0.40/0.40 NLPM H_2/O_2.

To further investigate RH sensitivity for both flow fields, we also studied the effect of asymmetric anode and cathode RH, as shown in Figure 3.8. After changing RH independently at anode and cathode, the observation is similar to the above symmetric RH study. The results for both flow fields are very similar, which suggest that both anode and cathode has similar RH sensitivity. A drier cathode appears to be slightly better than a drier anode for performance improvement. Omasta suggests that anode flooding could be relieved by the cathode [81]. However, based on our later neutron observations (min by min) under steady state at 100% RH suggests this effect is limited; the cathode can provide some alleviation but has its own limit to the amount of water it can carry.

3.2.2.3 Study of relative humidity under steady-state conditions

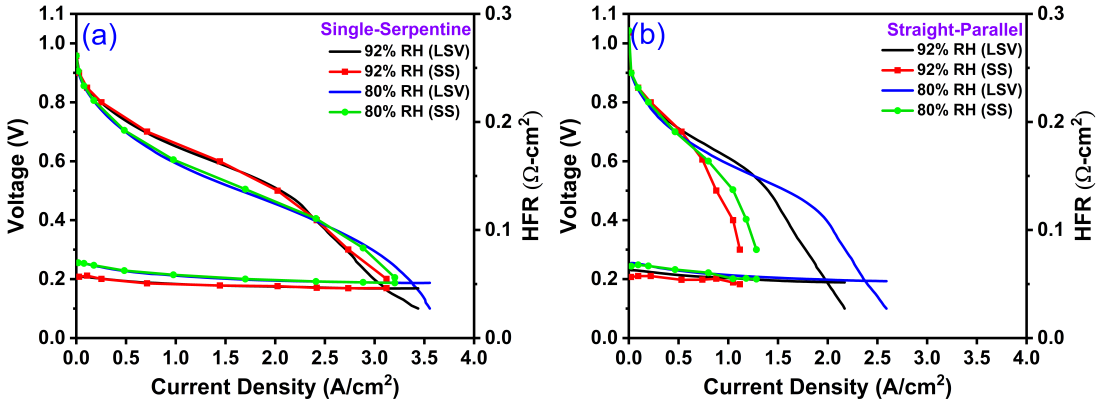

Figure 3.9: Steady-state performance curves under two different RH conditions using (a) single serpentine, and (b) straight parallel flow field. Cell operating conditions: 70°C, 131 kPaa., 0.40/0.40 NLPM H_2/O_2.

As shown in Figure 3.9, steady-state fuel cell performances are also evaluated to investigate the cell behavior under water rich condition for both FFs. For steady-state experiments, the cell is controlled at each potential for 30 min to obtain the polarization curve. The steady-state performance was measured only down to 0.30 V (i.e., not down to 0.10 V as the LSV) to prolong the cell life by avoiding any degradation of cell materials under high current density. In addition to that, cell was not tested any RH lower than 80% to avoid membrane or ionomer degradation that can be caused from long-term dehydrated cell operation.

As shown in Figure 3.9(a), steady-state performance matches well with the dynamic performance for the SS design. So, the water management for SS design is similarly efficient for operation under both short-term and long-term operation. But, as shown in Figure 3.9(b), significant performance loss under steady-state condition is observed for the SP design. This may be because of the increased water retention or flooding associated with the SP design [18]. It also may have occurred due to higher steady-state hold time of 30 mins at each potential. It may also be because of cell degradation incurred during dryer conditions between protocols. So, water appears to be the prime limiting factor to cell performance.

3.2.2.4 Study of reactant sensitivity under dynamic conditions

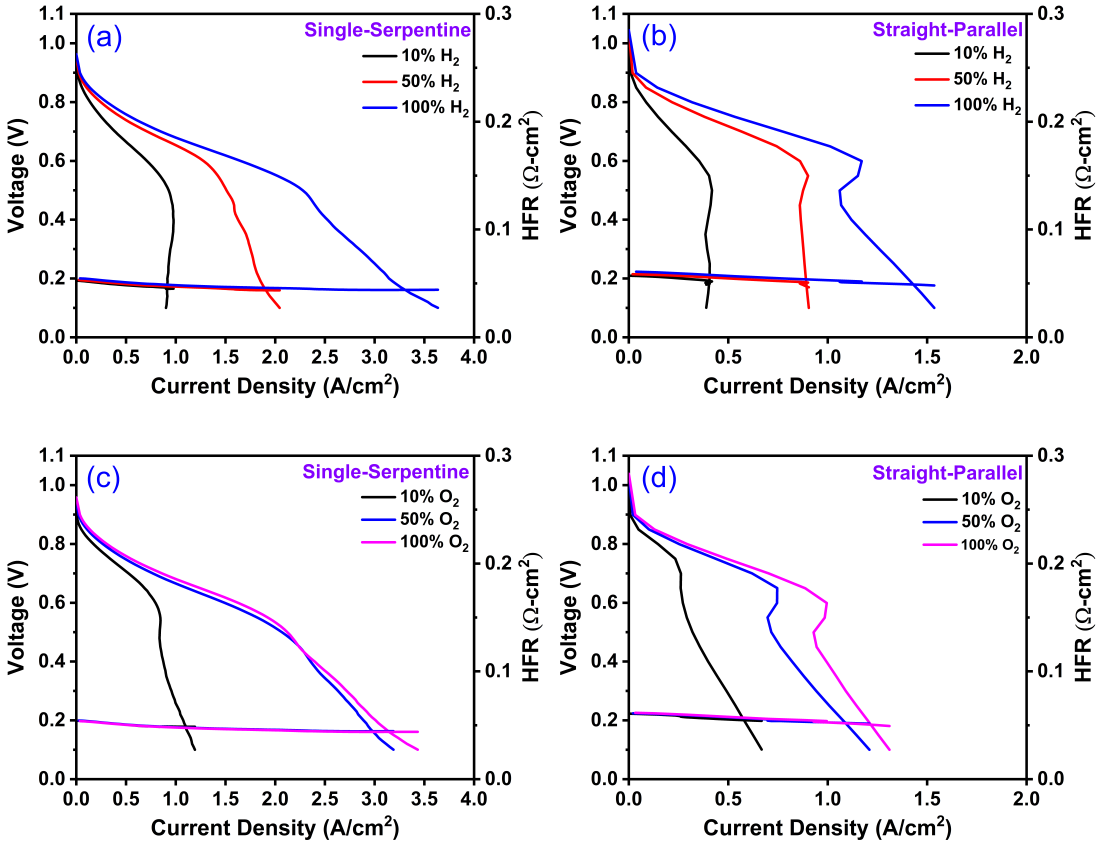

Figure 3.10: Dynamic performance curves for (top) hydrogen and (bottom) oxygen sensitivity tests using (a,c) single serpentine, and (b,d) straight parallel flow field. Cell operating conditions: 70°C, 92% RH, 131 kPaa., 0.40/0.40 NLPM H_2/O_2.

The performance sensitivity under reduced hydrogen or reduced oxygen concentration are studied for both flow fields, as shown in Figure 3.10. It is clearly seen that the impact of reducing hydrogen concentration has a stronger effect on an AEMFC performance than that caused by reducing the oxygen concentration. This observation is consistent with the findings from Gottesfeld et al. [69] that HOR overpotential is more significant than the ORR in an AEMFC. Or, in other words, the alkaline HOR kinetic reaction is not as facile as the acidic HOR. This however only explains the differences between concentrations at the lowest current densities. This 'reactant sensitivity' observation is an important one as it elucidates the extent to which water on the anode is impacting the cell performance. Examining hydrogen reactant sensitivity, it is observed that the cell performance clearly follows the

hydrogen concentration.

From oxygen sensitivity study, the increase in concentration does not necessarily correspond with an increased current density. One would normally expect the onset of concentration polarization should occur at a higher current density for a higher oxygen concentration. But water blockage is limiting the performance at higher current density. For, serpentine design, a high oxygen concentration (e.g., 100% O_2) has nearly the same performance as a low oxygen concentration (e.g., 50% O_2). For parallel design, the i-V curves for higher concentration still appear closer together. The conclusions we can draw from these two reactant studies is either i) water generation and an accumulation of it on cathode limits the cell performance, or ii) that the change in oxygen concentration has little effect because the maximum performance have already been capped by water present on the anode.

What can lend credit to the second conclusion here is the 'knee' observed in the polarization curves during testing with straight parallel flow field. By 'knee', we mean the inflection in the current density happening at somewhat 0.60 V. Similar behavior for the same material have also been reported by Omasta et al. and was attributed to water flooding [122]. The possible explanation could be that the water generation is greater than the vapor water removal capacity at these conditions, the heat generation and water consumption on cathode is not high enough to avoid liquid water condensing and blocking the anode catalyst. With lower voltage comes greater heat loss which may help removal of water. Additionally, the water balance across the membrane may be slower to equilibrate than the reaction rate, after a second it balances out and water pathways are established. The observation of a knee can support conclusion 'ii' above as that knee becomes more distinct for higher concentrations of hydrogen but is rather distinct for all oxygen concentrations. However, from this data alone it is not certain water on anode is limiting performance.

3.2.2.5 Steady-state reactant sensitivity

As we already discussed in Chapter 2, limiting current method is a well established tool to measure the total oxygen transport resistance, $R_{O_2}^{Total}$ (in s/cm), in different components of a PEMFC [97–106]. We employed the similar techniques for measuring both oxygen and hydrogen transport resistances in an operating AEMFC.

The $R_{O_2}^{Total}$ can be obtained by combining the Fick's law of diffusion and Faraday's law together as following:

$$n''_{O_2} = \frac{i}{4F} = \frac{C_{O_2}^{Channel} - C_{O_2}^{Electrode}}{R_{O_2}^{Total}} \tag{3.1}$$

where n''_{O_2} is the oxygen flux in mol/cm^{2}sec, i is the current density in A/cm^2, F is the Faraday's current in Coulomb, C_{O_2} is the oxygen concentration in mol/cm^3. $C_{O_2}^{Electrode}$ (s/cm) tends to zero at limiting current condition and following expression is obtained:

$$n''_{O_2} = \frac{i_{lim}}{4F} = \frac{C_{O_2}^{Channel}}{R_{O_2}^{total}} \tag{3.2}$$

where i_{lim} is the limiting current density. The oxygen concentration at the channel inlet, $C_{O_2}^{Channel}$, is calculated from the values of cell operating pressure (P_T), and the dry mole fractions of oxygen (x_{O_2}). The following expression is used to determine the total oxygen transport resistance in a PEMFC and it can also be employed in an AEMFC:

$$R_{O_2}^{Total} = \frac{4F}{RT} * \frac{x_{\text{O}_2}}{i_{lim}}(P_T - P_W) \tag{3.3}$$

where R is the universal gas constant in J/molK, T is the cell temperature in K, P_W is the partial pressure of water vapor.

Similarly, the following expression can be used to determine the total hydrogen transport resistance in the AEMFC:

$$R_{H_2}^{Total} = \frac{2F}{RT} * \frac{x_{\text{H}_2}}{i_{lim}}(P_T - P_W) \tag{3.4}$$

where $R_{H_2}^{Total}$ (in s/cm) is the total hydrogen transport resistance and (x_{H_2}) is the dry mole fractions of hydrogen.

Results from steady-state reactant sensitivity experiments

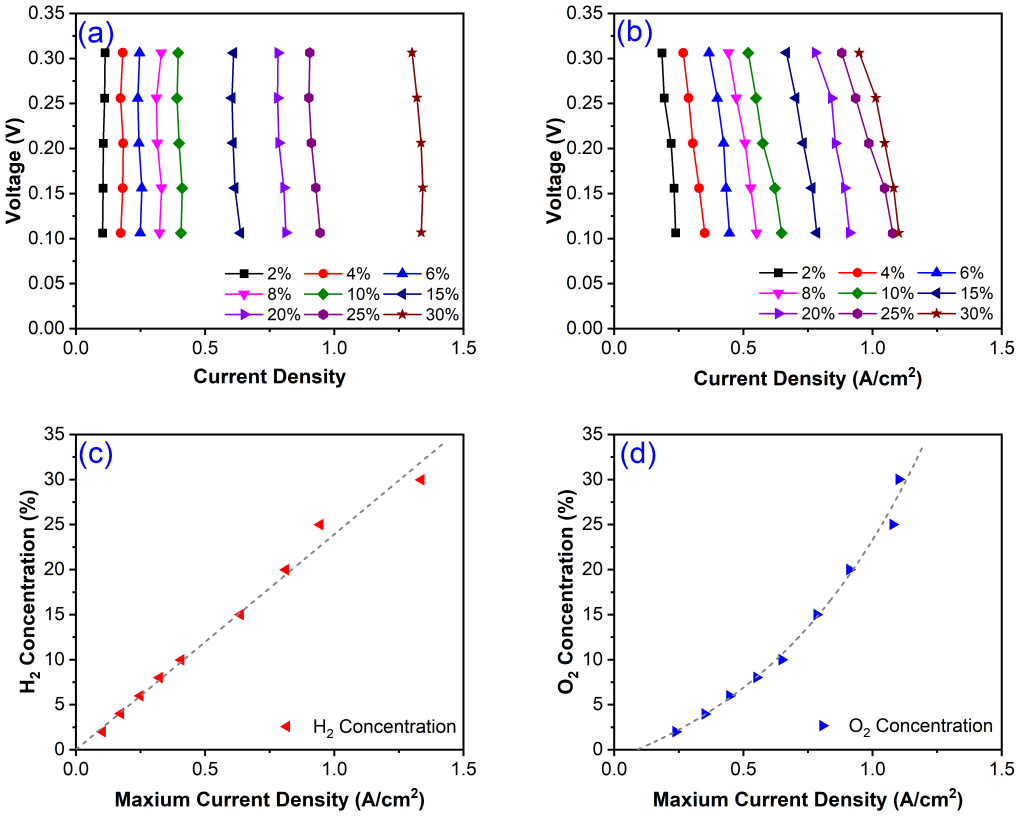

Figure 3.11: Steady-state cell performance using straight parallel flow field to analyze reactant sensitivity for (a) hydrogen and (b) oxygen; total (c) hydrogen and (d) oxygen transport resistance. Cell operating conditions: 70°C, 80% RH, 131 kPaa., 0.80/0.40 NLPM $(H_2+N_2)/O_2$ for hydrogen sensitivity, 0.40/0.60 NLPM $H_2+(N_2/O_2)$ for oxygen sensitivity.

Hydrogen and oxygen reactant sensitivities under steady-state was studied by holding each cell potential for 2 mins. The reactant concentrations were changed parametrically from 2% to 30% for both hydrogen and oxygen. The results are plotted in Figure 3.11. For hydrogen sensitivity, as shown in Figure 3.11(a, c), the hydrogen transport resistance on the anode remains a relatively constant at ca. 1.7 s/cm across all hydrogen concentrations, i.e., the presence of water is not hindering the transport here. In contrast for oxygen sensitivity, as shown in Figure 3.11(b, d), the oxygen transport resistance is increasing steadily, whereas initially transport is less than that at anode for the same current density and then increasing to roughly

4 s/cm. Water then is clearly hindering performance on cathode contrary to the initial assumption.

3.3 Neutron radiography results

3.3.0.1 RH sensitivity

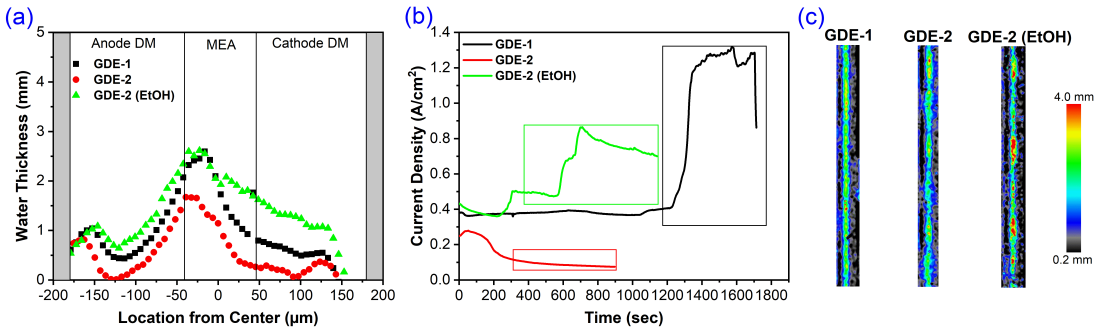

Figure 3.12: (a) Through-plane water thickness for three cell configurations at 0.30 V, 70°C, 90% RH and 135 kPaa., (b) transient current density with boxes marking the data used for averaging neutron images, (c) false colored neutron images showing water thickness, anode is on the left and cathode on the right.

Cell performance and neutron radiography data is shown in Figure 3.12. The test time is varied between each cell configuration due to limited beam time and based on the observation in previous lab experiments that a cell could be considered unrecoverable if upon reducing RH the current density declined to a steady value below 0.10 A/cm^2. To make best use of limited beam time some steps were cut short. These three cells are examined together at the 90% RH condition which was the final step for GDE-2. As shown in Figure 3.12(b), GDE-1 shows best performance towards the end of the test step. The large change in current density seen in the transient data suggests water retention and removal is the issue. Clearly a change in electrode design is required to address this. From Figure 3.12(a), water thickness is largest on the anode near the catalyst layer and so changes in design to address flooding should be aimed here. GDE-2, as with tests performed at the home laboratory, showed considerably weak performance. It was observed during ion exchange that GDE-2 appeared to be extremely hydrophobic, and it was hypothesized that adding a wetting agent to the ion exchange solution would improve the exchange process. Hence, 10 mL ethanol was poured into 90 mL of 2M KOH solution. GDE-2 (ethanol) showed vastly improved performance. From figure 3.12(a), it is observed that water on the anode is nearly the same for all three cells. The difference is apparent on the cathode where GDE-2 (ethanol) has the greatest thickness of water. The weak

performance previously observed was due to weak counter ion exchange, low water uptake, as noted previously, and low conductivity of the Cl^- form of the ionomer [54]. Better exchange allowed for much greater water uptake and increased performance.

3.3.0.2 H_2 sensitivity

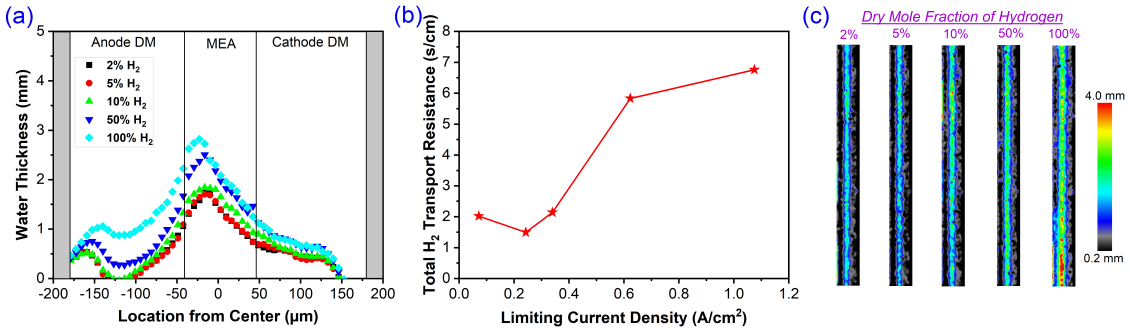

Figure 3.13: (a) Through-plane water thickness for hydrogen sensitivity at 0.30 V, 70°C, 90% RH, and 135 kPaa., (b) total hydrogen transport resistance, (c) false colored neutron images showing water thickness, anode is on the left and cathode on the right.

The results for steady-state hydrogen sensitivity experiments performed in tandem with neutron imaging is shown in Figure 3.13. Slightly different from the previous reactant sensitivity results, this test is performed at a higher relative humidity and across a greater range of reactant concentrations. This is done to ensure water was present, with trends that could be extrapolated to other test conditions. For 2%, 5%, and 10% hydrogen concentrations, the results in figure 3.13(b) match relatively well with results shown in Figure 3.11(c). At higher hydrogen concentrations (e.g., 50%, 100%), significant water accumulation beneath the anode land is observed. The average water thickness at the anode electrode doubles from 1 to 2 mm. Water can be clearly seen to build up on the anode from the false colored image, as shown in Figure 3.13(c).

3.3.0.3 O_2 sensitivity

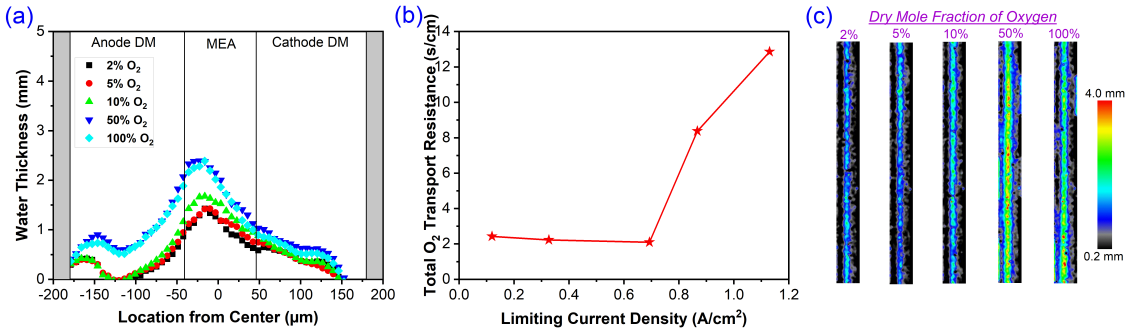

Figure 3.14: (a) Through-plane water thickness for oxygen sensitivity at 0.30 V, 70°C, 90% RH, and 135 kPaa., (b) total oxygen transport resistance, (c) false colored neutron images showing water thickness, anode is on the left and cathode on the right.

The results for steady-state oxygen transport resistance and water content are plotted in Figure 3.14. Slightly deviating from the results collected in the home lab at lower relative humidity as previously shown in Figure 3.11(d), the oxygen transport resistance plotted in Figure 3.14(b), is relatively constant at 2%, 5%, and 10% oxygen concentrations. With more water present in the feed stream the liquid was able to be developed at lower current density. Similar to the results observed for hydrogen limiting current the transport apparently increases drastically for 50% and 100% concentration. However, this does not correlate with the water present at the cathode electrode which only trends up slightly, from 1.7 to 2.2 mm, in comparison to the water on the anode electrode which again doubles.

These results paint a more complete picture for water transport. At low current densities, here reactant concentrations beneath 50%, water generated will first transport to the cathode as there is a slight concentration gradient created by the production at anode and consumption at the cathode. As the water generation is increased it accumulates within the cathode electrode and diffusion media. The water transport resistance through the membrane and the cathode to the channel increases, although there is a larger anode-cathode water gradient at the higher reactant concentrations the rate of removal cannot is not sufficient and anode floods. For both Figure 3.13(a) and 3.14(a), one can observe peak water thickness shifts from nearly the middle of the membrane towards the anode electrode.

What this means for steady-state reactant sensitivity testing is that when current density is low and relatively little liquid water is present, oxygen transport is the limiting factor and can be measured. As water begins to build the limiting factor becomes hydrogen transport through a now flooded anode.

3.4 Summary

In this work, sensitivity of the AEMFC performance is investigated under different operating conditions (e.g., relative humidity, reactant sensitivity) under both dynamic and steady state conditions. The study was done using two types of flow fields (single channel serpentine and straight parallel) and two types of gas diffusion electrodes (powder and dispersion ionomer type). First, it is discovered that the cell performance is sensitive to membrane and GDE's ion exchange and cell assembling processes; GDE prepared with dispersion type of ionomer contained more fluorine which resulted in poor ion exchange and thereby poor cell performance. Second, it was found that the cell performance is very sensitive to channel design; serpentine design offers better performance due to active water removal from the cell as compared to the straight parallel design. Third, different RH conditions have clear effect on cell performance and cell water behavior; higher RH improves better ohmic performance by offering increased membrane and ionomer conductivity, whereas lower RH is better for achieving high concentration performance through active water management in the cell. Fourth, low concentrations of hydrogen and oxygen sensitivity experiments showed that performance is more sensitive when reducing the hydrogen on the anode side. Finally, neutron experiments show that cathode gets more water at the beginning of the cell operation, out of which most water is then transported to the anode through electroosmotic drag, the balance shifts towards anode and anode becomes flooded at some point which causes the cell performance to reduce.

Note

Certain trade names and company products are mentioned in the text or identified in an illustration in order to adequately specify the experimental procedure and equipment used. In no case does such identification imply recommendation or endorsement by the National Institute of Standards and Technology (NIST), nor does it imply that the products are necessarily the best available for the purpose.

Acknowledgement

This work was sponsored by the University of California, Merced. It was partially supported by NIST and NREL. The AEMFC materials are prepared and provided by Dr. Ami Neyerlin from the National Renewable Energy Laboratory (NREL, Golden, CO 80401). I would like to thank Marc F. Labata, Shirin Mehrazi, and Nitul Kakati for taking the SEM/EDS images for the GDE materials. Thanks to Joy Marie Mora for her ongoing efforts to model some of the results shown in this project to deepen the fundamental understanding of AEMFC.

Chapter 4

EXPERIMENTAL INVESTIGATION ON THE EFFECT OF MEMBRANE THICKNESS AND CELL OPERATING CONDITIONS ON LIMITING CURRENT ANALYSIS IN PEMFC

Hydrogen-powered a proton exchange membrane fuel cells (PEMFC) have great potential to replace traditional internal combustion engines due to their inherent advantages of zero greenhouse gas emissions, better fuel efficiency, quick startup, silent operation, less required maintenance, etc. In a PEMFC, oxygen transport is a critical performance limiting factor because of the sluggish oxygen reduction reaction kinetics. Limiting current method is a well-established in-situ diagnostic tool to measure the oxygen transport resistance in a PEMFC. To obtain accurate oxygen transport resistances, a few key assumptions need to be made including (1) the effect of temperature gradient in the diffusion media is negligible, (2) no convective flow in the porous media, (3) oxygen is diluted in a gas mixture of nitrogen and water vapor, (4) the total oxygen transport resistance combines gas diffusion layer, microporous layer, and catalyst layer, (5) the effect of membrane thickness has negligible effect, and (6) the anode side does not affect the measurement results due to fast hydrogen oxidation reaction. In this study, we perform a systematic study of the effect of membrane thickness and operating conditions on obtaining robust and reliable limiting current measurements. Standard Nafion membranes of two different thicknesses (25 and 85 µm) are tested with Toray 060 and Freudenberg H23C8 diffusion media. In addition, we further study the interaction between membrane thickness and cell temperature, asymmetric pressure and relative humidity and their effects on limiting current results. Our results show that membrane thickness and relative humidity are critical factors in obtaining reliable oxygen transport resistance due to their effect on the overall water balance in the cell.

4.1 Experimental details

4.1.1 Cell components

Flow fields utilizing a straight parallel channel design were implemented [24]. The channels measure 660 µm in width and 800 µm in depth, maintaining a 1:1

channel-to-land ratio. The flow field's total active area, originally 4 cm^2, was reduced to 2 cm^2 by using polytetrafluoroethylene (PTFE) gasket sheets. This ensured differential flow conditions within the cell, confirming uniform temperature, relative humidity (RH), and flow conditions at both the channel inlet and outlet [99]. Such uniformity is critical for minimizing pressure drop along the channel, a necessary condition for attaining a concentration-driven limiting current. Additionally, the PTFE gaskets effectively prevented any gas leakage. Catalyst coated Nafion membrane electrode assembly (MEA) were sourced from Ion Power, USA. Membranes of two varying thicknesses - 25 and 90 µm - were utilized. All MEAs were fabricated using carbon-supported platinum catalysts, with a loading of 0.30 mg_{Pt}/cm^2. The electrochemically active surface area (ECSA) for each MEA was determined to be approximately 35∼40 m_2/gm_{Pt}, measured via hydrogen adsorption/desorption (HAD) methods using cyclic voltammetry (CV). This study employed two types of commercial gas diffusion media (GDM), both wetproofed and MPL-coated: Toray 060 and Freudenberg H23C8. Further details on the flow channel design and the gas diffusion media (GDMs) utilized are available in our prior publications [30, 130].

4.1.2 Fuel cell experiments

A fully automated Greenlight G20 fuel cell test station was used to conduct the fuel cell experiments [131], while a Gamry Reference 3000 Potentiostat, coupled with a Gamry 30k Booster, facilitated electrochemical impedance spectroscopy (EIS) for measuring cell resistance [132]. High frequency resistance (HFR), as measured through EIS, indicates the ohmic losses within the fuel cell, incorporating both electronic and ionic resistances [133].

Ultra-high purity air, hydrogen, and nitrogen gases were used. The experimental procedure commenced with cyclic voltammetry (CV) to measure the electrochemically active surface area (ECSA) [134], followed by a 16-cycle break-in procedure employed to hydrate the membrane and develop proton-conducting pathways within it. Once the cell was successfully broken in, a series of testing protocols were executed to evaluate various oxygen transport properties through limiting current experiments and to assess performance via polarization experiments. All test protocols are detailed in Table 4.1.

Test	Temp. (°C)	Inlet RH (%)	Pressure (kPa abs.)	Reactants (An/Ca)	Flow rate (NLPM)	Comments
CV	30	100	100	H_2/N_2	0.02/0.04	To measure ECSA
Break-in	70	100	150	H_2/Air	λ=10	To activate the cell
DLC	80	64	100 ∼300	H_2/(Air+N_2)	0.40/2.0	To study effect
WLC	70	80, 100	300	H_2/(Air+N_2)	0.40/2.0	of membrane thickness
DLC	60, 70, 80	64	100 ∼300	H_2/(Air+N_2)	0.40/2.0	To study effect
WLC	70	100	300	H_2/(Air+N_2)	0.40/2.0	of cell temperature
DLC	80	64	250/300 ∼ 300/250	H_2/(Air+N_2)	0.40/2.0	To study effect
WLC	70	100	300	H_2/(Air+N_2)	0.40/2.0	of cell pressure
DLC	80	50, 64, 80, 95	100 ∼300	H_2/(Air+N_2)	0.40/2.0	To study effect
WLC	70	100	300	H_2/(Air+N_2)	0.40/2.0	of cell RH
Dry i-V	70	60	100	H_2/Air	0.40/2.0	To evaluate cell
Wet i-V	70	100	300	H_2/Air	0.40/2.0	performance for all

Table 4.1: Test protocols for the PEM fuel cell experiments. DLC and WLC stand for dry limiting current and wet limiting current experiments, respectively.

Limiting current experiments were conducted under standard dry (80°C, 64% RH, and 100∼300 kPa) and wet (70°C, 80∼100% RH, and 300 kPa) conditions across all samples to examine the impact of membrane thickness using both types of gas diffusion media (GDM). For these measurements, the cell operated at each voltage for 2 minutes, with data from the last 20 seconds being averaged. The oxygen concentration was varied between 1∼4% for dry limiting current experiments to prevent water condensation within the cell and varied from 1∼21% for wet limiting current experiments to induce liquid water condensation.

Additionally, a GDM compression study using Freudenberg H23C8 GDM was performed to determine whether the limiting current results were influenced by the thicker membrane compressing the GDM more than anticipated. Finally, we tested different conditions to see how cell temperature, pressure, and humidity affect the measurements of the limiting current.

For all cells, steady-state fuel cell performances were evaluated under both dry (70°C, 60% RH, and 100 kPa) and wet (70°C, 100% RH, and 300 kPa) conditions. Performance curves were obtained in a steady-state potentiostatic mode by maintaining the cell voltage at each point for 13 minutes, with the final minute's data being averaged. Except for CV, anode and cathode flow rates were set at 400 and 2000 sccm, respectively. All pressures mentioned in this study are reported in absolute values, calculated by adding atmospheric pressure to the gauge pressure.

All of the PEM fuel cell test protocls are tabulated in Table 4.1. Necessary break-in or activation process were carried out to activate the catalyst layer and hydrate the membrane before running any experiments. During the activation process, each cell was conditioned by stepping the voltage with high stoichiometries

(λ=10) of H_2/Air at 70°C, 150 kPa, and 100% RH in the following sequence: 0.60 V for 15 min, 0.85 V for 15 min, this was repeated 6∼8 times or until current density reached a plateau.

Fuel cell performance data were collected under both dry (70°C, 64% RH, 100 kPa) and wet (70°C, 100% RH, 300 kPa) conditions using potentiostatic control. Each voltage set point was held for ten minutes to achieve steady state conditions, then cell performance data over one minute was taken and averaged.Limiting current experiments were conducted under both dry (80°C, 64% RH) and wet (70°C, 100% RH) conditions to study the oxygen transport properties following the standard limiting current test protocols. Dry limiting current tests were done at four cell pressures: 110, 150, 200, and 300 kPa abs., and four dry mole fractions of oxygen: 1, 2, 3, and 4%. Wet limiting current tests were carried out at a single pressure of 300 kPa abs. and under twelve dry mole fractions of oxygen: 1-8% with stepped increase of 1%, followed by 10% 12%, 16% and 21%. At each oxygen concentration, cell voltage was controlled to 0.30, 0.24, 0.18, 0.12, 0.09 V with a hold time of 2 min at each potential.

4.1.3 Limiting current theory

Assumptions

1. Temperature is constant i.e. ignore the impact of temperature change in the diffusion media under different current densities.

2. No convective flow in the porous media.

3. Oxygen is diluted in a gas mixture of nitrogen and water vapor.

4. This analysis combines GDL and MPL for the Fickian diffusion. So, the D/D_{eff} ratio represents a combined result.

5. D/D_{eff} (or, τ/ϵ) value (calculated under dry condition) is totally a DM material property.

6. The membrane or membrane thickness has no effect in the limiting current analysis.

7. Anode side has no effect on the oxygen transport properties, cathode being the dominant in limiting current analysis.

8. There is no effect of anode RH or anode backpressure.

Calculation of total OTR

We know, each mole of oxygen generates 4 moles of electron in a PEMFC. Hence, oxygen diffusion flux, n''_{O_2} (in mol/cm^2 sec), can be expressed as:

$$n''_{O_2} = \frac{i}{4F} \tag{4.1}$$

Mass transfer coefficient, k (in cm/sec), is a diffusion rate constant that relates the mass transfer rate, n (in mol/sec), mass transfer area, A (in cm^2), and concentration gradient, ΔC (in mol/cm^3) in following way:

$$k = \frac{n}{A * \Delta C}$$

$$\Rightarrow k = n'' \frac{1}{\Delta C}$$

$[\because n" = Diffusion flux = \frac{n}{A}]$

$$\Rightarrow n'' = k * \Delta C$$

$$\Rightarrow n'' = \frac{\Delta C}{R_{MT}}$$

[$\because$ Mass transfer coefficient, k, is the inverse of mass transport resistance, R_{MT}]

$$\Rightarrow n''_{O_2} = \frac{C_{O_2}^{Channel} - C_{O_2}^{Electrode}}{R_{O_2}^{Total}} \tag{4.2}$$

Total cell oxygen transport resistance, R_{MT} or $R_{O_2}^{Total}$, can be defined from equation-4.2 as the difference in oxygen concentrations between the flow field inlet and the electrode divided by the average oxygen flux to the electrode.

$R_{O_2}^{Total}$ can be calculated by combining the Fick's law of diffusion and Faraday's law. Hence, equations 4.1 and 4.2 are combined as following:

$$n''_{O_2} = \frac{i}{4F} = \frac{C_{O_2}^{Channel} - C_{O_2}^{Electrode}}{R_{O_2}^{Total}}$$

where i is the current density in A/cm^2, F is the Faraday's constant in Coulomb, C_{O_2} is the oxygen concentration in mol/cm^3. $C_{O_2}^{Electrode}$ tends to zero at limiting current condition and we get:

$$n''_{O_2} = \frac{i_{lim}}{4F} = \frac{C_{O_2}^{Channel}}{R_{O_2}^{total}}$$

$$\Rightarrow \frac{i_{lim}}{4F} = C_{O_2}^{Channel} * \frac{1}{R_{O_2}^{Total}}$$

$$\frac{i_{lim}}{4F} = \frac{P_{O_2}^{Channel}}{RT} * \frac{1}{R_{O_2}^{Total}} \tag{4.3}$$

$[\because P = C \times R \times T]$

where i_{lim} is the limiting current density in A/cm^2, $P_{O_2}^{Channel}$ is the oxygen pressure at the channel inlet in kPa, R is the universal gas constant in J/molK, T is the cell temperature in K. $P_{O_2}^{Channel}$ is calculated from the cell operating pressure, P_T, partial pressure of water vapor, P_W, and the dry mole fractions of oxygen, x_{O_2}.

$$\frac{i_{\lim}}{4F} = \frac{(P_T - P_W) \times x_{O_2}}{RT} * \frac{1}{R_{O_2}^{Total}}$$

$$\Rightarrow R_{O_2}^{Total} = \frac{4F}{RT} * \frac{x_{\mathrm{O_2}}}{i_{lim}}(P_T - P_W)$$

And, the P_W is calculated from inlet relative humidity, RH, and saturation pressure, P_S:

$$R_{O_2}^{Total} = \frac{4F}{RT} * \frac{x_{\mathrm{O_2}}}{i_{lim}}(P_T - RH * P_S) \tag{4.4}$$

Also, it is desirable to break down the total transport resistance in several different components to understand easily:

$$R_{O_2}^{Total} = R_{O_2}^{Channel} + R_{O_2}^{GDL} + R_{O_2}^{MPL} + R_{O_2}^{Electrode} \tag{4.5}$$

Calculation of OTR in channel

Convective mass transfer coefficient, h_m can be expressed as:

$$h_m = Sh * \frac{D_{i,j}}{D_h}$$

$$\therefore h_{m,H_2} = Sh * \frac{D_{H_2,mix}}{D_h}$$

$$\therefore h_{m,O_2} = Sh * \frac{D_{O_2,mix}}{D_h}$$

where D_h is the hydraulic diameter, and D_{ij} is the binary diffusion coefficient for species i and j. And, D_{ij} can be expressed as:

$$D_{i,j} = \frac{\left(1.013{*}10^{-3}\right){*}T^{1.75}}{P_T\left(V_i^{\frac{1}{3}} + V_j^{\frac{1}{3}}\right)^2}\left[\frac{1}{M_i} + \frac{1}{M_j}\right]^{\frac{1}{2}}$$

$$\Rightarrow D_{i,j} = \frac{T^{1.75}}{P_T} * C$$

$$\left[\text{Let, } C = \frac{(1.013{*}10^{-3})}{\left(V_i^{\frac{1}{3}} + V_j^{\frac{1}{3}}\right)^2}\left[\frac{1}{M_i} + \frac{1}{M_j}\right]^{\frac{1}{2}}\right]$$

$$\therefore D_{O_2,N_2} = \frac{T^{1.75} * C_1}{P_T}$$

$$\therefore D_{O_2,H_2O} = \frac{T^{1.75} * C_2}{P_T}$$

For a straight parallel flow field design, some convection happens in the flow channel with diffusion being the major transport mechanism. Channel transport resistance, $R_{O_2}^{Channel}$, is the inverse of mass transfer co-efficient, h_m, which can be calculated using Sherwood number, Sh, fickian diffusion coefficient of oxygen, and channel geometry [17].

$$R_{O_2}^{Channel} = \frac{1}{h_{m,O_2}}$$

$$\Rightarrow R_{O_2}^{Channel} = \frac{D_h}{Sh * D_{O_2,mix}} \tag{4.6}$$

Sherwood number can be calculated from channel aspect ratio [17]. And, Blanc's law is used for the calculation of the effective diffusion coefficient of oxygen ($D_{O_2,mix}$):

$$D_{im} = \left(\sum_{\substack{j=1 \\ j \neq i}}^{n} \frac{x_j}{D_{ij}}\right)^{-1}$$

$$\Rightarrow D_{O_2,mix} = \left(\frac{x_{N_2}}{D_{O_2,N_2}} + \frac{x_{H_2O}}{D_{O_2,H_2O}}\right)^{-1}$$

$$\Rightarrow \frac{1}{\mathrm{D_{O_2,mix}}} = \left(\frac{\mathrm{x_{N_2}}}{\mathrm{D_{O_2,N_2}}} + \frac{\mathrm{x_{H_2O}}}{\mathrm{D_{O_2,H_2O}}}\right)$$

$$\Rightarrow \frac{1}{\mathrm{D_{O_2,mix}}} = \left(\frac{1-\mathrm{x_{H_2O}}}{\mathrm{D_{O_2,N_2}}} + \frac{\mathrm{x_{H_2O}}}{\mathrm{D_{O_2,H_2O}}}\right) \text{ [From Assumption} - 3]$$

$$\Rightarrow \frac{1}{\mathrm{D_{O_2,mix}}} = (1-\mathrm{x_{H_2O}})*\frac{\mathrm{P_T}}{\mathrm{T^{1.75}*C_1}} + \mathrm{x_{H_2O}}*\frac{\mathrm{P_T}}{\mathrm{T^{1.75}*C_2}}$$

$$\Rightarrow \frac{1}{\mathrm{D_{O_2,mix}}} = \frac{\mathrm{P_T} - \mathrm{P_T.x_{H_2O}}}{\mathrm{T^{1.75}*C_1}} + \frac{\mathrm{P_T.x_{H_2O}}}{\mathrm{T^{1.75}*C_2}}$$

$$\Rightarrow \frac{1}{\mathrm{D_{O_2,mix}}} = \frac{\mathrm{P_T} - \mathrm{P_{H_2O}}}{\mathrm{T^{1.75}*C_1}} + \frac{\mathrm{P_{H_2O}}}{\mathrm{T^{1.75}*C_2}} \quad \left[\because \mathrm{x_{H_2O}} = \frac{\mathrm{P_{H_2O}}}{\mathrm{P_T}}\right] \tag{4.7}$$

$$\Rightarrow \frac{1}{\mathrm{D_{O_2,mix}}} = \frac{\mathrm{P_T} - \mathrm{P_{H_2O}}}{\mathrm{P_T}*\mathrm{D_{O_2,N_2}}} + \frac{\mathrm{P_{H_2O}}}{\mathrm{P_T}*\mathrm{D_{O_2,H_2O}}} \tag{4.8}$$

$$\therefore \textit{Equation (4.6)} \Rightarrow \mathrm{R_{O_2}^{Channel}} = \frac{\mathrm{D_h}}{\mathrm{Sh}} * \left[\frac{\mathrm{P_T} - \mathrm{P_{H_2O}}}{\mathrm{T^{1.75}*C_1}} + \frac{\mathrm{P_{H_2O}}}{\mathrm{T^{1.75}*C_2}}\right]$$

Pressure dependent and independent OTR

As mentioned earlier, $R_{O_2}^{total}$ can be broken into contributions from channel ($R_{O_2}^{Channel}$), GDL ($R_{O_2}^{GDL}$), MPL ($R_{O_2}^{MPL}$), and CL ($R_{O_2}^{Electrode}$) as following:

$$R_{O_2}^{Total} = R_{O_2}^{Channel} + R_{O_2}^{GDL} + R_{O_2}^{MPL} + R_{O_2}^{Electrode}$$

Intermolecular gas diffusion occurs in the large pores of the GDL, whereas Knudsen diffusion occurs in the small pores of MPL and catalyst layer. Oxygen also gets diffused through liquid water and ionomer. Intermolecular/ Fickian/ binary gas diffusion is dependent on pressure. Knudsen diffusion or diffusion through liquid water, ionomer, and the nanometer scale pores of the catalyst layer and MPL are independent of pressure. Hence, cell operating pressure is varied to split the total transport resistance into pressure dependent ($R_{O_2}^{Fick}$) and pressure independent ($R_{O_2}^{Other}$) parts. The separation of the the total resistance into pressure dependent and independent parts can be derived from equation 4.5 as:

$$R_{O_2}^{Total} = R_{O_2}^{Channel} + R_{O_2}^{GDL} + R_{O_2}^{MPL} + R_{O_2}^{Electrode}$$

$$\Rightarrow R_{O_2}^{Total} = R_{O_2}^{Channel} + [R_{O_2}^{Fick}]_{Pressure\ dependent\ term} + [R_{O_2}^{Other}]_{Pressure\ independent\ term}$$

$$\Rightarrow R_{O_2}^{Total} = R_{O_2}^{Channel} + R_{O_2}^{Fick} + R_{O_2}^{Others}$$

$$\Rightarrow (R_{O_2}^{Total} - R_{O_2}^{Channel}) = R_{O_2}^{Fick} + R_{O_2}^{Others} \tag{4.9}$$

Now, equation 4.3 can be re-written for Fickian diffusion in the DM as:

$$\frac{i_{lim}}{4F} = \frac{P_{O_2}^{DM}}{RT} * \frac{1}{R_{O_2}^{Fick}}$$

$$\Rightarrow \frac{i_{lim}}{4F} = \frac{P_{O_2}^{DM}}{RT} * \frac{1}{R_{O_2}^{Fick}} = D_{O_2}^{eff} * \frac{P_{O_2}^{DM}}{RT} * \frac{1}{dx}$$

[$\because \frac{\mathrm{i_{lim}}}{\mathrm{4F}} = \mathrm{D_{O_2}^{eff}} * \frac{\mathrm{P_{O_2}^{DM}}}{\mathrm{RT}} * \frac{1}{\mathrm{dx}}$ for limiting current condition at DM]

$$\Rightarrow R_{O_2}^{Fick} = \frac{dx}{D_{O_2}^{eff}}$$

$$\Rightarrow R_{O_2}^{Fick} = \frac{f * dx}{D_{O_2}^{eff}}$$

$$\Rightarrow R_{O_2}^{Fick} = \frac{f * h}{D_{O_2}^{eff}}$$

where h or dx is the compressed diffusion media thickness, f is the geometric factor or dimensionless shape factor which is calculated using reference [97].

$$\Rightarrow R_{O_2}^{Fick} = \frac{f * h}{D_{O_2,mix} * (\frac{\varepsilon}{\tau})}$$

$$\Rightarrow R_{O_2}^{Fick} = f * h * (\frac{\tau}{\varepsilon}) * \frac{1}{D_{O_2,mix}}$$

$$\Rightarrow \mathrm{R_{O_2}^{Fick}} = \mathrm{f{*}h{*}} \left(\frac{\tau}{\varepsilon}\right) * \left[\frac{\mathrm{P_T} - \mathrm{P_{H_2O}}}{\mathrm{P_T{*}D_{O_2,N_2}}} + \frac{\mathrm{P_{H_2O}}}{\mathrm{P_T{*}D_{O_2,H_2O}}}\right]$$

[By inserting values from equation 4.8]

Then, equation 4.9 can be written as:

$$(\mathrm{R}_{\mathrm{O_2}}^{\mathrm{Total}} - \mathrm{R}_{\mathrm{O_2}}^{\mathrm{Channel}}) = \mathrm{f{*}h{*}}\left(\frac{\tau}{\varepsilon}\right) * \left[\frac{\mathrm{P_T} - \mathrm{P_{H_2O}}}{\mathrm{P_T{*}D_{O_2,N_2}}} + \frac{\mathrm{P_{H_2O}}}{\mathrm{P_T{*}D_{O_2,H_2O}}}\right] + \mathrm{R}_{\mathrm{O_2}}^{\mathrm{Others}}$$

$$\Rightarrow (\mathrm{R}_{\mathrm{O_2}}^{\mathrm{Total}} - \mathrm{R}_{\mathrm{O_2}}^{\mathrm{Channel}}) = \mathrm{fh}\left(\frac{\tau}{\varepsilon}\right) * \frac{\mathrm{P_T}}{\mathrm{P_T{*}D_{O_2,N_2}}} - \mathrm{fh}\left(\frac{\tau}{\varepsilon}\right) * \frac{\mathrm{P_{H_2O}}}{\mathrm{P_T{*}D_{O_2,N_2}}} + \mathrm{fh}\left(\frac{\tau}{\varepsilon}\right) \frac{\mathrm{P_{H_2O}}}{\mathrm{P_T{*}D_{O_2,H_2O}}} + \mathrm{R}_{\mathrm{O_2}}^{\mathrm{Others}}$$

$$\Rightarrow (\mathrm{R}_{\mathrm{O_2}}^{\mathrm{Total}} - \mathrm{R}_{\mathrm{O_2}}^{\mathrm{Channel}}) = \mathrm{P_T{*}}\left[\frac{\left(\frac{\tau}{\varepsilon}\right)\mathrm{fh}}{\mathrm{P_T{*}D_{O_2,N_2}}}\right] + \left[\mathrm{P_{H_2O}}\left\{-\frac{\left(\frac{\tau}{\varepsilon}\right)\mathrm{fh}}{\mathrm{P_T{*}D_{O_2,N_2}}} + \frac{\left(\frac{\tau}{\varepsilon}\right)\mathrm{fh}}{\mathrm{P_T{*}D_{O_2,H_2O}}}\right\}\right] + \mathrm{R}_{\mathrm{O_2}}^{\mathrm{Others}}$$

$$\Rightarrow (\mathrm{R}_{\mathrm{O_2}}^{\mathrm{Total}} - \mathrm{R}_{\mathrm{O_2}}^{\mathrm{Channel}}) = \mathrm{P_T{*}}\left[\frac{\left(\frac{\tau}{\varepsilon}\right)\mathrm{fh}}{\mathrm{P_T{*}D_{O_2,N_2}}}\right] + \left[\mathrm{P_W}\left\{\frac{\left(\frac{\tau}{\varepsilon}\right)\mathrm{fh}}{\mathrm{P_T{*}D_{O_2,H_2O}}} - \frac{\left(\frac{\tau}{\varepsilon}\right)\mathrm{fh}}{\mathrm{P_T{*}D_{O_2,N_2}}}\right\} + \mathrm{R}_{\mathrm{O_2}}^{\mathrm{Others}}\right]$$

So, a plot between ($R_{O_2}^{total}$-$R_{O_2}^{Channel}$) versus P_T can be drawn. Afterwards, D/D_{eff} is calculated from the slope of the graph, and the $R_{O_2}^{total}$ is calculated from the intercept.

Calculation of D/D_{eff} from the slope:

$$\mathrm{Slope,\ a} = \frac{\left(\frac{\tau}{\varepsilon}\right)\mathrm{fh}}{\mathrm{P_T{*}D_{O_2,N_2}}}$$

$$\Rightarrow \left(\frac{\tau}{\epsilon}\right) = \frac{\mathrm{a{*}P_T{*}D_{O_2,N_2}}}{\mathrm{fh}}$$

$$\therefore \left(\frac{\tau}{\epsilon}\right) = \frac{\mathrm{D}}{\mathrm{D_{eff}}} = \frac{\mathrm{D_{O_2,mix}}}{\mathrm{D_{O_2}^{eff}}} = \frac{\mathrm{a{*}P_T{*}D_{O_2,N_2}}}{\mathrm{fh}} \tag{4.10}$$

Calculation of R_{Others} from the intercept:

$$\mathrm{Intercept,\ b} = \left[\mathrm{P_W}\left\{\frac{\left(\frac{\tau}{\varepsilon}\right)\mathrm{fh}}{\mathrm{P_T{*}D_{O_2,H_2O}}} - \frac{\left(\frac{\tau}{\varepsilon}\right)\mathrm{fh}}{\mathrm{P_T{*}D_{O_2,N_2}}}\right\} + \mathrm{R}_{\mathrm{O_2}}^{\mathrm{Others}}\right]$$

$$\Rightarrow \mathrm{b} = \left[\mathrm{P_W}\left\{\frac{\left(\frac{\tau}{\varepsilon}\right)\mathrm{fh}}{\mathrm{P_T{*}D_{O_2,H_2O}}} - \mathrm{a}\right\} + \mathrm{R}_{\mathrm{O_2}}^{\mathrm{Others}}\right]$$

$$\Rightarrow \mathrm{R}_{\mathrm{O_2}}^{\mathrm{Others}} = \mathrm{b} - \left[\mathrm{P_W}\left\{\frac{\left(\frac{\tau}{\varepsilon}\right)\mathrm{fh}}{\mathrm{P_T{*}D_{O_2,H_2O}}} - \mathrm{a}\right\}\right]$$

$$\Rightarrow R_{O_2}^{Others} = b - b_{Fick} \tag{4.11}$$

$$\left[\text{Let, } b_{Fick} = \text{Fician intercept} = P_W \left\{ \frac{\left(\frac{\tau}{\varepsilon}\right) fh}{P_T{}^* D_{O_2,H_2O}} - a \right\} \right]$$

4.2 Experimental results and discussions

4.2.1 Limiting current analysis for a 25 µm membrane under standard conditions

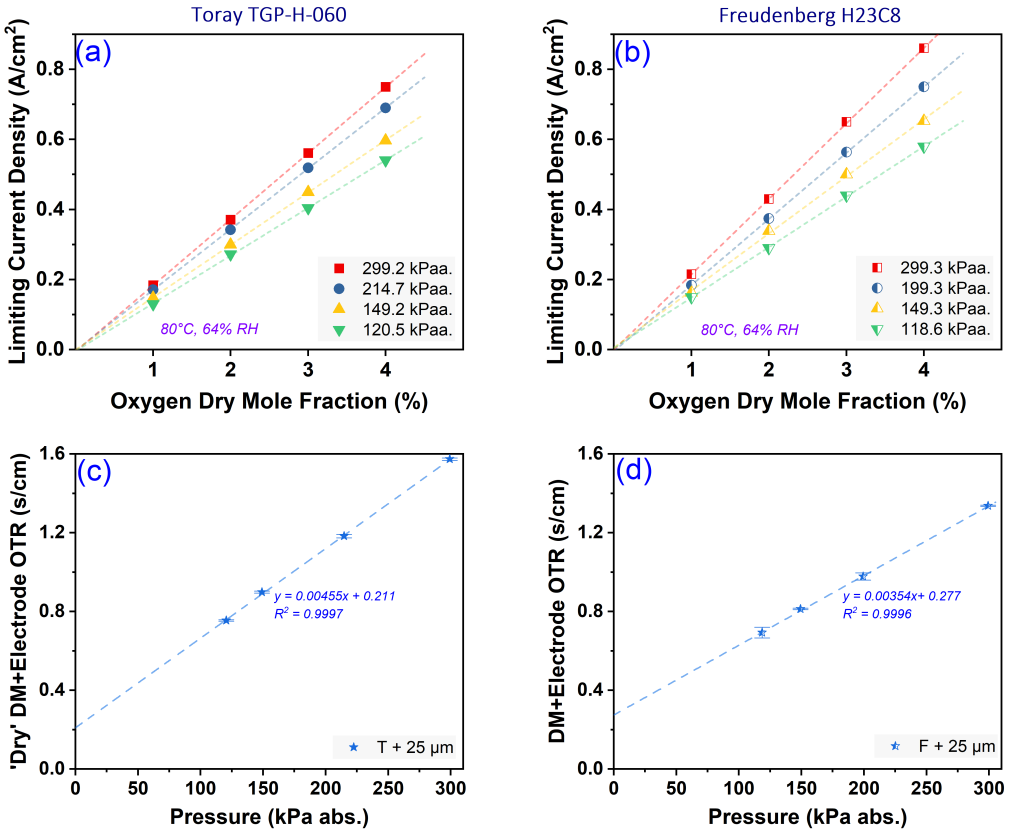

Figure 4.1: Limiting current density as a function of dry mole fraction of oxygen for four different pressures in cells built with (a) Toray and (b) Freudenberg GDMs; the combined oxygen transport resistance across GDM and electrde as a function of cell pressure in cells built with (a) Toray and (b) Freudenberg GDMs, all using 25 µm membrane. Cell operating conditions: 80°C, 64% RH.

First, limiting currents for a 25 µm membrane cell are evaluated by varying the oxygen concentration from 1 to 4% at four different cell pressures under standard dry conditions (80°C, 64% RH) [97, 99] to avoid liquid water condensation within the cell for both Toray and Freudenberg GDMs. The oxygen concentration is adjusted by flowing a diluted mixture of air and nitrogen on the cathode side. The obtained limiting current densities are plotted in Figure 4.1(a,b) for both GDMs as a function of oxygen concentrations. The linear relationship between the limiting current density and the oxygen concentrations, which can be extrapolated back to the origin, indicating a zero current at zero oxygen concentration, demonstrates that the currents measured under all pressures are purely driven by concentration or are transport limited, achieved without the formation of any liquid water in the cell as supported by references [97, 99]. The slopes for these linear lines are proportional to the oxygen transport resistance.

As already mentioned in the theory of limiting current in Section 4.1.3, the channel resistance can be deducted from the overall measured oxygen transport resistances. Subsequently the combined transport resistance across the GDM and electrode layers is plotted as a function of cell pressure, as illustrated in Figure 4.1(c,d) for both types of GDMs. Then the best-fit lines through these four points can be used to distinguish transport resistances that are dependent on pressure, arising from intermolecular gas diffusion in the macro pores of the GDM, and those that are independent of pressure, resulting from diffusion through liquid water or ionomer within the micro pores of the microporous layer (MPL) and catalyst layers. This distinction originates from the fact that intermolecular gas diffusion coefficients are inversely proportional to pressure, whereas diffusion coefficients through liquid water or ionomer, often referred to as Knudsen diffusion, do not depend on pressure. So, the linear relationship between transport resistance and cell pressure for both GDMs, as shown in Figure 4.1(c,d), confirms the expected behavior. Notably, Toray exhibits higher transport resistance compared to Freudenberg, aligning with findings reported in the literature [30].

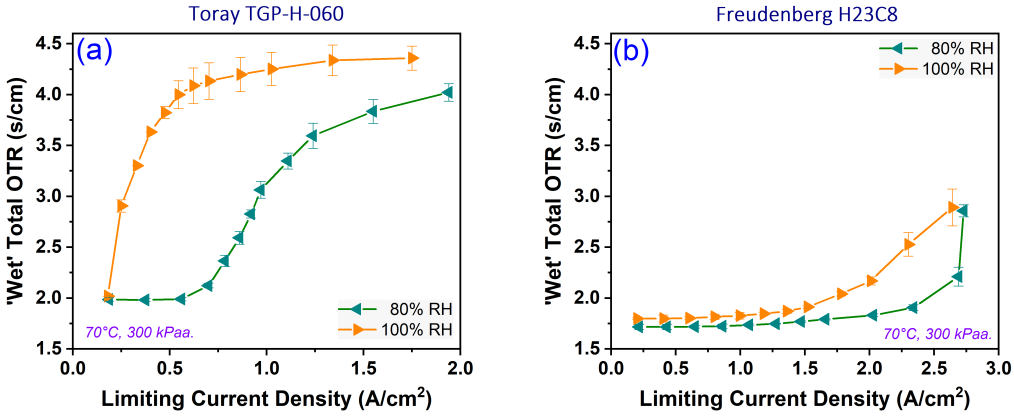

Figure 4.2: Wet oxygen transport resistnace as a function of limiting current density at 80% and 100% RH in cells built with (a) Toray and (b) Freudenberg GDMs, all using 25 µm membrane. Cell operating conditions: 70°C, 300 kPa.

Limiting current experiments are also conducted under standard wet conditions (70°C, 80∼100% RH, 300 kPa) [97, 99] with a wider range of oxygen concentrations, designed to initiate liquid water condensation within the cell, eventually reaching maximum saturation levels. The outcomes of these experiments are presented in Figure 4.2.

As shown in Figure 4.2, the trend observed in cells with 25 µm membrane cell and both types of GDMs align well with the findings reported in the literature [30]. The Toray cell displays 3 distinct regions: a dry plateau, a transition region, and a wet plateau, whereas the Freudenberg cell exhibits two regions: a dry plateau and a transition region), under 80% relative humidity conditions [135]. At 100% RH, there is a noted increase in transport resistance within the cell, likely due to increased liquid water condensation obstructing more pores in the GDM. A shift in oxygen transport resistance from the dry to the wet region is evident for the Toray, transitioning from about 2 s/cm under dry conditions to around 4 s/cm when wet. In contrast, the Freudenberg GDM remains longer in the dry state, with peak resistance reaching approximately 3 s/cm, which is on par with the lower dry transport resistance observed in Figure 4.1(c, d).

4.2.2 Limiting current analysis for 25 and 85 µm membrane under standard conditions

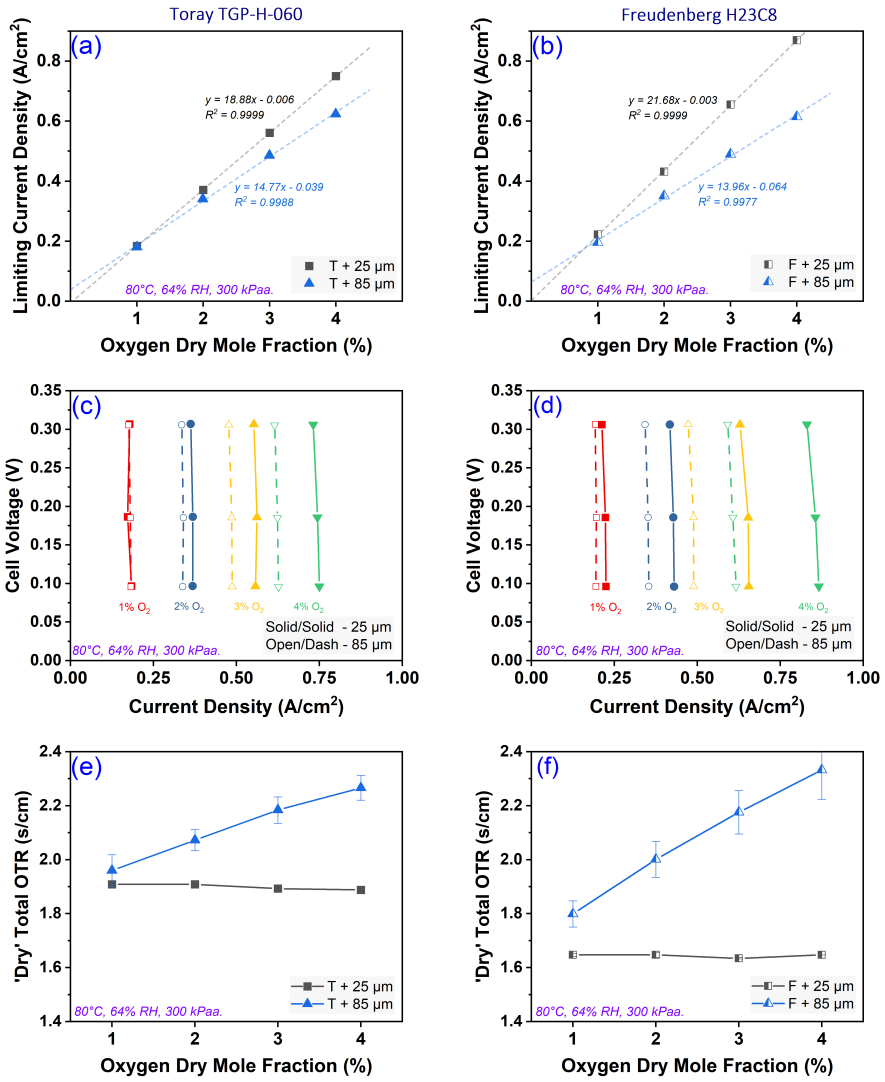

Figure 4.3: . (a,b) Limiting current density as a function of dry mole fraction of oxygen at 300 kPa for 25 µm and 85 µm membranes using Toray and Freudenberg GDMs, respectively; (c,d) voltage versus current density curves showing limiting current density at 300 kPa for both membrane thicknesses; (e,f) dry total oxygen transport resistance as a function of dyr mole fraction of oxygen at 300 kPa for the two membrane thicknesses with each type of GDM. Cell operating conditions: 80°C, 64% RH.

For the next step, it is aimed to conduct limiting current experiments under the same operating conditions using a thicker 85 µm membrane, and then compare the results with those from a 25 µm membrane. As depicted in Figure 4.3(a,b), it is intriguing to note that the trend line from the plot of limiting current density versus oxygen concentration does not reach zero and instead passes slightly above the origin for the thicker 85 µm membrane. To simplify the presentation, data only for a cell pressure of 300 kPa is shown, while data for all cell pressures are available in Figure 4.4. The i-V profiles for both membranes, as illustrated in Figure 4.3(c,d), show that the limiting current density for the cell with the thicker 85 µm membrane is lower than that of the cell with the 25 µm membrane. This difference is particularly pronounced at higher oxygen concentrations, where the trend in current density does not increase linearly with oxygen concentration, suggesting that the observed current is not a true concentration-limited current. Equation 4.4 can be employed to calculate the overall transport resistance from the current density values depicted in Figure 4.3(c,d). Figure 4.3(e,f) presents the overall transport resistance as a function of oxygen concentration for both GDMs. For the 25 µm membrane, the transport resistance appears as a horizontal line, indicating the absence of liquid water condensation within the cell and thus characterizing this resistance as purely dry transport resistance, approximately 1.9 s/cm for Toray and 1.62 s/cm for Freudenberg GDM. Interestingly, with the thicker 85 µm membrane, transport resistance increases with oxygen concentration for both GDMs, a behavior that could potentially arise from either water flooding or dehydration within the cell. If due to flooding, water generated at an increasing rate with higher oxygen concentrations could continue to block the GDL pores. Additionally, for membranes of the same equivalent weight, the relative amount of swelling is similar for both; however, the total amount of swelling could be as much as 15 µm, roughly, for the thicker membrane [135, 136]. This swelling could compress the GDL, influencing the heat and mass transport properties [30]. Conversely, if there is too little water in the thicker membrane, due to lower water uptake associated with increased thickness, this could result in higher ohmic loss in the membrane due to drying out. This ohmic loss can also impact the current density, thus contributing to the observed increase in transport resistance.

Even if the limiting current density data for the 85 µm membrane cells are not truly diffusion-limited, we used this data to measure the D/D_{eff} value and compared it with that of the 25 µm membrane cells, as shown in Table 4.2. As we can see, the D/D_{eff} values obtained for the respective GDLs in cells built with the 85 µm membrane are much higher than those for the 25 µm membrane cells.

GDM	D/D_{eff} for 25 µm cells	D/D_{eff} for 85 µm cells
Toray	5.1	6.1
Freudenberg	3.5	5.6

Table 4.2: Dry D/D_{eff} values, as measured for the cells built with membranes of two different thicknesses. Cell operating conditions: 80°C, 64% RH, 100 300 kPaa..

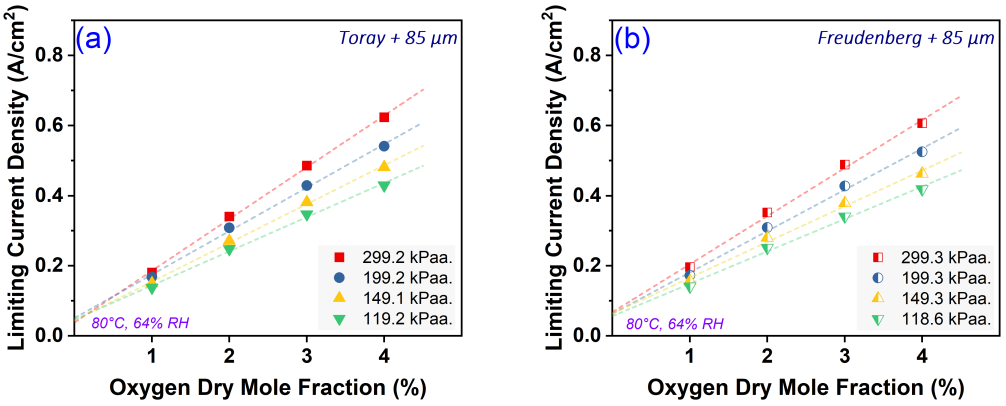

Figure 4.4: . Limiting current density as a function of dry mole fraction of oxygen for four cell pressures in cells built 85 µm membrane using (a) Toray and (b) Freudenberg GDMs; Cell operating conditions: 80°C, 64% RH.

Limiting current experiments are also performed under wet conditions to evaluate the oxygen transport resistance and cell performance for cells with both 25 and 85 µm membranes cells. Results for wet transport resistance and cell performance are presented in Figure 4.5 and Figure 4.6, respectively.

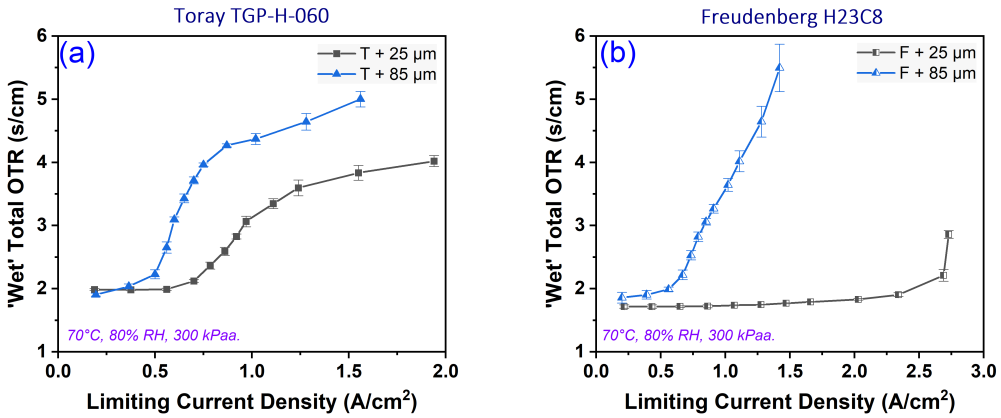

Figure 4.5: Wet oxygen transport resistnace as a function of limiting current density at 80% RH in cells built with (a) Toray and (b) Freudenberg GDMs for both 25 and 85 µm membranes. Cell operating conditions: 70°C, 300 kPa.

As shown in Figure 4.5(a), for Toray, liquid water condensation begins earlier in the cell with the thicker 85 µm membrane, occurring at or before approximately 0.25 A/cm^2, compared to around 0.75 A/cm^2 for the cell with the 25 µm membrane. This effect is even more pronounced in the Freudenberg cells, as shown in Figure 4.5(b), where condensation in the 85 µm membrane cell starts at or before roughly 0.25 A/cm^2, while it initiates at about 2.25 A/cm^2, for the 25 µm membrane cell. These results highlight the significant increase in transport resistance encountered when using a thicker 85 µm membrane in a PEMFC, potentially due to increased issues with liquid water management in the cell built with thicker membranes.

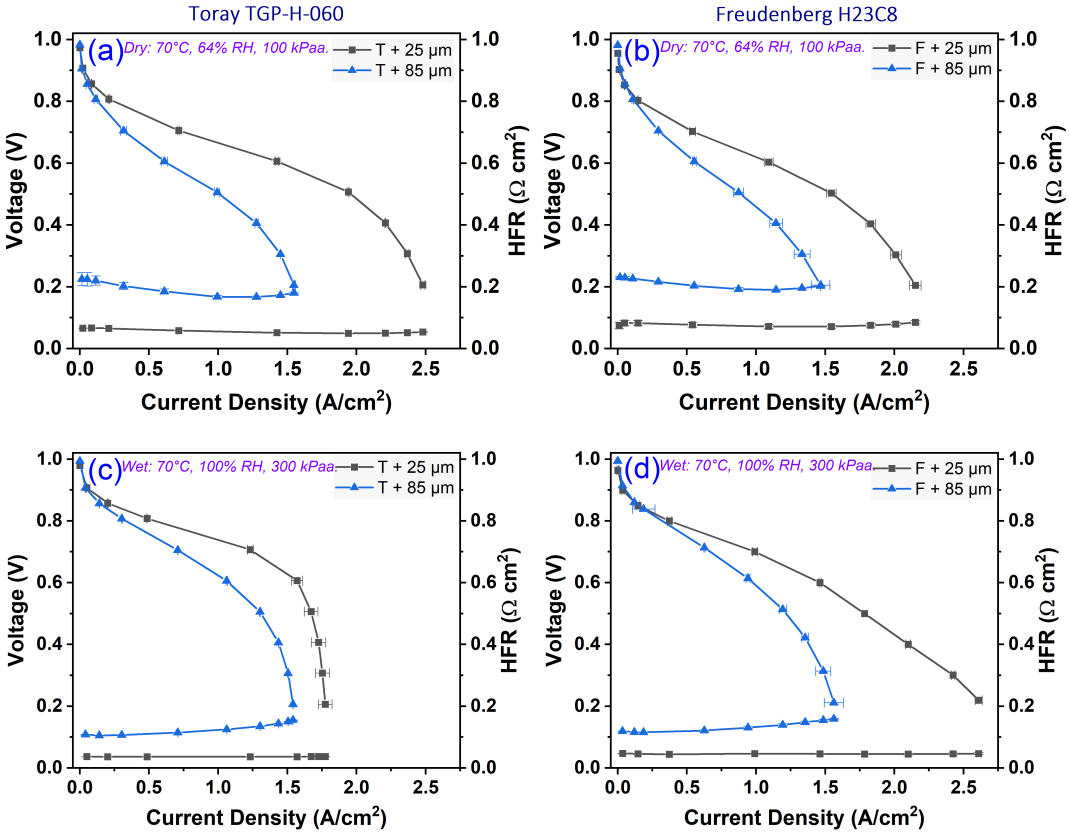

Figure 4.6: Steady-state polarization under (a, b) dry (70°C, 60% RH, 100 kPa) and (c, d) wet (70 °C, 100% RH, 300 kPa) conditions for cells built with 25 and 85 µm membranes using (a, c) Toray and (b, d) Freudenberg GDMs.

Fuel cell performance and high frequency resistance (HFR) under both dry and wet conditions for membranes with two different thicknesses are presented in Figure 4.6 for both GDMs. Notably, the cell performance is significantly better for the thinner 25 µm membrane in both conditions. Specifically, as shown in Figure 4.6(a,b), under dry conditions, cells with a 25 µm membrane achieve a peak current density of 2.50 A/cm^2 and 2.12 A/cm^2 for Toray and Freudenberg GDMs, respectively, compared to just 1.50 A/cm^2 for cells with an 85 µm membrane using either GDM. Similarly, as shown in Figure 4.6(c,b), under wet conditions, cells with a 25 µm membrane reach peak current densities of 1.75 A/cm^2 and 2.6 A/cm^2 for Toray and Freudenberg GDMs, respectively, while those with an 85 µm membrane again show around 1.50 A/cm^2 for both GDMs. The superior performance of the thinner membrane is attributed to higher through-plane proton conductivity, as protons have a shorter distance to travel [137–139]. This is evident in the HFR data, reflecting combination of cell ohmic and electronic resistance; cells with

thicker membranes exhibit higher ohmic resistance, assuming electronic resistance remains constant across all tests. Additionally, thinner membranes achieve better hydration, facilitating easier back diffusion of water generated at the cathode to the anode, crucial for enhancing proton and ionomer conductivity. Thus, thinner membranes offer improved internal water circulation and proton transport, boosting performance. However, thicker membranes provide better open-circuit voltage (OCV) due to reduced fuel crossover and increased shorting resistance from the less electronically conductive, thicker membrane [140]. Nevertheless, this advantage is primarily during the initial activation phase and less beneficial during ohmic and concentration regions.

4.2.3 Effect of GDM compression due to varied membrane thickness

In this part of the study, the impact of the GDM compressions on the oxygen transport properties and cell performance are conducted, with a particular focus on the variations in membrane thickness. Section 4.2.1 outlines the use of a standard NR211 membrane with a thickness of 25 µm in traditional configurations. As demonstrated in Figure 4.7 of the supporting document, increasing the membrane thickness to 85 µm, while keeping the overall cell assembly dimensions unchanged, could results in a significant compression of the GDM. This compression could potentially alter the oxygen transport properties in the cell. To distinctly examine the effect of GDM compression, independent of other variables, PTFE sheets of varied thicknesses alongside the standard 25 µm NR211 membrane is employed. This approach allows for the simulation of GDM compression effects attributable to increased membrane thickness, without the need for physically thicker membranes. The configurations used in this study are detailed in Table 4.3.

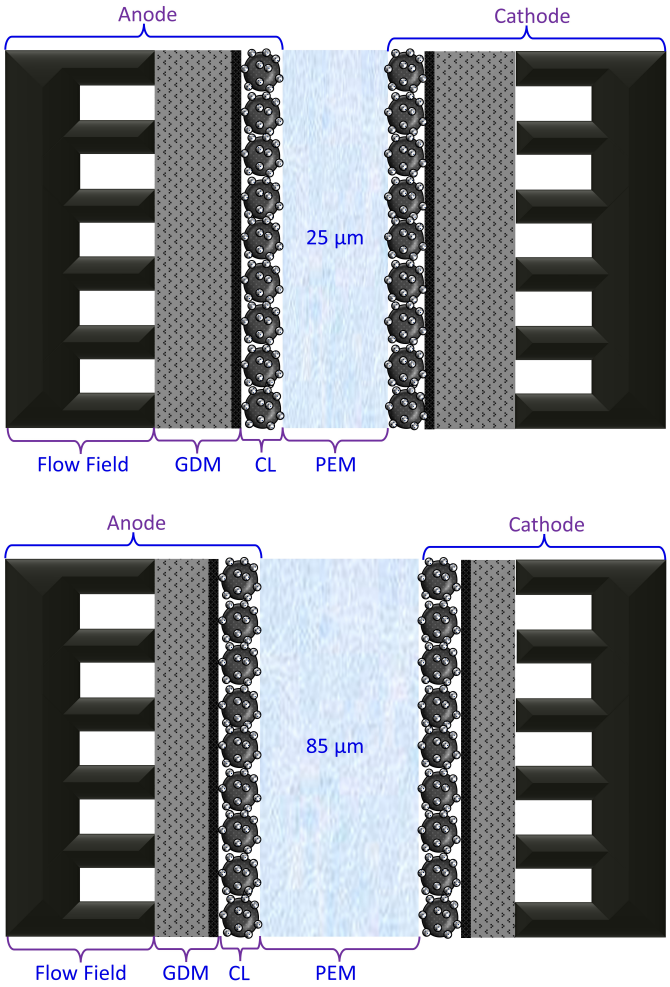

Figure 4.7: Illustration of increased GDM compression resulting from thicker membrane usage.

GDM Compression (%)	Membrane thickness (µm)	AN GDM (µm)	CA GDM (µm)	AN PTFE (µm)	CA PTFE (µm)	Comment
17.5%	25	206.4	210.4	180	182	All fresh cell materials.
24.3%	↑	↑	↑	150	↑	All materials from 17.5% cell except that the used AN PTFE is replaced with a new PTFE of different thickness.
31.6%	↑	↑	↑	↑	150	All materials from 24.3% cell except that the used CA PTFE is replaced with a new PTFE of different thickness.

Table 4.3: Cell configurations for investigating GDM compression effects with Freudenberg H23C8 GDM in response to increased membrane thickness.

For simplification and to ensure clarity in our findings, only the Freudenberg H23C8 GDM is chosen for this series of experiments. This choice aims to minimize complexity and focus specifically on the results related to GDM compression due to the use of membranes of different thicknesses. A reference cell, assembled with the Freudenberg GDM under standard compression (17.5%), serves as the baseline for comparison. To test the hypothesis regarding GDM compression, two additional cells are assembled with increased strains. The first of these additional cells is subjected to a compression of 24.3%, achieved by utilizing a PTFE gasket that is 30 µm thinner on the anode side. This setup simulates the effect of using a membrane with an effective thickness of 55 µm (25 µm standard membrane + 30 µm additional thickness). Subsequently, the second additional cell is compressed further to 31.6%, using a PTFE gasket that is 32 µm thinner on the cathode side, to mimic the scenario of employing a membrane with a total thickness of 87 µm (25 µm standard membrane + 30 µm + 32 µm additional thickness). This thickness closely approximates the 85 µm membrane sample incorporated in our investigation.

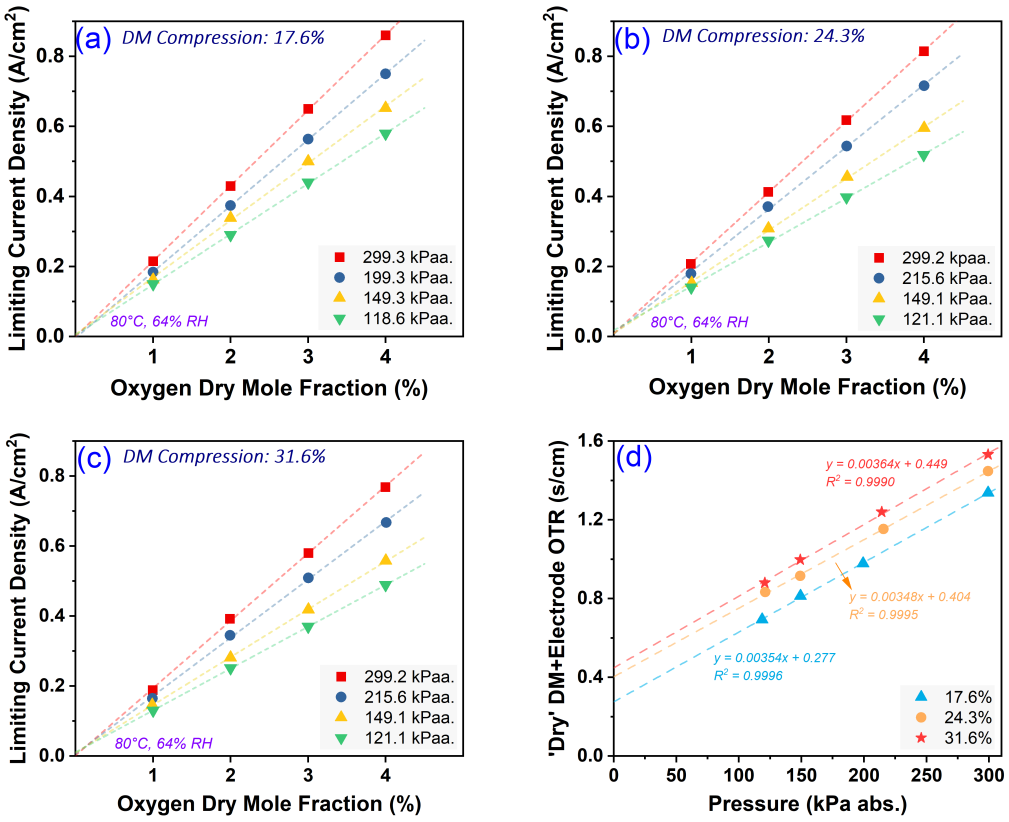

Figure 4.8: Limiting current density as a function of dry mole fraction of oxygenfor four different cell pressures in cells built with 25 µm membrane under GDM compression levels of (a) 17.6%, (b) 24.3%, and (c) 31.6%; (d) combined transport resistance in the GDM and electrode as a function of cell pressure for each compresson level. Cell operating conditions: 80°C, 64% RH.

GDM Compression (%)	Compressed CA GDM (µm)	D/D_{eff} (-)	R_{Others} (s/cm)
17.5%	179.6	3.67	0.299
24.3%	157.7	4.00	0.426
31.6%	142.5	4.54	0.473

Table 4.4: Summary of oxygen transport property results obtained from Figure 4.8.

Figure 4.8 shows that increased GDM strain does not replicate the behavior observed with the 85 µm membrane (Figure 4.3(b) or Figure 4.4(b)). For all tested compression levels and cell pressures, the limiting current density approaches zero as

the oxygen dry mole fraction decreases. A notable finding from Figure 4.8 is the rise in R_{Others}, which represents pressure-independent transport resistances, commonly referred to as Knudsen diffusion. This is inferred from the trend line's intercept with the axis in the oxygen transport resistance versus pressure graph, suggesting that the compression may cause sufficient pore reduction in the GDM to induce Knudsen diffusion [141]. This targeted examination of GDM strain leads to the conclusion that GDM swelling alone cannot explain the peculiar performance of the thicker 85 µm membrane. Furthermore, the limiting current summary results are tabulated in Table 4.4. It is observed that the D/D_{eff}, which is also known as the ratio of GDM tortuosity to the porosity [102], increases with increasing compression. This suggests a reduction in GDM pore size under higher compression levels, aligning with literature [142, 143]. However, the pronounced increasing transport resistance associated with the 85 µm membrane, as depicted in Figure 4.3(f), remains unexplained.

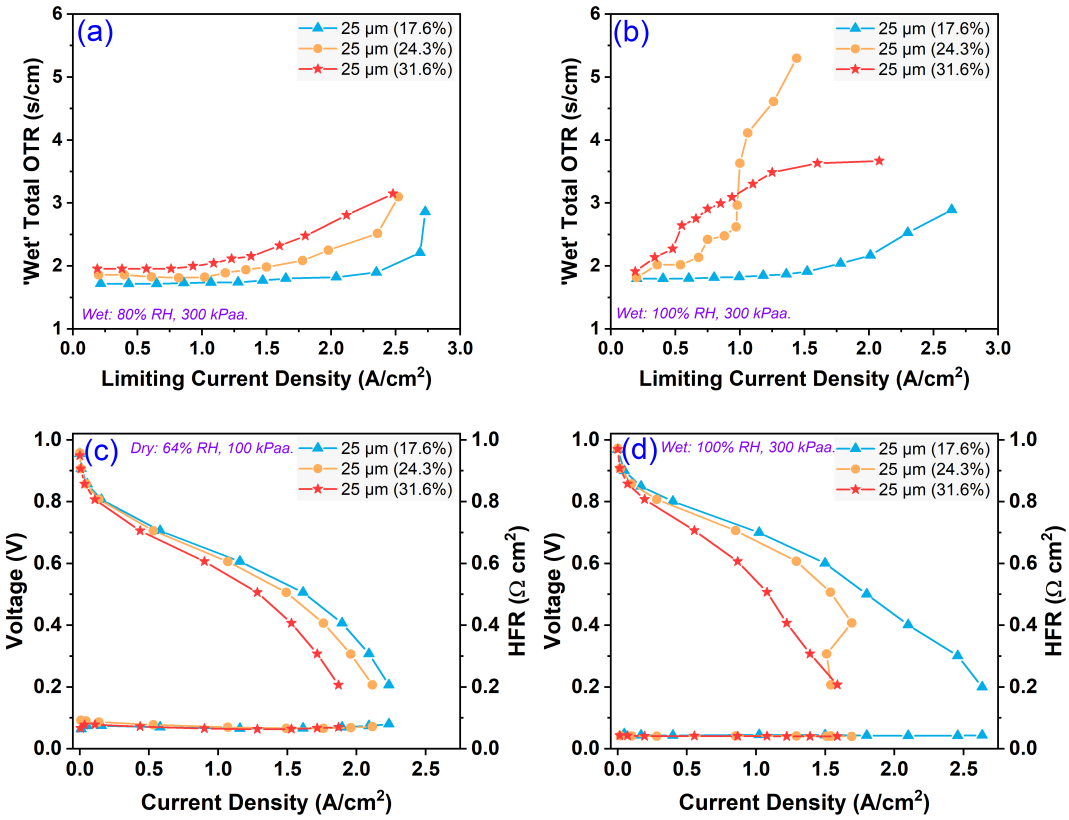

Figure 4.9: Total wet oxygen transport resistance as a function of the limiting current density under (a) 80% and (b) 100% RH; steady-state polarization for cells with 25 µm membrane and varying Freudneberg GDM compression levels under (c) dry (70°C, 60% RH, 100 kPa) and (d) wet (70°C, 100% RH, 300 kPa) conditions.

Limiting current experiments are also performed under wet conditions to evaluate the oxygen transport resistance and cell performance for cells with 25 µm membrane and three compression levels of GDM. Results for wet transport resistance and cell performance are presented in Figure 4.9(a,b) and Figure 4.9(c,d), respectively.

4.2.4 Effect of cell temperature

To further explore the reasons behind the observed deviation in oxygen transport resistance (OTR) behavior, sensitivity analysis on limiting current method is performed. This analysis focuses on three key parameters in Equation 4.4: temperature, pressure, and partial pressure of water i.e., relative humidity.

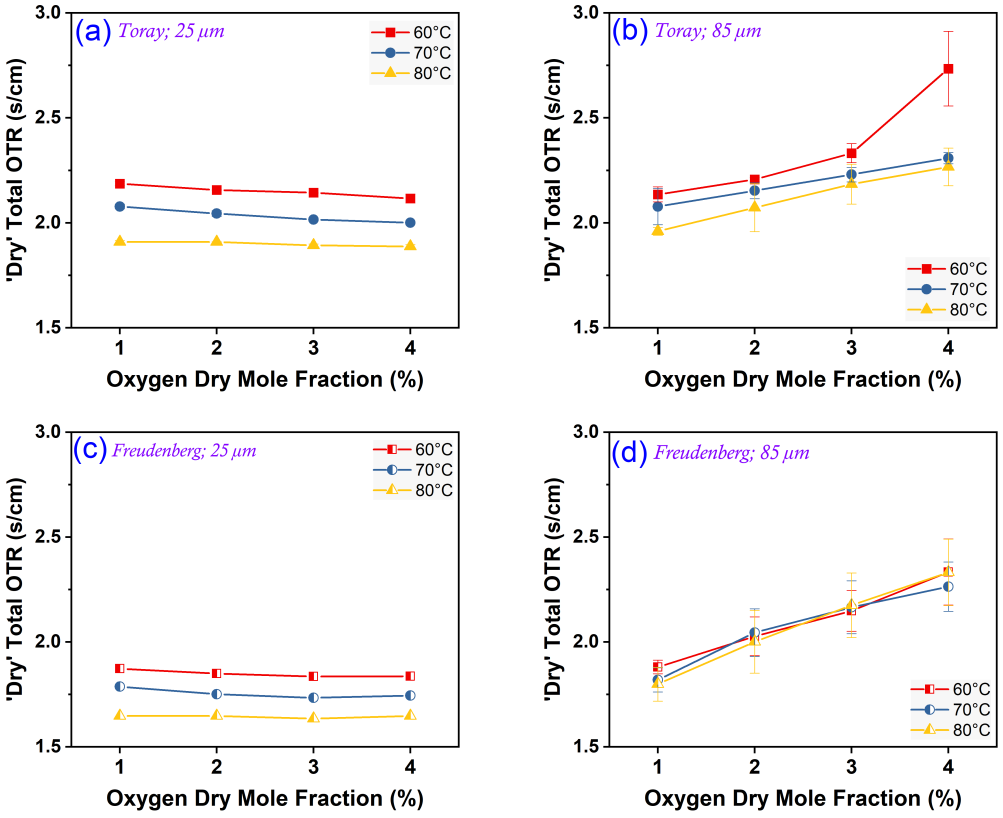

Figure 4.10: Oxygen transport resistance as a function of dry mole fraction of oxygen at three different cell temperatures in cells built (a) Toray and 25 µm, (b) Toray and 85 µm, (c) Freudenberg and 25 µm, and (d) Freudenberg and 85 µm. Cell operating conditions: 64% RH, 300 kPa.

The relationship in Equation 4.4 indicates that an increase in temperature should lead to a corresponding decrease in the oxygen transport resistance (OTR). Because higher temperatures facilitate the evaporation of water, reducing the water content in the catalyst and diffusion layers, thereby which aids oxygen transport and reduces overall oxygen transport resistance [144]. In Figure 4.10, OTR is evaluated at 60°C, 70°C, and 80°C across two GDM materials and the two previously examined membrane thicknesses. As can be observed in Figure 4.10(a,c), the trend aligns with expectations and literature for both GDMs [145]. However, the results diverge with the 85 µm membrane. As in Figure 4.10(b), with the Toray material and thicker membrane, OTR values increase at higher supplied oxygen mass fractions and are not vertically evenly spaced between temperatures. For the 70°C and 80°C cases, there is significant overlap in values at higher mass fractions. At 60°C, the values show a non-linear increase and shift upward dramatically, potentially due to water condensation in the GDM at reduced temperature. Similarly, as depicted in Figure 4.10(d), with the Freudenberg material and thicker membrane, measured OTR values at all temperatures fully overlap and exhibit an upward trend. The error bars indicate considerable variation between tests. Given these observations and the trends observed, the change in the cell's water transport properties can begin to be considered as the source of these behaviors. The presence of liquid water in the GDM undoubtedly increases OTR, and the current signal becomes notably more erratic as water forms and removed from the GDM into the channel.

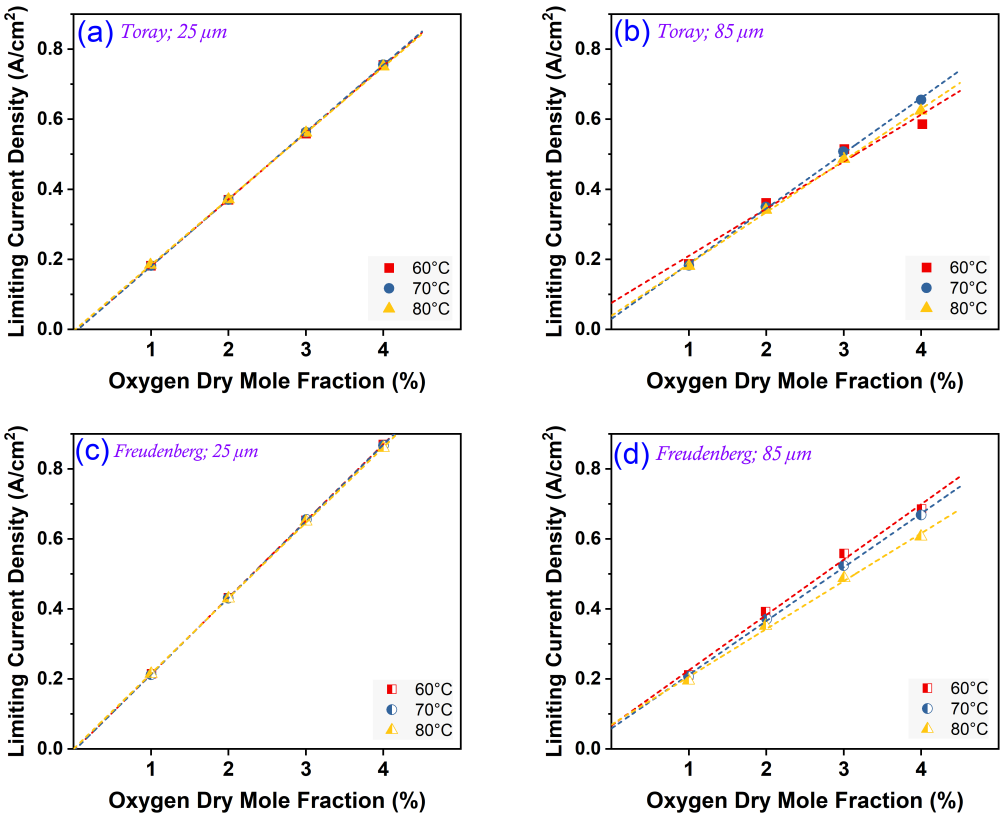

Figure 4.11: Limiting current density as a function of dry mole fraction of oxygen at three different cell temperatures in cells built (a) Toray and 25 µm, (b) Toray and 85 µm, (c) Freudenberg and 25 µm, and (d) Freudenberg and 85 µm. Cell operating conditions: 64% RH, 300 kPa.

The limiting current data as a function of oxygen concentration, serving as the basis for the analysis presented in Figure 4.10, is plotted in Figure 4.11. Consistent with earlier findings, the linear trend lines for cells with the 25 µm membrane extrapolate back to the origin. Conversely, for cells with the thicker 85 µm membrane, the trend lines do not reach zero, deviating slightly above the origin, indicating a distinct behavior associated with the increased membrane thickness.

4.2.5 Effect of cell pressure

The relationship in Equation 4.4 indicates that oxygen transport resistance (OTR) is anticipated to rise with an increase in pressure. Given observations from the temperature sensitivity and the suspected change in water transport properties, asymmetric backpressures are held within the cell to drive more water from one side of the cell to the other thus exacerbate or alleviate water presence on the cathode.

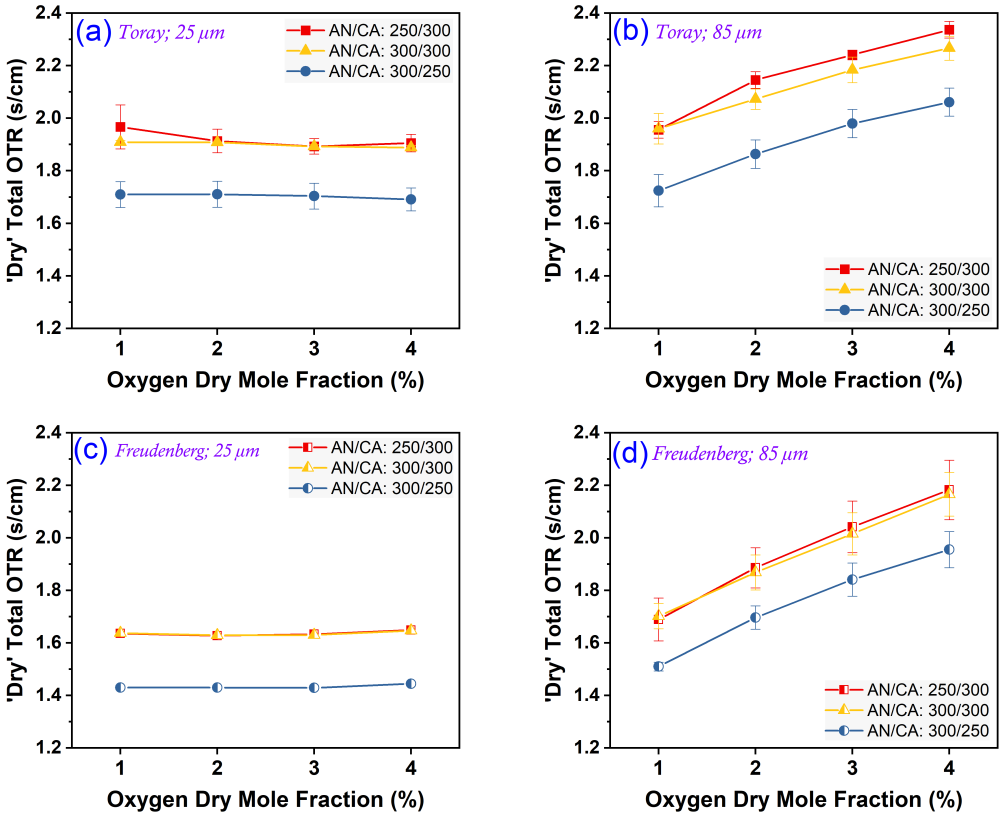

Figure 4.12: Oxygen transport resistance as a function of dry mole fraction of oxygen at three different ssymmetric pressure combinations in cells built (a) Toray and 25 µm, (b) Toray and 85 µm, (c) Freudenberg and 25 µm, and (d) Freudenberg and 85 µm. Cell operating conditions: 80°C, 64% RH.

In each plot of Figure 4.12, OTR is plotted against the dry mole fraction of oxygen for a specific GDM-membrane combination across three different anode-cathode backpressure combinations. The anode pressure doesn't seem to induce any variation in the test results, suggesting minimal dependence of cell performance on the anode side in PEMFCs. Notably, OTR increases with cathode pressure in all cases, as expected. For cells built with the 85 µm membrane, OTR consistently rises with oxygen concentration, indicating an upward trend in transport resistance. Thus, similar to previous observations, the 85 µm exhibit greater variance compared to those with a thinner membrane. This implies that, if water is contributing to these observations, the pressure gradients tested might not be sufficient to significantly impact it.

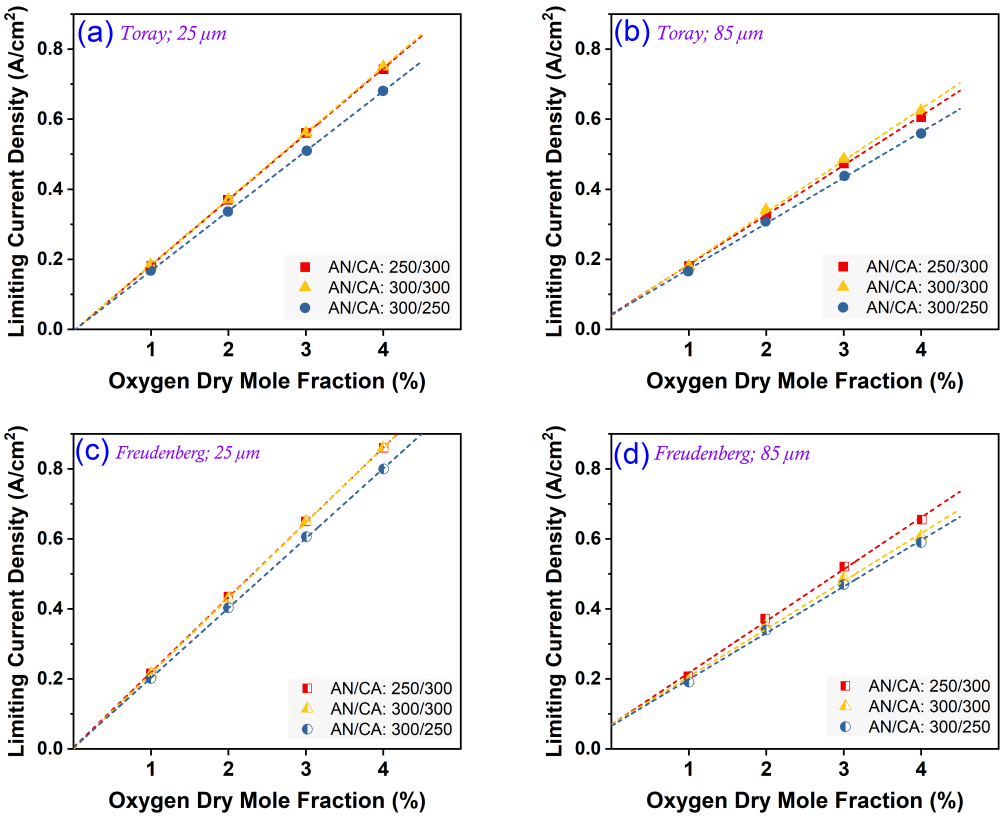

Figure 4.13: Limiting current density as a function of dry mole fraction of oxygen at three different ssymmetric pressure combinations in cells built (a) Toray and 25 µm, (b) Toray and 85 µm, (c) Freudenberg and 25 µm, and (d) Freudenberg and 85 µm. Cell operating conditions: 80°C, 64% RH).

The limiting current data as a function of oxygen concentration, serving as the basis for the analysis presented in Figure 4.12, is plotted in Figure 4.13. Consistent with earlier findings, the linear trend lines for cells with the 25 µm membrane extrapolate back to the origin. Conversely, for cells with the thicker 85 µm membrane, the trend lines do not reach zero, deviating slightly above the origin, indicating the same distinct behavior associated with the increased membrane thickness.

4.2.6 Effect of cell RH

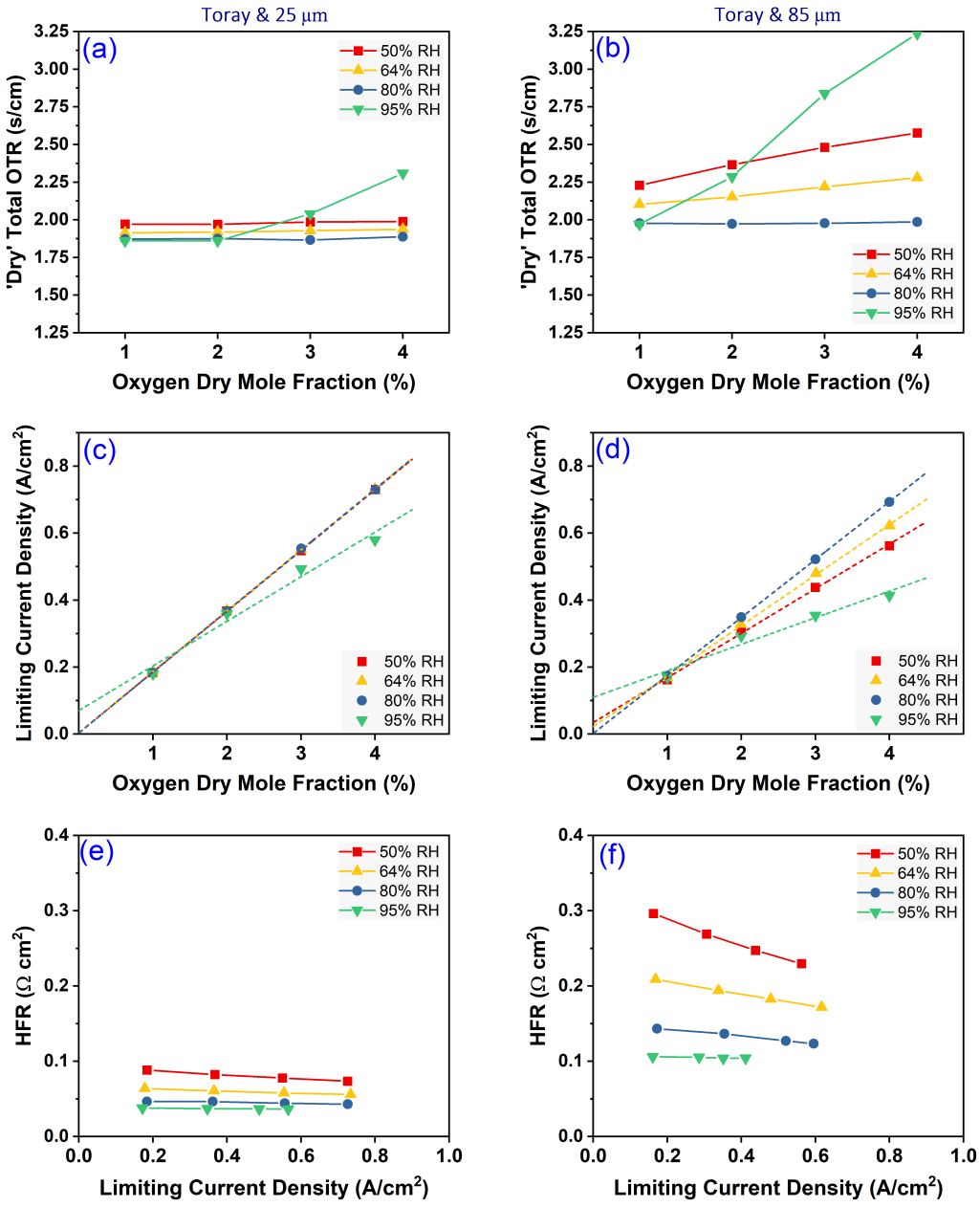

Figure 4.14: Plots of oxygen transport resistance, limiting current density, and HFR for cells built with Toray material using (left) 25 µm and (right) 85 µm membranes under four different relative humidity (RH) conditions. (a,b) Oxygen transport resistance as a function of dry mole fraction of oxygen, (c,d) limiting current density as a function of dry mole fraction of oxygen, and (e,f) high frequency resistance (HFR) as a function of limiting current density. Cell operating conditions: 80°C, 300 kPaa..

The relationship in Equation 4.4 suggests that oxygen transport resistance (OTR) is expected to decrease with an increase in relative humidity or cell water content, until excessive condensation causes pore flooding within the GDM. In Figure 4.14, OTR, limiting current density, and HFR are plotted against the dry mole fraction of oxygen, dry mole fraction of oxygen, and limiting current density, respectively, across a range of relative humidities (50, 64, 80, 95% RH) for the cells built with Toray GDL and 25 and 85 µm membranes. 4.14(a) shows that for the cell with 25 µm membrane, there is a decreasing trend in the slope of the transport resistance versus oxygen concentration as RH increases, with flooding occurring at 95% RH above 2% oxygen concentration. Conversely, Figure 4.14(b) demonstrates that for the cell with 85 µm membrane, the slope diminishes with increasing RH, becoming almost flat at 80% RH. This suggests that this transport resistance is driven by concentration-driven limiting current. The limiting current data, used as the basis for analysis are shown in Figure 4.14(c,d). As shown in Figure 4.14(d), for the cell with 85 µm membrane, the extrapolated trend line between limiting current density and oxygen concentration approaches zero as RH increases. At 80% RH, the line reaches zero, but at 95% RH, there is a significant increase in transport resistance due to severe flooding. This can be further corroborated from the HFR data, depicted in Figure 4.14(e,f). HFR represents the combined electronic and ionic resistance in the cell. Since electronic resistance does not change significantly from one cell to another, any variation in HFR can be attributed to the proton resistance in the membrane. As shown in Figure 4.14(e), for 25 µm membrane cell, HFR remains constant across all current densities and shows a decreasing trend with increasing RH, indicating more efficient proton transport associated with higher water content. In contrast, as shown in Figure 4.14(f), for 85 µm membrane cell, the drying effect is apparent at 50 and 64% RH, with HFR reducing at high current densities, which generate more water in the cell and also decrease with increasing RH. The condition at 80% RH provides enough water for adequate proton transport through the membrane, making the limiting current density at this RH truly diffusion-limited, as validated by the extrapolated line returning to zero in Figure 4.14(d). However, the cell encounters flooding issues at higher RH conditions like 95% RH.

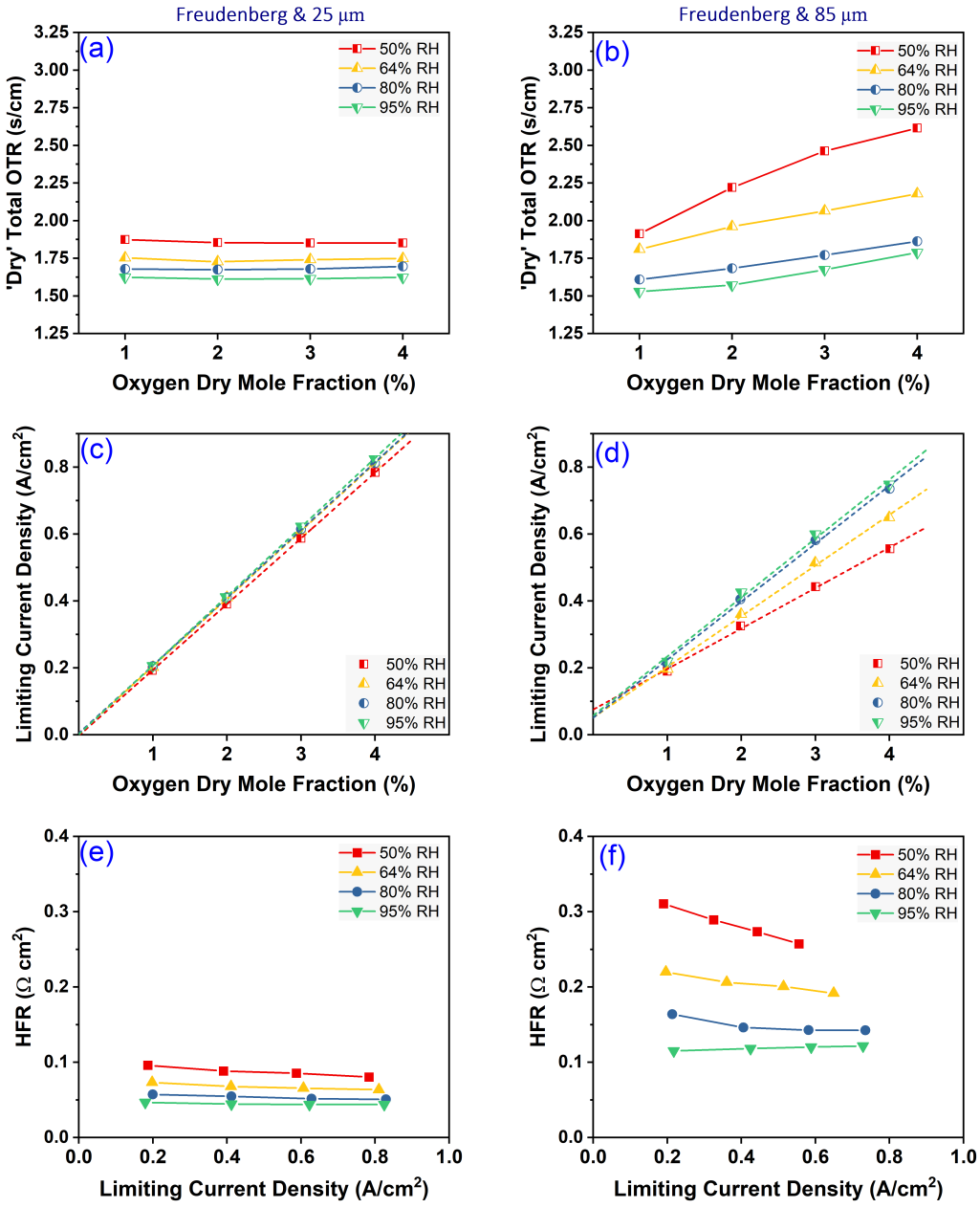

Figure 4.15: Plots of oxygen transport resistance, limiting current density, and HFR for cells built with Freudenberg material using (left) 25 µm and (right) 85 µm membranes under four different relative humidity (RH) conditions. (a,b) Oxygen transport resistance as a function of dry mole fraction of oxygen, (c,d) limiting current density as a function of dry mole fraction of oxygen, and (e,f) high frequency resistance (HFR) as a function of limiting current density. Cell operating conditions: 80°C, 300 kPaa..

Similar to the Toray cells, Figure 4.15 represents plots of OTR, limiting current density, and HFR against the dry mole fraction of oxygen, the dry mole fraction of oxygen, and limiting current density, respectively, across a range of relative humidities (50, 64, 80, 95% RH) for cells built with Freudenberg GDL and 25 and 85 µm membranes. For the cell with 25 µm membrane, a decreasing trend in the slope of the transport resistance versus oxygen concentration with increasing RH is observed. Unlike the Toray GDL, which experiences flooding at 95% RH, the Freudenberg GDL shows the ability to manage the liquid water even at a 95% RH for the thinner membrane. However, as shown in Figure 4.15(d), for cell with 85 µm membrane, the slope of the transport resistance relative to the dry mole fraction of the oxygen flattens with increasing RH but never reaches a plateau.

Considering these findings alongside previously discussed outcomes, it becomes evident that the water content significantly influences the cell's behavior. This interplay between relative humidity and OTR underscores the delicate balance required in managing water content within the cell to obtained reliable results from limiting current experiments for any specific type of GDL and membranes with thickness higher than standard thickness.

4.3 Summary

In summary, this investigation into the impact of membrane thickness and operating conditions on limiting current analysis in PEMFCs has illuminated several critical insights. The study demonstrates that membrane thickness significantly influences oxygen transport resistance, with thicker membranes deviating from expected limiting current behavior due to altered water management within the cell. Specifically, our findings reveal that increased membrane thickness can exacerbate issues with liquid water condensation and transport, leading to a notable rising trend in oxygen transport resistance with oxygen concentration. The sensitivity analysis focusing on temperature, pressure, and humidity further underscores the intricate relationship between these operational conditions and the accurate determination of limiting current. Increasing relative humidity to 80% for the 85 µm membrane using Toray GDM resulted in improved oxygen transport resistance (OTR) data, suggesting a beneficial alteration in water balance within the cell. This contrasts with the results obtained for Freudenberg GDM, where no clear trend emerged, highlighting the complex interplay between GDM type, membrane thickness, and operational conditions. Through a comprehensive examination of these factors, we have identified key considerations for the correct application and interpretation of the limiting current method in PEMFCs. This work contributes to the fundamental understanding of the method's limitations and potentials, paving the way for refined diagnostic techniques that can more accurately reflect the intricate interactions within fuel cells. Future research should continue to explore these dynamics,

particularly the role of water management in influencing transport resistance, especially when using a membrane thicker than standard 25 µm thickness, to enhance the predictive accuracy and reliability of limiting current measurements in PEMFC systems.

Acknowledgement

This work is supported by the University of California (United States), Merced and the CIPHER Program (IIID 2018-008) from the Commission on Higher Education – Philippine California Advanced Research Institutes (CHED-PCARI) of the Republic of the Philippines. I would like to thank Felipe for his unparalleled expertise in data analysis and his significant contributions to the writing of this project, which were absolutely instrumental in its completion.

Chapter 5

UNVEILING THE POTENTIAL OF A HIGH OXYGEN PERMEABLE IONOMER-BASED PT/C CATALYST INK IN PEMFC VIA MEA PERFORMANCE & DURABILITY EXPERIMENTS

Fuel cell durability is a key limitation for its commercialization in heavy-duty applications. Cathode catalyst layers need to be designed to demonstrate not only high oxygen reduction reaction (ORR) mass activity and cell performance but also significanlt durability during long-term operation. Ion-conducting polymers, or ionomers, play a crucial role in determining both performance and durability in a PEMFC. A highly oxygen permeable ionomer (HOPI), developed by Chemours^{TM}, is explored in this project; it is known for higher ORR mass activity and lower oxygen transport resistance through its thin film. This investigation involves using HOPI to fabricate the cathode catalyst layer of a PEM fuel cell. Cells prepared with HOPI are compared with those using the standard or conventional Nafion D2020^{TM} ionomer. We aim to examine the impact of this newly developed ionomer on cell durability, oxygen transport in the ionomer thin film, cathode proton transport, and overall cell performance, utilizing in situ fuel cell electrochemical diagnostics. First, the durability of the HOPI cell is compared with that of the D2020 by conducting DOE 5000 MEA accelerated stress test (AST) cycles. Then, the cathode proton resistance, both before and after the AST cycles, is examined and compared. Subsequently, the oxygen transport resistance—specifically the electrode resistance - for both ionomers is compared before and after AST. Finally, the cell performance and the H_2/Air mass activities for both ionomer cells are compared. The insights gleaned from these comprehensive analyses aim to guide the optimization of ink formulation and ionomer selection, thereby enhancing the formation of catalyst layers and improving the performance and durability of proton exchange membrane fuel cells.

5.1 Experimental

5.1.1 Fuel cell materials

Commercially available Toray TGP-H-060 (wetproofed, with MPL incorporated) was used as gas diffusion media (GDM) material. The thickness strains of the GDM, along with catalyst loadings, are listed in Table 5.1. As earlier mentioned,

14-µm reinforced and checmically stabilized NC700 Nafion perfluorosulfonic acid (PFSA) membrane from Chemours^{TM} was used to fabricate the MEA. Note that D2020 ionomer was used as the anode catalyst ionomer for both cells, while D2020 and pre-commercial high oxygen permeability ionomer (HOPI) were employed as cathode catalyst materials for the two cells.

Graphite flow fields with straight parallel channel designs were used on both anode and cathode. The total channel area of 4 cm^2 was masked down to 2 cm^2 using PTFE gaskets to achieve differential cell conditions (i.e., minimal pressure drop, uniform temperature and RH at channel inlets and outlets) [24]. PTFE gaskets also serve to avoid electrical shorting between anode and cathode sides and to avoid any leakage of the reactant gases.

Cathode Ionomer	CA GDM (µm)	GDM Strain (%)	I/C Ratio (-)	AN/CA Loading (mg_{Pt}/cm^2_{MEA})
D2020	218.4	22.4	0.85	0.121/0.214
HOPI	210.4	23.3	0.80	0.102/0.221

Table 5.1: Cell configurations (anode ionomer: D2020).

5.1.2 In-situ fuel cell characterizations and accelerated stress testing

A fully automated Greenlight G20 fuel cell test station was used to perform fuel cell experiments. A Gamry Reference 3000 Potentiostat with a 30k Booster was employed to perform electrochemical impedance spectroscopy (EIS) for measuring the high frequency resistance (HFR) [132]. All gases used (hydrogen, air, and nitrogen) were ultra-high purity with 99.999% purity. The anode and cathode flow rates for polarization and limiting current experiments were 0.40 and 2.0 NLPM, respectively.

In the beginning, cyclic voltammetry (CV) was performed at a scan rate of 50 mV/s to measure the electrochemically active surface area (ECSA) of the MEAs. A 16-cycle break-in protocol was then employed to activate the catalyst layer by cycling the cell voltage between open circuit voltage (OCV), 0.40, 0.60, 0.70, and 0.85 V. The activation was done under fully humidified conditions at 70 °C to enhance proton conductivity, using a flow stoichiometry of 10 and an absolute backpressure of 150 kPa on each side. For characterizing the MEA, fuel cell performances were measured under dry (70 °C, 64% RH, 100 kPaa.), wet (70 °C, 100% RH, 300 kPaa.) conditions. Additionally, another condition (88 °C, 40% RH, 250 kPaa.) similar to that suggested by the DOE was used and named 'DOE-DryPol' [109]. Then the oxygen transport resistances were measured under dry (80 °C, 64% RH, 100 300 kPaa., 1∼4% O_2 concentration) and wet (70 °C, 100% RH, 300 kPaa., 1∼21% O_2 concentrations) conditions. In addition, a time-sensitive experiment was performed to

measure the cathode proton resistance under three different RH (relative humidity) conditions along with the membrane proton resistance. Subsequently, 5000 cycles of H_2/Air MEA AST (accelerated stress test) were performed by cycling the cell voltage in a wave form between 0.675 V and 0.925 V for 30 seconds each at 90 °C, 90% RH, 250 kPaa. [146]. Finally, cell performances, oxygen transport resistances, time-sensitive sheet resistances, and ECSA were measured after the 5000 MEA AST cycles. A summarized list of test protocols is tabulated in Table 5.2.

Test	Temp. (°C)	RH (%)	Pressure (kPa abs.)	Voltage range (V)
Cyclic Voltammetry	30	100	100	0.05-1.2
Break-in	70	100	150	OCV-0.40
Dry limiting current	80	64	100∼300	0.30-0.09
Wet limiting current	70	80	300	0.30-0.09
Dry i-V	70	60	100	OCV-0.20
Wet i-V	70	100	300	OCV-0.20
DOE-DryPol i-V	88	40	250	OCV-0.20
Sheet resistance	70	40∼100	300	0.20
5k cycles MEA AST	88	90	250	OCV-0.20
Dry limiting current	80	64	100∼300	0.30-0.09
Wet limiting current	70	80	300	0.30-0.09
Dry i-V	70	60	100	OCV-0.20
Wet i-V	70	100	300	OCV-0.20
DOE-DryPol i-V	88	40	250	OCV-0.20
Sheet resistance	70	40∼100	300	0.20

Table 5.2: Fuel cell testing protocols.

5.2 Results and discussion

5.2.1 MEA health and break-in

The ECSA of the cells are measured using HAD method [51]. The crossover current for both cells is found to be 2 mA/cm^2_{MEA}, and the cathode ECSA of both cells is found to be around 50 m^2/gm, indicating the cells are in good beginning-of-life conditions. A fully humidified break-in protocol is then employed to activate catalyst and all proton-conducting domains or pathways. As shown in Figure 5.1, the cell utilizing HOPI ionomer exhibits superior break-in performance compared to that of the D2020 cell. Although the D2020 cell shows better performance at the initial five cycles or higher potential ranges (e.g., 0.60 and 0.85 V), the HOPI cell surpasses its performance as the break-in progresses to lower potential ranges (e.g.,

0.40 and 0.70 V) or higher current densities. Furthermore, the HOPI cell reaches to a plateau in current density much earlier than the D2020 cell, maintaining a consistent current density of 1 A/cm^2 at 0.60 V during the last six cycles of break-in, unlike the D2020 cell, which shows an increasing trend in current density from 0.54 to 0.85 A/cm^2 at 0.60V. The superior break-in performance and quicker achievement of a steady and high current density by the HOPI cell can be attributed to the enhanced water retainability of the HOPI ionomer, which facilitates better proton conductivity more rapidly. As shown in Figure 5.2, the OCV for both cells through the different set of experiments are demonstrated and it is found that the HOPI cell showed better OCV for all the experiments conducted. It should be noted that a cell's OCV is primarily determined by shorting and crossover through the membrane, with the ionomer in the catalyst layer having little to no impact.

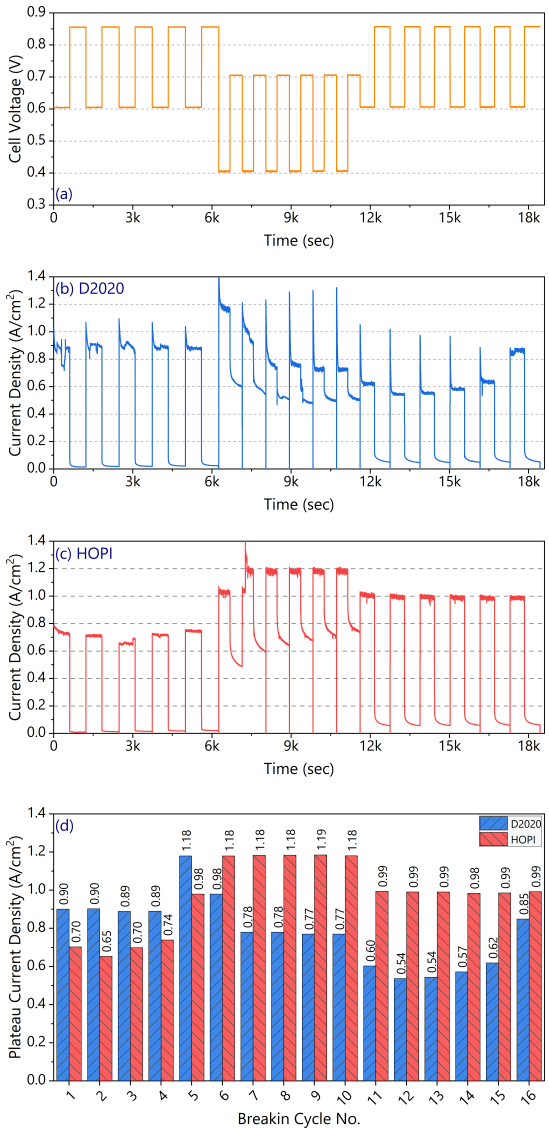

Figure 5.1: Cell voltages during the 16 break-in cycles, and current density responses for the associated voltages for (b) D2020 and (c) HOPI ionomer-based MEA, and (d) the plateau current densities observed for each cycle. Cell operating conditions: 70 °C, 100% RH, 150 kPaa., H_2/Air stoichiometry: 10/10.

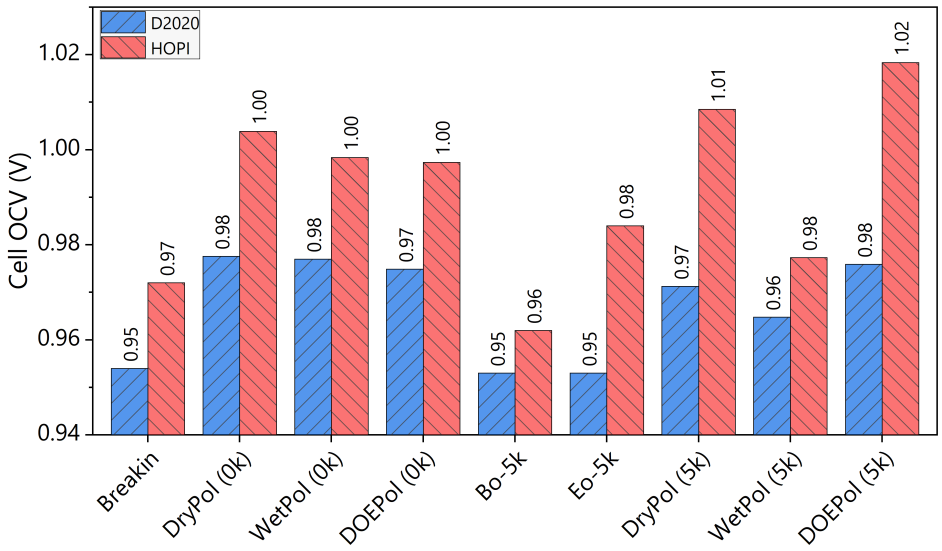

Figure 5.2: Comparison of open circuit voltage (OCV) for HOPI and D2020 ionomer-based cells across various experimental stages.

5.2.2 AST performance

Both cells underwent 5,000 cycles of accelerated stress tests (AST), during which hydrogen and air are flown to the anode and cathode, respectively. Each cycle lasted one minute, alternating between 0.675 V for 30 seconds and 0.925 V for the remaining 30 seconds. Since a reinforced membrane is used, no significant decline in the cell OCV is observed following the AST, suggesting negligible increase in internal current or notable membrane degradation. Subsequently, data corresponding to 0.925 V are excluded, and the current density at 0.675 V for both cells is represented in Figure 5.3. Here, the HOPI cell's performance markedly surpasses that of the D2020 cell throughout the AST. Moreover, the degradation rate of the HOPI cell is found to be 0.112 mA/cm^2 per cycle, approximately 23% lower than the D2020 cell's rate of 0.145 mA/cm^2 per cycle. There are some fluctuations in the current density for HOPI cell after 2k cycles and for D2020 cell after 3k cycles. This is due to an artifact caused by faulty pressure control of the test operation while changing nitrogen gas cylinder, which lasted for approximately 10 minutes. Despite a brief disruption in current density during this procedure, the overall trend realigned with the pre-existing pattern shortly thereafter.

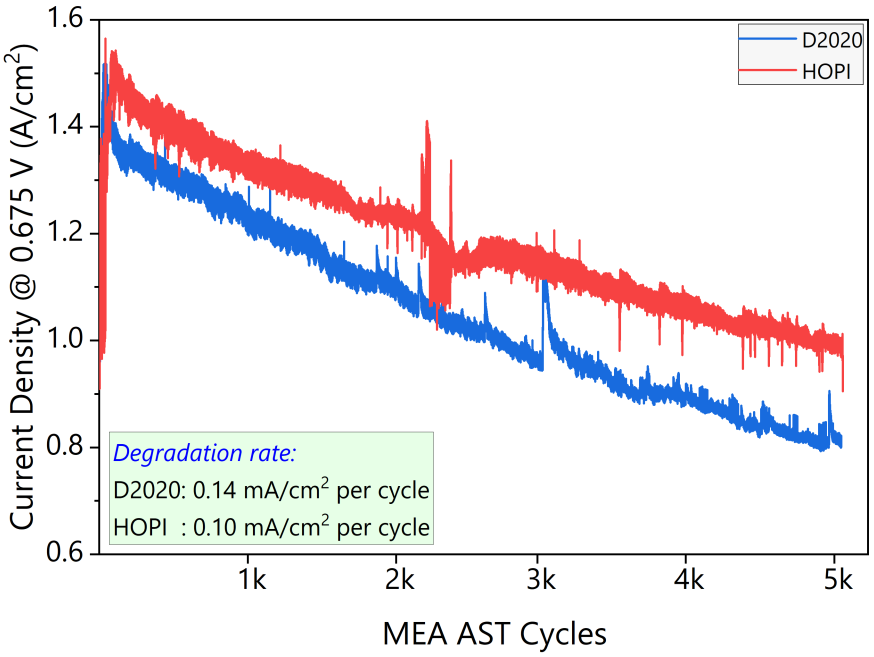

Figure 5.3: Current density trend at 0.675 V as extracted during 5000 cycles of H_2/Air MEA AST by cycling the voltage in square wave form between 0.675 and 0.925 V at 90 °C, 90% RH, 250 kPa abs. (some initial cycles trimmed down due to fluctuating current densities indicating break-in behavior).

5.2.2.1 Proton resistance measurement

The proton transport resistance, commonly referred as sheet resistance, at the cathode catalyst layer and the membrane proton transport resistances, are measured across a wide range of RH conditions from 100% down to 40% RH. At steady-state conditions of 100%, 70%, and 40% RH, a series of 3, 5, and 10 electrochemical impedance spectroscopy (EIS) measurements are taken respectively, at 10-minute intervals to investigate the ionomer's proton conductivity behavior over time. The cathode proton transport resistance across various RH levels is depicted in Figure 5.4, where the HOPI ionomer consistently exhibits lower proton transport resistance at the cathode catalyst layer. Notably, the proton transport resistance for the HOPI ionomer remains nearly unchanged pre- and post-AST between 100% and 70% RH, and it is lower than that of a fresh D2020 ionomer. This significant finding underscores the superior durability in maintaining proton conductivity of the HOPI ionomer within the catalytic layer through the AST process. Furthermore, even under relatively drier conditions of 40% RH, the post-AST HOPI ionomer shows

significantly lower proton transport resistance as compared to the D2020 ionomer. In addition, the proton transport resistance within the membrane is evaluated from the Nyquist plot, as presented in Figure 5.5. Despite using a similar type of membrane, the HOPI cell's membrane resistance after 5k cycles remains lower than that of the D2020 ionomer. This observation suggests that the HOPI ionomer's enhanced water retention capacity at the catalyst layer may facilitate more efficient proton transport from the membrane to the cathode electrode.

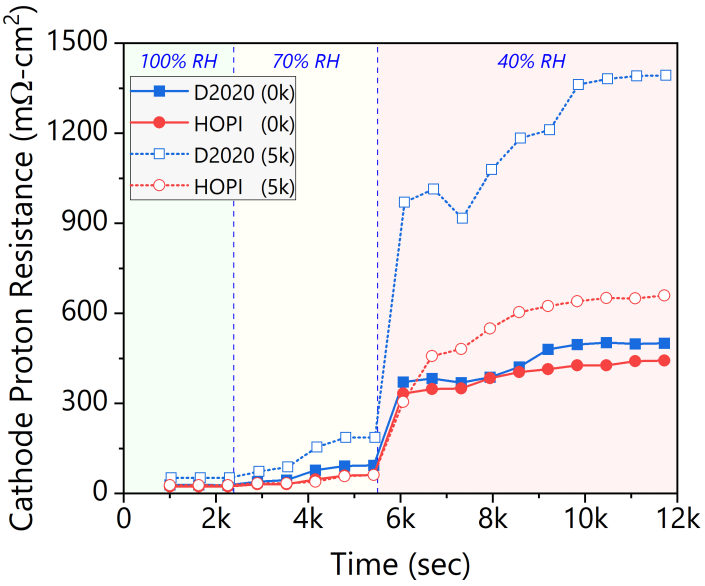

Figure 5.4: Cathode proton transport resistance measured from the 45° line from a Nyquist plot. Cell operating conditions: H/N_2, 70 °C, 40∼100% RH, 300 kPa abs., 0.20 V DC, 10 mV AC. Solid symbols with straight lines represent data before 5k MEA AST, and open symbols with dashed lines represent data after AST.

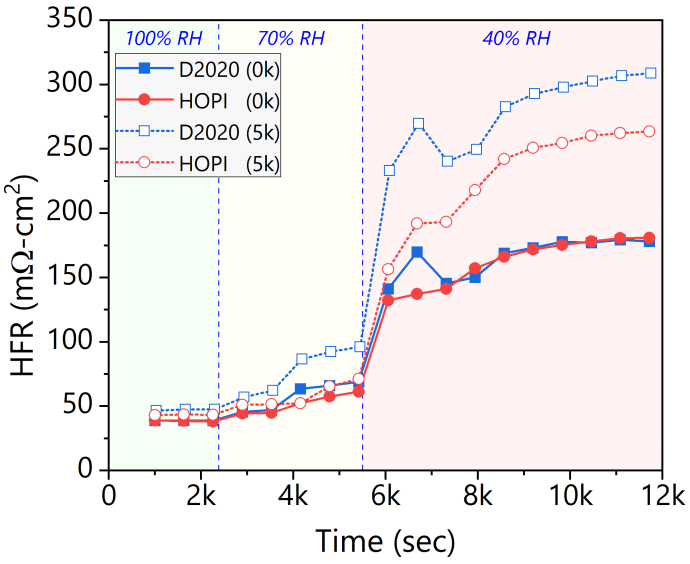

Figure 5.5: Membrane proton transport resistance or the HFR as measured from a Nyquist plot. Cell operating conditions: H/N_2, 70 °C, 40∼100% RH, 300 kPa abs., 0.20 V DC, 10 mV AC. Solid symbols with straight lines represent data before 5k MEA AST, and open symbols with dashed lines represent data after AST.

5.2.2.2 Oxygen transport resistance

In-situ limiting current experiments are conducted to evaluate the oxygen transport properties in the cell from the channel to the electrode layer. Faraday's law and Fick's law of diffusion are combined to measure the total oxygen transport resistance (OTR). The OTR in the large pores of the gas diffusion layer is pressure-dependent, while the OTR in the micro pores of the MPL and electrode are pressure-independent because Knudsen diffusion is dominant there. Detailed theory on the limiting current experiments and evaluation of different oxygen transport properties can be found in our previous works [24, 51].

The transport resistance in the channel is subtracted from the total dry transport resistance to get the combined OTR in the diffusion media and electrode, which is then plotted as a function of total cell backpressure in Figure 5.6(a). The pressure-independent OTR in the electrode micropores, R_{NP}, is evaluated from the y-axis intercept, that is, the point where the cell pressure approaches zero. Despite the HOPI cell exhibiting a marginally higher overall diffusion transport resistance than the D2020 cell, the increase in electrode OTR for the D2020 cell is a substantial

97%, in stark contrast to the HOPI cell's modest 30% increase. Consequently, the electrode constructed with HOPI ionomer displays significantly less degradation during AST compared to the D2020.

Additionally, OTR for both cells under wet conditions are assessed across a wider range of oxygen concentrations, ranging from 1% to 21%, with the results depicted in Figure 5.6(b). Higher oxygen concentrations under fully humidified conditions are employed to ensure water condensation in the cell, allowing for a thorough investigation of the impact on wet transport resistance. This experiment typically indicates water condensation behavior in the gas diffusion layer. The trend suggests a higher OTR for the HOPI cell, corroborating the cell's tendency to retain more water than the D2020 cell.

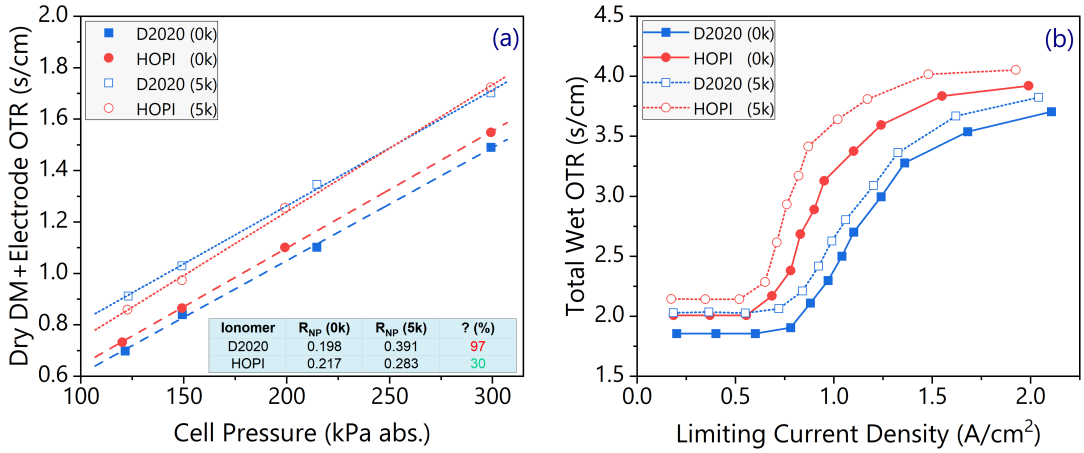

Figure 5.6: Oxygen transport resistance for HOPI and D2020 cells under (a) dry (80 °C, 64% RH, 100 kPa abs.) and (b) wet (70 °C, 100% RH, 300 kPa abs.) operating conditions. Solid symbols with dashed/solid lines represent data before 5k MEA AST, and open symbols with dotted lines represent data after AST.

5.2.2.3 Polarization performance

The H_2/Air polarization curves along with high frequency resistance (HFR) for both the HOPI and D2020 cells, before and after 5k MEA AST, are shown in Figure 5.7(a-c). Furthermore, the H_2/Air catalytic mass activities at 0.90 V are delineated in Figure 5.7(d). Under low relative humidity conditions, HOPI cell shows superior performance. Additionally, the HFR or cell resistance is slightly lower for the HOPI cell as compared to the D2020 cell. Under wet conditions, the HOPI cell shows comparable performance levels to the D2020 cell until reaching

the mass transport region, at which point pronounced flooding occurs at elevated current density conditions – both for pre- and post-MEA AST. This might have caused due to higher water retention capacity of HOPI ionomer, as inferred from sheet resistance measurement in Figure 5.4. It should be noted that flooding at high current densities can also be attributed to the high oxygen transport resistance for the gas diffusion media used in the HOPI cell observed in Figure 5.6. In terms of mass activity loss, the HOPI cell demonstrates losses of 31.20%, 23.31%, and 23.46% under dry, wet, and DOE-DryPol conditions, respectively. In contrast. D2020 cell exhibits losses of 32.64%, 34.49%, and 22.56%, respectively. Therefore, HOPI cell experiences approximately 11% less mass activity loss than the D2020 cell under the wet operating conditions.

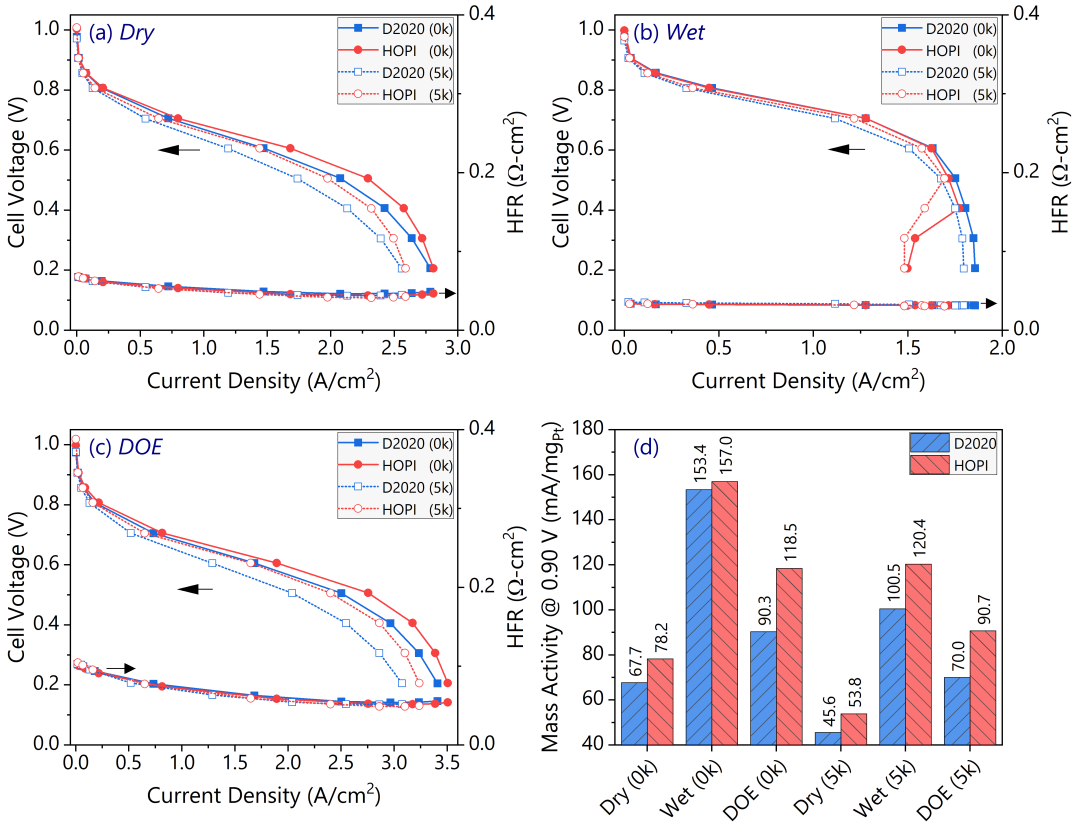

Figure 5.7: Performance and HFR curves for D2020 (blue) and HOPI (red) ionomer-based cell under (a) dry conditions: 70 °C, 60% RH, 100 kPa abs.; (b) wet conditions: 70 °C, 100% RH, 300 kPa abs.; (c) DOE-DryPol conditions: 88 °C, 40% RH, 250 kPa abs.; and (c) catalytic mass activity evaluated at 0.90 V. Solid symbols with straight lines represent data before 5k MEA AST, and open symbols with dashed lines represent data after AST.

5.3 Summary

A comprehensive comparison of cell performance and durability between PEMFCs employing HOPI and D2020 ionomers is conducted. The results highlight the potential advantages of incorporating HOPI as a cathode catalyst material to enhance cell durability and performance, especially in heavy-duty applications. The HOPI MEA demonstrated superior performance during cell activation or break-in, exhibiting a degradation rate of only 0.112 mA/cm^2 per cycle, compared to the 0.145 mA/cm^2 for the D2020 ionomer, over the 5000 cycles of the DOE H_2/Air MEA AST. The HOPI cell showed significantly lower cathode transport resistance, even

after the AST, across a broader range of relative humidity conditions. Moreover, the HOPI cell experienced only a 23% increase in oxygen transport resistance compared to the 97% increase observed with the D2020 ionomer after durability tests. HOPI demonstrated better performance under dry conditions and some flooding under high current density and wet conditions, potentially attributable to the higher water retention capacity of the HOPI ionomer. These results make HOPI as a compelling choice for cathode catalyst material in future fuel cell technology developments, especially in applications where cell durability is critical, such as in heavy-duty vehicles like long-haul trucks. Further research on HOPI-based ionomer is necessary for better optimization of the cathode catalyst to meet and exceed current performance and durability targets.

Note

Certain trade names and company products are mentioned in the text or identified in an illustration in order to adequately specify the experimental procedure and equipment used. In no case does such identification imply recommendation or endorsement, nor does it imply that the products are necessarily the best available for the purpose.

Acknowledgement

This work was sponsored by the University of California, Merced. It was partially supported by Chemours. I would like to thank Dr. Nitul Kakati and Joy Marie Mora for their contributions. Special thanks to Austin Plymill and Andrew Park for their valuable discussions on the experimental results.

Chapter 6

CONCLUSION & FUTURE WORK

6.1 Summary: Project on AEMFC sensitivity

An AEMFC experiences more complex and interesting water transport mechanism than a PEMFC. More research of an AEMFC is needed to have deeper understanding on its sensitivity to different parameters. In the first project, as explained in Chapter 3, sensitivity of the AEMFC performance is investigated under different operating conditions (e.g., relative humidity, reactant sensitivity) under both dynamic and steady-state conditions. Break-in procedures and fuel cell performances are also evaluated. The study is performed using two types of flow fields (single channel serpentine and straight parallel) and two types of gas diffusion electrodes (powder and dispersion ionomer type). Two GDEs are prepared with solid and powder ionomer binder, GDE-1 and GDE-2 respectively. The dispersion or liquid ionomer binder made a very hydrophobic electrode that made ion exchange difficult and resulted in poor performance although the membrane was sufficiently hydrated. Adding ethanol to ion exchange solution is able to improve exchange and consequently performance. From the performance observation for two mentioned flow fields, it is found that the cell performance is very sensitive to channel design; serpentine design offers better performance due to active water removal from the cell as compared to the straight parallel design. The study of RH sensitivity shows that different RH conditions have clear effect on cell performance and cell water behavior. It is observed that the ohmic performance is reduced and the concentration performance is increased with lowering the RH. The reduction in the ohmic performance can be attributed to the membrane being heated up under low humid conditions, and on the other hand, for concentration region, cell liquid water management gets better due to a combination of water production from reaction and less water from low humidified reactant streams. Low concentrations of hydrogen and oxygen sensitivity experiments show that performance is more sensitive when reducing the hydrogen on the anode side. Finally, neutron experiments show that cathode gets more water at the beginning of the cell operation, out of which most water is then transported to the anode through electroosmotic drag, the balance shifts towards anode and anode becomes flooded at some point which causes the cell performance to reduce.

6.2 Summary: Project on Membrane thickness & limiting current sensitivity

A systematic investigation is performed to examine the influence of membrane thickness and operational conditions on limiting current analysis. Through experimental approaches, we evaluated the oxygen transport resistance across standard Nafion membranes of two distinct thicknesses (25 and 85 µm) under varying cell temperatures, pressures, and humidity levels, employing Toray 060 and Freudenberg H23C8 as gas diffusion media. The investigation results illuminate several critical insights. The study demonstrates that membrane thickness significantly influences oxygen transport resistance, with thicker membranes deviating from expected limiting current behavior due to altered water management within the cell. Specifically, our findings reveal that increased membrane thickness can exacerbate issues with liquid water condensation and transport, leading to a notable rising trend in oxygen transport resistance with oxygen concentration. The sensitivity analysis focusing on temperature, pressure, and humidity further underscores the intricate relationship between these operational conditions and the accurate determination of limiting current. Increasing relative humidity to 80% for the 85 µm membrane using Toray GDM resulted in improved oxygen transport resistance (OTR) data, suggesting a beneficial alteration in water balance within the cell. This contrasts with the results obtained for Freudenberg GDM, where no clear trend emerged, highlighting the complex interplay between GDM type, membrane thickness, and operational conditions. Through a comprehensive examination of these factors, we have identified key considerations for the correct application and interpretation of the limiting current method in PEMFCs. This work contributes to the fundamental understanding of the method's limitations and potentials, paving the way for refined diagnostic techniques that can more accurately reflect the intricate interactions within fuel cells. Future research should continue to explore these dynamics, particularly the role of water management in influencing transport resistance, especially when using a membrane thicker than standard 25 µm thickness, to enhance the predictive accuracy and reliability of limiting current measurements in PEMFC systems.

6.3 Summary: Project on HOPI Ionomer

A comprehensive comparison of cell performance and durability between PEMFCs employing HOPI and D2020 ionomers is conducted. The results highlight the potential advantages of incorporating HOPI as a cathode catalyst material to enhance cell durability and performance, especially in heavy-duty applications. The HOPI MEA demonstrated superior performance during cell activation or break-in, exhibiting a degradation rate of only 0.112 mA/cm^2 per cycle, compared to the 0.145 mA/cm^2 for the D2020 ionomer, over the 5000 cycles of the DOE H_2/Air MEA AST. The HOPI cell showed significantly lower cathode transport resistance, even after the AST, across a broader range of relative humidity conditions. Moreover,

the HOPI cell experienced only a 23% increase in oxygen transport resistance compared to the 97% increase observed with the D2020 ionomer after durability tests. HOPI demonstrated better performance under dry conditions and some flooding under high current density and wet conditions, potentially attributable to the higher water retention capacity of the HOPI ionomer. These results make HOPI as a compelling choice for cathode catalyst material in future fuel cell technology developments, especially in applications where cell durability is critical, such as in heavy-duty vehicles like long-haul trucks. Further research on HOPI-based ionomer is necessary for better optimization of the cathode catalyst to meet and exceed current performance and durability targets.

6.4 Future work

The AEMFC exhibits great potential due to its enhanced cathode oxygen reduction reaction and the ability to utilize low-cost cathode catalysts and flow field materials. However, it presents unique water management challenges, such as severe flooding at the anode and dehydration at the cathode. Therefore, modeling work is necessary to deepen our understanding of the physics behind transport issues in an AEMFC. A manuscript on this project has been prepared and is expected to be submitted to a journal by May 2024.

The project focusing on the sensitivity study of membrane thickness and cell operating conditions opens new doors for developing a better understanding of evaluating correct oxygen transport properties through the limiting current method. Joy Marie Mora is planned to conduct modeling work to elucidate the water transport behavior using thicker membranes and for cells operating under various temperatures, pressure, and especially relative humidity conditions. A manuscript on this project is in preparation and is planned to be submitted to a journal by July 2024.

The project on HOPI ionomer is crucial as it demonstrates the potential of this ionomer to significantly enhance fuel cell performance and durability. Expanding on this project, we aim to investigate its electrostatic stability, rheological properties, and impedance characteristics. Joy Marie Mora and Nitul Kakati are planned to conduct studies on zeta-potentials and agglomerate size measurements to assess electrostatic repulsion and stability, respectively. Moreover, ink viscosity and viscoelastic behavior will be examined through ink rheology studies. A manuscript on this project is currently being written, with plans for submission to a journal by August 2024.

APPENDIX A

A.1 Properties of Toray 060 gas diffusion layer

Property	Value
Uncompressed Thickness (μm)	190
Density (g/m^2)	0.44
Air Permeability (m^2)	12.80×10^{-12}
Through-plane Resistance (mΩcm)	80
Thermal conductivity (in-plane, room temperature) (W/mK)	21
Thermal conductivity (through-plane, room temperature) (W/mK)	124∼1.60
Tensile Strength (N/cm)	70
Flexural Modulus (MPa)	40
Porosity (Uncompressed) (%)	78
Target compression (%)	22±1.5

Table A.1: Specifications for the Toray 060 GDL [98, 147–149]

A.2 Properties of Freudenberg H23C8 gas diffusion media

Property	Value
Uncompressed Thickness (μm)	230
Area Weight (g/m^2)	135
Thermal conductivity (through-plane, room temperature) (W/mK)	0.11∼0.16
Tensile Strength (N/cm)	≥70
Porosity (Uncompressed) (%)	80
Target compression (%)	17±1.5

Table A.2: Specifications for the Freudenberg H23C8 GDM [147, 149, 150]

Bibliography

[1] Information collected from National Geographic Website. *https://https://www.nationalgeographic.com/environment/article/greenhouse-gases/.*

[2] Leon Clarke et al. "Scenarios of greenhouse gas emissions and atmospheric concentrations". In: (2007).

[3] Information collected from NASA Earth Observatory. *https://earthobservatory.nasa.gov/world-of-change/global-temperatures/.*

[4] M Balat. "Influence of coal as an energy source on environmental pollution". In: *Energy Sources, Part A: Recovery, Utilization, and Environmental Effects* 29.7 (2007), pp. 581–589.

[5] Information collected from US Environmental Protection Agency. *https://www.epa.gov/ghgemissions/overview-greenhouse-gases/.*

[6] Information collected from US Environmental Protection Agency. *https://www.epa.gov/greenvehicles/greenhouse-gas-emissions-typical-passenger-vehicle/.*

[7] J Lee et al. "Investigating the effects of gas diffusion layer substrate thickness on polymer electrolyte membrane fuel cell performance via synchrotron X-ray radiography". In: *Electrochimica Acta* 236 (2017), pp. 161–170.

[8] Toshihiko Yoshida and Koichi Kojima. "Toyota MIRAI fuel cell vehicle and progress toward a future hydrogen society". In: *Electrochemical Society Interface* 24.2 (2015), p. 45.

[9] Zachary P Cano et al. "Batteries and fuel cells for emerging electric vehicle markets". In: *Nature Energy* 3.4 (2018), pp. 279–289.

[10] Jenn-Jiang Hwang. "Sustainability study of hydrogen pathways for fuel cell vehicle applications". In: *Renewable and Sustainable Energy Reviews* 19 (2013), pp. 220–229.

[11] JP Owejan et al. "Investigation of micro-and macro-scale transport processes for improved fuel cell performance". In: *FY 2011 annual progress report, DOE hydrogen and fuel cells program* (2011), pp. 827–832.

[12] Marco Mariani et al. “The Role of Fluorinated Polymers in the Water Management of Proton Exchange Membrane Fuel Cells: A Review”. In: *Energies* 14.24 (2021), p. 8387.

[13] Allen Hermann, Tapas Chaudhuri, and Priscila Spagnol. “Bipolar plates for PEM fuel cells: A review”. In: *International journal of hydrogen Energy* 30.12 (2005), pp. 1297–1302.

[14] Dewan Hasan Ahmed and Hyung Jin Sung. “Effects of channel geometrical configuration and shoulder width on PEMFC performance at high current density”. In: *Journal of Power Sources* 162.1 (2006), pp. 327–339.

[15] J Scholta et al. “Investigation on the influence of channel geometries on PEMFC performance”. In: *Journal of Power Sources* 155.1 (2006), pp. 66–71.

[16] Nuttapol Limjeerajarus and Patcharawat Charoen-Amornkitt. “Effect of different flow field designs and number of channels on performance of a small PEFC”. In: *International Journal of Hydrogen Energy* 40.22 (2015), pp. 7144–7158.

[17] Ryan O’hayre et al. *Fuel cell fundamentals*. John Wiley & Sons, 2016.

[18] F Mojica et al. “Experimental Study of Three Channel Designs with Model Comparison in a PEM Fuel Cell”. In: *Fuel Cells* (2020).

[19] Dusan Spernjak, Ajay K Prasad, and Suresh G Advani. “In situ comparison of water content and dynamics in parallel, single-serpentine, and interdigitated flow fields of polymer electrolyte membrane fuel cells”. In: *Journal of Power Sources* 195.11 (2010), pp. 3553–3568.

[20] BH Lim et al. “Effects of flow field design on water management and reactant distribution in PEMFC: a review”. In: *Ionics* 22.3 (2016), pp. 301–316.

[21] Hong Liu et al. “Experimental study and comparison of various designs of gas flow fields to PEM fuel cells and cell stack performance”. In: *Frontiers in Energy Research* 2 (2014), p. 2.

[22] Kui Jiao, Jaewan Park, and Xianguo Li. “Experimental investigations on liquid water removal from the gas diffusion layer by reactant flow in a PEM fuel cell”. In: *Applied Energy* 87.9 (2010), pp. 2770–2777.

[23] Nathanial J Cooper et al. “Experimental optimization of parallel and interdigitated PEMFC flow-field channel geometry”. In: *international journal of hydrogen energy* 41.2 (2016), pp. 1213–1223.

[24] Felipe Mojica et al. “Study of converging-diverging channel induced convective mass transport in a proton exchange membrane fuel cell”. In: *Energy Conversion and Management* 237 (2021), p. 114095.

[25] Yasuyuki Sando. "Research and development of fuel cell vehicles at Honda". In: *ECS Transactions* 25.1 (2009), p. 211.

[26] Minkmas V Williams et al. "Characterization of gas diffusion layers for PEMFC". In: *Journal of the Electrochemical Society* 151.8 (2004), A1173–A1180.

[27] M Prasanna et al. "Influence of cathode gas diffusion media on the performance of the PEMFCs". In: *Journal of Power Sources* 131.1-2 (2004), pp. 147–154.

[28] Wolf Vielstich, Arnold Lamm, and Hubert A Gasteiger. *Handbook of fuel cells: fundamentals technology and applications*. Vol. 3, chapter 46. Wiley New York, 2010.

[29] Mark C Lefebvre, Rex B Martin, and Peter G Pickup. "Characterization of ionic conductivity profiles within proton exchange membrane fuel cell gas diffusion electrodes by impedance spectroscopy". In: *Electrochemical and Solid State Letters* 2.6 (1999), p. 259.

[30] Po-Ya Abel Chuang et al. "The interactive effect of heat and mass transport on water condensation in the gas diffusion layer of a proton exchange membrane fuel cell". In: *Journal of Power Sources* 480 (2020), p. 229121.

[31] Haolin Tang et al. "A degradation study of Nafion proton exchange membrane of PEM fuel cells". In: *Journal of Power Sources* 170.1 (2007), pp. 85–92.

[32] Srinivasan Raman et al. "Effects of water induced pore blockage and mitigation strategies in low temperature PEM fuel cells–A simulation study". In: *International Journal of Hydrogen Energy* 42.37 (2017), pp. 23799–23813.

[33] Guangyu Lin and Trung Van Nguyen. "Effect of thickness and hydrophobic polymer content of the gas diffusion layer on electrode flooding level in a PEMFC". In: *Journal of The Electrochemical Society* 152.10 (2005), A1942–A1948.

[34] Trung Van Nguyen. "Effect of Morphological and Wetting Characteristics of the Gas Diffusion Layers on Electrode Flooding Level in a PEM Fuel Cell". In: *ECS Proceedings Volumes* 2004-21.1 (2004), pp. 412–416.

[35] Sehkyu Park, Jong-Won Lee, and Branko N Popov. "A review of gas diffusion layer in PEM fuel cells: Materials and designs". In: *International Journal of Hydrogen Energy* 37.7 (2012), pp. 5850–5865.

[36] Mehdi Mortazavi and Kazuya Tajiri. "Effect of the PTFE content in the gas diffusion layer on water transport in polymer electrolyte fuel cells (PEFCs)". In: *Journal of Power Sources* 245 (2014), pp. 236–244.

[37] Chan Lim and CY Wang. “Effects of hydrophobic polymer content in GDL on power performance of a PEM fuel cell”. In: *Electrochimica Acta* 49.24 (2004), pp. 4149–4156.

[38] Saverio Latorrata et al. “Performance Evaluation and Durability Enhancement of FEP-Based Gas Diffusion Media for PEM Fuel Cells”. In: *Energies* 10.12 (2017), p. 2063.

[39] Israel Cabasso, Youxin Yuan, and Xiao Xu. *Gas diffusion electrodes based on poly (vinylidene fluoride) carbon blends*. US Patent 5,783,325. 1998.

[40] Sung Bum Park et al. “Fabrication of GDL microporous layer using PVDF for PEMFCs”. In: *Journal of Physics: Conference Series*. Vol. 165. IOP Publishing. 2009, p. 012046.

[41] Saverio Latorrata et al. “Design of properties and performances of innovative gas diffusion media for polymer electrolyte membrane fuel cells”. In: *Progress in Organic Coatings* 78 (2015), pp. 517–525.

[42] XL Wang et al. “Micro-porous layer with composite carbon black for PEM fuel cells”. In: *Electrochimica Acta* 51.23 (2006), pp. 4909–4915.

[43] J Soler, E Hontanon, and L Daza. “Electrode permeability and flow-field configuration: influence on the performance of a PEMFC”. In: *Journal of Power Sources* 118.1-2 (2003), pp. 172–178.

[44] Zhigang Qi and Arthur Kaufman. “Improvement of water management by a microporous sublayer for PEM fuel cells”. In: *Journal of Power Sources* 109.1 (2002), pp. 38–46.

[45] Adam Z Weber and John Newman. “Effects of microporous layers in polymer electrolyte fuel cells”. In: *Journal of the Electrochemical Society* 152.4 (2005), A677–A688.

[46] Fereshteh Salimi Nanadegani, Ebrahim Nemati Lay, and Bengt Sunden. “Effects of an MPL on water and thermal management in a PEMFC”. In: *International Journal of Energy Research* 43.1 (2019), pp. 274–296.

[47] Hasan K Atiyeh et al. “Experimental investigation of the role of a microporous layer on the water transport and performance of a PEM fuel cell”. In: *Journal of Power Sources* 170.1 (2007), pp. 111–121.

[48] Dzmitry Malevich et al. “Investigation of charge-transfer and mass-transport resistances in PEMFCs with microporous layer using electrochemical impedance spectroscopy”. In: *Journal of The Electrochemical Society* 156.2 (2009), B216–B224.

[49] Jeff T Gostick et al. “On the role of the microporous layer in PEMFC operation”. In: *Electrochemistry Communications* 11.3 (2009), pp. 576–579.

[50] Anthony Thomas et al. “Thermal and water transfer in PEMFCs: investigating the role of the microporous layer”. In: *International Journal of Hydrogen Energy* 39.6 (2014), pp. 2649–2658.

[51] Mrittunjoy Sarker et al. “Experimental and computational study of the microporous layer and hydrophobic treatment in the gas diffusion layer of a proton exchange membrane fuel cell”. In: *Journal of Power Sources* 509 (2021), p. 230350.

[52] Sharon Thomas and Marcia Zalbowitz. *Fuel cells-green power*. Los Alamos National Laboratory, 1999.

[53] Ashutosh G Divekar et al. “The impact of alkyl tri-methyl ammonium side chains on perfluorinated ionic membranes for electrochemical applications”. In: *Journal of Polymer Science Part B: Polymer Physics* 57.11 (2019), pp. 700–712.

[54] Andrew Michael Park et al. “Synthesis and characterization of perfluorinated anion exchange membranes”. In: *ECS Transactions* 80.8 (2017), p. 957.

[55] Jon P Owejan et al. “Water management studies in PEM fuel cells, Part I: Fuel cell design and in situ water distributions”. In: *International Journal of Hydrogen Energy* 34.8 (2009), pp. 3436–3444.

[56] William E Mustain et al. “Durability challenges of anion exchange membrane fuel cells”. In: *Energy & Environmental Science* 13.9 (2020), pp. 2805–2838.

[57] Heng Zhang et al. “Microstructure reconstruction of the gas diffusion layer and analyses of the anisotropic transport properties”. In: *Energy Conversion and Management* 241 (2021), p. 114293.

[58] Heng Zhang et al. “Coupled stress–strain and transport in proton exchange membrane fuel cell with metallic bipolar plates”. In: *Applied Energy* 251 (2019), p. 113316.

[59] Yiwei Zheng et al. “Quantifying and elucidating the effect of CO 2 on the thermodynamics, kinetics and charge transport of AEMFCs”. In: *Energy & Environmental Science* 12.9 (2019), pp. 2806–2819.

[60] Marc Francis Labata et al. “Insights on platinum-carbon catalyst degradation mechanism for oxygen reduction reaction in acidic and alkaline media”. In: *Journal of Power Sources* 487 (2021), p. 229356.

[61] Dario R Dekel. “Review of cell performance in anion exchange membrane fuel cells”. In: *Journal of Power Sources* 375 (2018), pp. 158–169.

[62] Yiwei Zheng et al. “Editors’ Choice—Power-Generating Electrochemical CO2 Scrubbing from Air Enabling Practical AEMFC Application”. In: *Journal of The Electrochemical Society* 168.2 (2021), p. 024504.

[63] Karam Yassin et al. “The effect of membrane thickness on AEMFC Performance: An integrated theoretical and experimental study”. In: *Energy Conversion and Management* 270 (2022), p. 116203.

[64] Shanfu Lu et al. “Alkaline polymer electrolyte fuel cells completely free from noble metal catalysts”. In: *Proceedings of the National Academy of Sciences* 105.52 (2008), pp. 20611–20614.

[65] Andrew Dicks and David Anthony James Rand. *Fuel cell systems explained*. Vol. 479. Wiley Online Library, 2018.

[66] PJ Hamilton and BG Pollet. “Polymer electrolyte membrane fuel cell (PEMFC) flow field plate: design, materials and characterisation”. In: *Fuel cells* 10.4 (2010), pp. 489–509.

[67] Jennie Huya-Kouadio. “Doe hydrogen and fuel cells program record”. In: (2017).

[68] Van Men Truong et al. “Effects of cell temperature and reactant humidification on anion exchange membrane fuel cells”. In: *Materials* 12.13 (2019), p. 2048.

[69] Shimshon Gottesfeld et al. “Anion exchange membrane fuel cells: Current status and remaining challenges”. In: *Journal of Power Sources* 375 (2018), pp. 170–184.

[70] JS Spendelow et al. “Mechanism of CO oxidation on Pt (111) in alkaline media”. In: *The Journal of Physical Chemistry B* 110.19 (2006), pp. 9545–9555.

[71] John R Varcoe et al. “Anion-exchange membranes in electrochemical energy systems”. In: *Energy & environmental science* 7.10 (2014), pp. 3135–3191.

[72] Klaus-Dieter Kreuer and Patric Jannasch. “A practical method for measuring the ion exchange capacity decrease of hydroxide exchange membranes during intrinsic degradation”. In: *Journal of Power Sources* 375 (2018), pp. 361–366.

[73] Karam Yassin et al. “Elucidating the role of anion-exchange ionomer conductivity within the cathode catalytic layer of anion-exchange membrane fuel cells”. In: *Journal of Power Sources* 524 (2022), p. 231083.

[74] Huai-Suen Shiau, Iryna V Zenyuk, and Adam Z Weber. “Elucidating performance limitations in alkaline-exchange-membrane fuel cells”. In: *Journal of The Electrochemical Society* 164.11 (2017), E3583.

[75] Yawen Zhou et al. “Improving cell performance for anion exchange membrane fuel cells with FeNC cathode by optimizing ionomer content”. In: *International Journal of Hydrogen Energy* 48.13 (2023), pp. 5266–5275.

[76] Junhua Wang et al. “Poly (aryl piperidinium) membranes and ionomers for hydroxide exchange membrane fuel cells”. In: *Nature Energy* 4.5 (2019), pp. 392–398.

[77] Shohei Suzuki et al. “Influence of CO2 dissolution into anion exchange membrane on fuel cell performance”. In: *Electrochimica acta* 88 (2013), pp. 552–558.

[78] Andrew M Kiss et al. “Carbonate and bicarbonate ion transport in alkaline anion exchange membranes”. In: *Journal of The Electrochemical Society* 160.9 (2013), F994.

[79] Karam Yassin et al. “A surprising relation between operating temperature and stability of anion exchange membrane fuel cells”. In: *Journal of Power Sources Advances* 11 (2021), p. 100066.

[80] María I León et al. “Water movement through an anion exchange membrane fuel cell (AEMFC): Influence of gas humidity and flow rate”. In: *Applied Energy* 324 (2022), p. 119722.

[81] TJ Omasta et al. “Importance of balancing membrane and electrode water in anion exchange membrane fuel cells”. In: *Journal of Power Sources* 375 (2018), pp. 205–213.

[82] Robert B Kaspar et al. “Manipulating water in high-performance hydroxide exchange membrane fuel cells through asymmetric humidification and wetproofing”. In: *Journal of the Electrochemical Society* 162.6 (2015), F483.

[83] Dario R Dekel et al. “Steady state and transient simulation of anion exchange membrane fuel cells”. In: *Journal of Power Sources* 375 (2018), pp. 191–204.

[84] Kui Jiao et al. “An analytical model for hydrogen alkaline anion exchange membrane fuel cell”. In: *International Journal of Hydrogen Energy* 40.8 (2015), pp. 3300–3312.

[85] Young-Jun Sohn, Jung-Il CHOI, and Kyoungyoun Kim. “Numerical analysis on water transport in alkaline anion exchange membrane fuel cells”. In: *Electrochemistry* 83.2 (2015), pp. 80–83.

[86] Kui Jiao et al. “Three-dimensional multiphase modeling of alkaline anion exchange membrane fuel cell”. In: *International journal of hydrogen energy* 39.11 (2014), pp. 5981–5995.

[87] Huai-Suen Shiau, Iryna V Zenyuk, and Adam Z Weber. “Water management in an alkaline-exchange-membrane fuel cell”. In: *ECS Transactions* 69.17 (2015), p. 985.

[88] Sen Huo et al. “Water management in alkaline anion exchange membrane fuel cell anode”. In: *international journal of hydrogen energy* 37.23 (2012), pp. 18389–18402.

[89] Joy Marie Mora et al. “Analytical-based simulation approach for an anion exchange membrane fuel cell”. In: *Energy Conversion and Management* 273 (2022), p. 116382.

[90] GS Hwang and AZ Weber. “Effective-diffusivity measurement of partially-saturated fuel-cell gas-diffusion layers”. In: *Journal of The Electrochemical Society* 159.11 (2012), F683–F692.

[91] Aakash Kumar and Mayank Sehgal. “Hydrogen fuel cell technology for a sustainable future: A review”. In: (2018).

[92] Adnan Ozden et al. “A review of gas diffusion layers for proton exchange membrane fuel cells—With a focus on characteristics, characterization techniques, materials and designs”. In: *Progress in Energy and Combustion Science* 74 (2019), pp. 50–102.

[93] L Cindrella et al. “Gas diffusion layer for proton exchange membrane fuel cells - A review”. In: *Journal of Power Sources* 194.1 (2009), pp. 146–160.

[94] Yan-Jie Wang et al. “Unlocking the door to highly active ORR catalysts for PEMFC applications: polyhedron-engineered Pt-based nanocrystals”. In: *Energy & Environmental Science* 11.2 (2018), pp. 258–275.

[95] Hui Xu et al. “Effect of elevated temperature and reduced relative humidity on ORR kinetics for PEM fuel cells”. In: *Journal of the Electrochemical Society* 152.9 (2005), A1828.

[96] A Brouzgou, SQ Song, and P Tsiakaras. “Low and non-platinum electrocatalysts for PEMFCs: Current status, challenges and prospects”. In: *Applied Catalysis B: Environmental* 127 (2012), pp. 371–388.

[97] Daniel R Baker et al. “Measurement of oxygen transport resistance in PEM fuel cells by limiting current methods”. In: *Journal of The Electrochemical Society* 156.9 (2009), B991–B1003.

[98] David A Caulk and Daniel R Baker. “Heat and water transport in hydrophobic diffusion media of PEM fuel cells”. In: *Journal of The Electrochemical Society* 157.8 (2010), B1237–B1244.

[99] Daniel R Baker and David A Caulk. “Limiting current as a tool to study oxygen transport in PEM fuel cells”. In: *ECS Transactions* 50.2 (2013), pp. 35–45.

[100] Daniel R Baker et al. “The use of limiting current to determine transport resistance in PEM fuel cells”. In: *ECS Transactions* 3.1 (2006), p. 989.

[101] Tetsuya Mashio et al. “Analysis of reactant gas transport in a catalyst layer”. In: *ECS Transactions* 11.1 (2007), p. 529.

[102] David A Caulk and Daniel R Baker. “Modeling two-phase water transport in hydrophobic diffusion media for PEM fuel cells”. In: *Journal of The Electrochemical Society* 158.4 (2011), B384–B393.

[103] Anusorn Kongkanand and Mark F Mathias. “The priority and challenge of high-power performance of low-platinum proton-exchange membrane fuel cells”. In: *The journal of physical chemistry letters* 7.7 (2016), pp. 1127–1137.

[104] J St-Pierre et al. “Limiting current operation of proton exchange membrane fuel cells”. In: *Journal of The Electrochemical Society* 154.2 (2007), B186–B193.

[105] Chao Wang et al. “The experimental measurement of local and bulk oxygen transport resistances in the catalyst layer of proton exchange membrane fuel cells”. In: *The journal of physical chemistry letters* 8.23 (2017), pp. 5848–5852.

[106] Nada Zamel and Xianguo Li. “Effective transport properties for polymer electrolyte membrane fuel cells–with a focus on the gas diffusion layer”. In: *Progress in energy and combustion science* 39.1 (2013), pp. 111–146.

[107] Jaewoo Cho, Jaejun Ko, and Sehkyu Park. “Comprehensive analysis of critical factors determining limiting current of PEMFC: O2 and H+ transport resistance without cathode humidification”. In: *Journal of The Electrochemical Society* 167.8 (2020), p. 084511.

[108] *Fuel Cell Technical Team Roadmap, November*. Tech. rep. Tech. Rep. July, US Department of Energy. URL: www. uscar. org, 2017. URL: https://www.energy.gov/sites/prod/files/2017/11/f46/FCTT_Roadmap_Nov_2017_FINAL.pdf.

[109] J Vickers. *Hydrogen Storage Technologies Roadmap Fuel Cell Technical Team Roadmap, July*. Tech. rep. 2017. URL: https://www.energy.gov/eere/vehicles/articles/us-drive-hydrogen-storage-technical-team-roadmap.

[110] Million Mile Fuel Cell Truck Consortium. *Million Mile Fuel Cell Truck*. 2024. URL: https://millionmilefuelcelltruck.org/.

[111] Ryosuke Jinnouchi et al. “The role of oxygen-permeable ionomer for polymer electrolyte fuel cells”. In: *Nature communications* 12.1 (2021), p. 4956.

[112] PJ Ferreira et al. “Instability of Pt/ C electrocatalysts in proton exchange membrane fuel cells: a mechanistic investigation”. In: *Journal of the Electrochemical Society* 152.11 (2005), A2256.

[113] Jonathan P Braaten et al. "Integration of a high oxygen permeability ionomer into polymer electrolyte membrane fuel cell cathodes for high efficiency and power density". In: *Journal of Power Sources* 522 (2022), p. 230821.

[114] Kensaku Kodama et al. "Effect of the side-chain structure of perfluorosulfonic acid ionomers on the oxygen reduction reaction on the surface of Pt". In: *Acs Catalysis* 8.1 (2018), pp. 694–700.

[115] Thomas A Greszler, David Caulk, and Puneet Sinha. "The impact of platinum loading on oxygen transport resistance". In: *Journal of The Electrochemical Society* 159.12 (2012), F831.

[116] Natalia Macauley et al. "Highly durable fluorinated high oxygen permeability ionomers for proton exchange membrane fuel cells". In: *Advanced Energy Materials* 12.45 (2022), p. 2201063.

[117] Ji Hee Lee et al. "Investigation of structural and transport properties of highly oxygen-permeable ionomer in polymer electrolyte membrane fuel cells using molecular dynamics simulations". In: *Journal of Industrial and Engineering Chemistry* 123 (2023), pp. 418–427.

[118] Xiang Lyu et al. "Design of graded cathode catalyst layers with various ionomers for fuel cell application". In: *Journal of Power Sources* 556 (2023), p. 232530.

[119] Jian Zhao et al. "Effect of catalyst deposition on electrode structure, mass transport and performance of polymer electrolyte membrane fuel cells". In: *Applied Energy* 255 (2019), p. 113802.

[120] Shaojie Du et al. "Effect of Dispersion Method and Catalyst on the Crack Morphology and Performance of Catalyst Layer of PEMFC". In: *Journal of The Electrochemical Society* 168.11 (2021), p. 114506.

[121] Shaojie Du et al. "Effects of ionomer and dispersion methods on rheological behavior of proton exchange membrane fuel cell catalyst layer ink". In: *International Journal of Hydrogen Energy* 45.53 (2020), pp. 29430–29441.

[122] Travis J Omasta et al. "Beyond catalysis and membranes: visualizing and solving the challenge of electrode water accumulation and flooding in AEMFCs". In: *Energy & Environmental Science* 11.3 (2018), pp. 551–558.

[123] TA Trabold et al. "Use of neutron imaging for proton exchange membrane fuel cell (PEMFC) performance analysis and design". In: *Handbook of fuel cells: Advances in electrocatalysis, materials, diagnostics and durability* 5 (2009), pp. 658–672.

[124] M Arif et al. "Neutron imaging facility development and research trend at NIST". In: *Physics Procedia* 69 (2015), pp. 210–217.

[125] TA Trabold et al. “In situ investigation of water transport in an operating PEM fuel cell using neutron radiography: Part 1–Experimental method and serpentine flow field results”. In: *International Journal of Heat and Mass Transfer* 49.25-26 (2006), pp. 4712–4720.

[126] DS Hussey et al. “In situ fuel cell water metrology at the NIST neutron imaging facility”. In: *Journal of Fuel Cell Science and Technology* 7.2 (2010).

[127] Jacob M LaManna et al. “Neutron and X-ray Tomography (NeXT) system for simultaneous, dual modality tomography”. In: *Review of Scientific Instruments* 88.11 (2017), p. 113702.

[128] Richard S Fu et al. “High-resolution neutron radiography of through-plane liquid water distribution in polymer electrolyte membrane and gas diffusion layer”. In: *Journal of The Electrochemical Society* 159.9 (2012), F545.

[129] PA Chuang et al. “The nature of flooding and drying in polymer electrolyte fuel cells”. In: *International Conference on Fuel Cell Science, Engineering and Technology*. Vol. 37645. 2005, pp. 31–37.

[130] Heng Zhang et al. “Numerical investigation and experimental validation of water condensation in the gas diffusion layer with different properties”. In: *Journal of Cleaner Production* 402 (2023), p. 136792.

[131] Ibrahim Alaefour et al. “The role of flow-field layout on the conditioning of a proton exchange membrane fuel cell”. In: *Fuel* 230 (2018), pp. 98–103.

[132] Dietmar Gerteisen et al. “Effect of operating conditions on current density distribution and high frequency resistance in a segmented PEM fuel cell”. In: *international journal of hydrogen energy* 37.9 (2012), pp. 7736–7744.

[133] Rohit Makharia, Mark F Mathias, and Daniel R Baker. “Measurement of catalyst layer electrolyte resistance in PEFCs using electrochemical impedance spectroscopy”. In: *Journal of The Electrochemical Society* 152.5 (2005), A970.

[134] Jon P Owejan, Jeanette E Owejan, and Wenbin Gu. “Impact of platinum loading and catalyst layer structure on PEMFC performance”. In: *Journal of The Electrochemical Society* 160.8 (2013), F824.

[135] Xiaoyan Luo et al. “Thickness dependence of proton-exchange-membrane properties”. In: *Journal of The Electrochemical Society* 168.10 (2021), p. 104517.

[136] Shouwen Shi, Adam Z Weber, and Ahmet Kusoglu. “Structure/property relationship of Nafion XL composite membranes”. In: *Journal of Membrane Science* 516 (2016), pp. 123–134.

[137] Rui B Ferreira et al. "Experimental study on the membrane electrode assembly of a proton exchange membrane fuel cell: effects of microporous layer, membrane thickness and gas diffusion layer hydrophobic treatment". In: *Electrochimica Acta* 224 (2017), pp. 337–345.

[138] Wenming Liu et al. "Experimental study of proton exchange membrane fuel cells using Nafion 212 and Nafion 211 for portable application at ambient pressure and temperature conditions". In: *International Journal of Hydrogen Energy* 37.5 (2012), pp. 4673–4677.

[139] Zhenye Kang, Magnolia Pak, and Guido Bender. "Introducing a novel technique for measuring hydrogen crossover in membrane-based electrochemical cells". In: *International journal of hydrogen energy* 46.29 (2021), pp. 15161–15167.

[140] Shyam S Kocha, J Deliang Yang, and Jung S Yi. "Characterization of gas crossover and its implications in PEM fuel cells". In: *AIChE Journal* 52.5 (2006), pp. 1916–1925.

[141] Heng Zhang et al. "Pore-scale modeling of microporous layer for proton exchange membrane fuel cell: Effective transport properties". In: *Membranes* 13.2 (2023), p. 219.

[142] Christoph Simon, Frédéric Hasché, and Hubert A Gasteiger. "Influence of the gas diffusion layer compression on the oxygen transport in PEM fuel cells at high water saturation levels". In: *Journal of The Electrochemical Society* 164.6 (2017), F591–F599.

[143] Christoph Simon et al. "Influence of the gas diffusion layer compression on the oxygen mass transport in PEM fuel cells". In: *Ecs Transactions* 69.17 (2015), p. 1293.

[144] Jian Zhang et al. "Experimental and Numerical Simulation Study of Oxygen Transport in Proton Exchange Membrane Fuel Cells at Intermediate Temperatures (80° C–120° C)". In: *Membranes* 14.4 (2024), p. 72.

[145] Kenji Kudo, Ryosuke Jinnouchi, and Yu Morimoto. "Humidity and temperature dependences of oxygen transport resistance of Nafion thin film on platinum electrode". In: *Electrochimica Acta* 209 (2016), pp. 682–690.

[146] Rangachary Mukundan and Rodney L Borup. *AST Development in M2FCT (ASTWG and iDWG) Update to 21CTP [Slides]*. Tech. rep. Los Alamos National Lab.(LANL), Los Alamos, NM (United States), 2022.

[147] Properties of Toray 060 GDL from Fuel Cell Store. *https://www.fuelcellstore.com/toray-carbon-paper-060/*.

[148] Manish Khandelwal and MM Mench. “Direct measurement of through-plane thermal conductivity and contact resistance in fuel cell materials”. In: *Journal of Power Sources* 161.2 (2006), pp. 1106–1115.

[149] Odne S Burheim et al. “Through-plane thermal conductivity of PEMFC porous transport layers”. In: *Journal of Fuel Cell Science and Technology* 8.2 (2011).

[150] Robert Bock et al. “Experimental study of thermal conductivity and compression measurements of the gdl-mpl interfacial composite region”. In: *ECS Transactions* 75.14 (2016), p. 189.